



저작자표시-비영리-변경금지 2.0 대한민국

이용자는 아래의 조건을 따르는 경우에 한하여 자유롭게

- 이 저작물을 복제, 배포, 전송, 전시, 공연 및 방송할 수 있습니다.

다음과 같은 조건을 따라야 합니다:



저작자표시. 귀하는 원저작자를 표시하여야 합니다.



비영리. 귀하는 이 저작물을 영리 목적으로 이용할 수 없습니다.



변경금지. 귀하는 이 저작물을 개작, 변형 또는 가공할 수 없습니다.

- 귀하는, 이 저작물의 재이용이나 배포의 경우, 이 저작물에 적용된 이용허락조건을 명확하게 나타내어야 합니다.
- 저작권자로부터 별도의 허가를 받으면 이러한 조건들은 적용되지 않습니다.

저작권법에 따른 이용자의 권리는 위의 내용에 의하여 영향을 받지 않습니다.

이것은 [이용허락규약\(Legal Code\)](#)을 이해하기 쉽게 요약한 것입니다.

[Disclaimer](#)

Nanomaterial-based unconventional
image sensor array inspired by
human and aquatic animal

지도교수 김 대 형

이 논문을 공학박사 학위논문으로 제출함
2020년 1월

서울대학교 대학원
화학생명공학부 에너지환경융합기술전공
최 창 순

최창순의 공학박사 학위논문을 인준함
2020년 1월

위 원 장 _____ 성 영 은 (인)

부 위 원 장 _____ 김 대 형 (인)

위 원 _____ 현 태 환 (인)

위 원 장 _____ 이 탁 희 (인)

위 원 장 _____ 최 문 기 (인)

공학박사학위논문

**Nanomaterial-based unconventional image
sensor array inspired by human and
aquatic animal**

사람 및 수중 생물에서 영감을 받은
나노물질 기반 비정형 이미지 센서 어레이

2020년 2월

서울대학교 대학원

화학생물공학부 에너지환경융합전공

최 창 순

**Nanomaterial-based unconventional image
sensor array inspired by human and
aquatic animal**

**A THESIS SUBMITTED IN PARTIAL FULFILLMENT OF THE
REQUESTMENTS FOR THE DEGREE OF DOCTOR OF
PHILOSOPHY IN ENGINEERING AT THE GRADUATE SCHOOL
OF SEOUL NATIONAL UNIVERSITY**

February 2020

By

Changsoon Choi

Supervisor

Dae-Hyeong Kim

Abstract

Nanomaterial-based unconventional image sensor array inspired by human and aquatic animal

Changsoon Choi

School of Chemical and Biological Engineering

Chemical Convergence for Energy & Environment

The Graduate School

Seoul National University

Conventional camera technologies have attracted significant attentions over the past decades particularly for image-based applications such as image acquisition and object detection. However, conventional cameras are bulky, heavy, and expensive due to complicated multi-lens optics for focusing the images onto flat image sensors, which cannot meet the requirement in advanced mobile electronics. In this regard, the eyes in nature, biological imaging systems optimized through evolution, have

inspired the development of unconventional imaging systems for advanced mobile electronics due to their unique advantages over conventional camera technologies, including the simple and miniaturized optics, wide field-of-view (FoV), highly sensitive and efficient photo-detection, deep depth-of-field (DoF), and facile accommodation. Here, we describe three types of bio-inspired unconventional imaging systems.

First, the human-eye-inspired curved image sensor array was fabricated by employing ultrathin soft optoelectronic devices based on MoS₂-graphene heterostructure. Such imaging system enabled aberration-free imaging with a single plano-convex lens. In addition, the curved image sensor array was applied to the soft retinal prosthesis with minimal mechanical distortion to the retina due to its ultrathin thickness.

Second, the aquatic-vision-inspired imaging system was developed by employing the monocentric-lens and hemispherical silicon nanorod photodiode array. The aquatic-vision-inspired imaging system features aberration-free wide FoV imaging, miniaturized and single lens optics, deep DoF, facile accommodation, and enhanced photodetection. With these attributes, the developed imaging system successfully captured the projected images from wide angular directions.

Third, the curved neuromorphic image sensor array (cNISA), inspired by the human vision recognition system, was developed for efficient imagery pattern recognition by conferring neuromorphic functions to image sensors. The cNISA is based on the MoS₂-organic heterostructure that exhibits photon-triggered synaptic

plasticity (*e.g.*, short-term plasticity and long-term potentiation). Using these neuromorphic functions, the cNISA successfully identified the distinctive patterns from massive optical inputs without redundant data storage, processing, and communications, required in conventional imaging and post-data-processing systems.

Keywords: bio-inspired camera, flexible, human-eye-inspired, aquatic-vision-inspired, neuromorphic image sensor.

Student number: 2014-31082

Contents

Abstract	i
Contents	iv
List of Figures	vi
List of Tables	x
Chapter 1. Introduction	1
1.1 Structural and functional feature of camera-type eyes.....	1
1.2 Bio-inspired imaging system.	5
1.3 Retinal Prosthesis.....	14
1.4 Conclusion.....	20
1.5 Reference.....	21
Chapter 2. Human-eye-inspired soft optoelectronic device using high-density MoS₂-graphene curved image sensor array	27
2.1 Introduction.....	27
2.2 Experimental section.....	34
2.3 Result and discussion.....	41
2.4 Conclusion.....	69
2.5 Reference.....	70

Chapter 3. Aquatic-vision-inspired imaging system using a single monocentric lens and a silicon nanorod photodiode array	75
3.1 Introduction.....	75
3.2 Experimental section.....	81
3.3 Result and discussion.....	86
3.4 Conclusion.....	112
3.5 Reference.....	113
Chapter 4. Curved neuromorphic image sensor array using MoS₂-organic heterostructure inspired by human visual recognition system	118
4.1 Introduction.....	118
4.2 Experimental section.....	123
4.3 Result and discussion.....	125
4.4 Conclusion.....	152
4.5 Reference.....	153

List of Figures

Chapter 1

Figure 1.1. Evolution of camera-type eyes.....	3
Figure 1.2. Schematic of camera-type eyes.....	4
Figure 1.3. Device designs of camera-type eyes.....	6
Figure 1.4. Curved image sensors inspired by hemispherical retina.....	10
Figure 1.5. Optical components inspired by camera-type eyes.....	13
Figure 1.6. Structure of eyes.....	16
Figure 1.7. Epiretinal and subretinal prosthesis.....	19

Chapter 2

Figure 2.1. Ray tracing simulation of each optical system.....	30
Figure 2.2. Device array design with and without serpentine-shaped interconnection.....	31
Figure 2.3. High-density curved image sensor array based on the MoS ₂ -graphene heterostructure.....	43
Figure 2.4. The curved image sensor array on the concave and convex hemisphere.....	44
Figure 2.5. Circular film-type device array on the concave hemisphere.....	45
Figure 2.6. Device design and materials in the curved image sensor array.....	46

Figure 2.7. Characterization of synthesized MoS ₂ and graphene film.....	47
Figure 2.8. Fabrication of the phototransistor array based on the MoS ₂ -graphene heterostructure.....	48
Figure 2.9. Device characterization and imaging using the curved image sensor array.....	51
Figure 2.10. Integration of the curved image sensor array on the hemispherical surface.....	52
Figure 2.11. Characterization of the phototransistor array.....	53
Figure 2.12. Imaging results using the curved image sensor array.....	54
Figure 2.13. Experimental setup for imaging.....	55
Figure 2.14. Human-eye-inspired soft optoelectronic device.....	59
Figure 2.15. Schematic ocular structure implanted with retinal prostheses and the soft optoelectronic device.....	60
Figure 2.16. Eye model for analyzing the retinal deformation.....	61
Figure 2.17. Biocompatibility of the soft optoelectronic device.....	62
Figure 2.18. Soft flexible printed circuit board that integrates the CurvIS array with UNE.....	66
Figure 2.19. Retinal stimulation by the soft optoelectronic device.....	67

Chapter 3

Figure 3.1. Conventional wide angle multi-lens.....	78
Figure 3.2. Conventional bio-inspired imaging system.....	79

Figure 3.3. Structural and functional features of the aquatic vision in nature.....	89
Figure 3.4. Imaging parameters.....	90
Figure 3.5. Visual accommodation in aquatic vision.....	91
Figure 3.6. Tailored monocentric lens inspired by the protruding monocentric lens of aquatic eyes.....	94
Figure 3.7. Optimized design factor of the tailored monocentric lens.....	95
Figure 3.8. Theoretical analysis on the tailored monocentric lens.....	96
Figure 3.9. Optical simulation for visual accommodation of the tailored monocentric lens.....	97
Figure 3.10. Hemispherical silicon nanorod photodiode array inspired by the retina of aquatic eyes.....	101
Figure 3.11. Characterization of silicon nanorods.....	102
Figure 3.12. Optical characteristics of bare silicon and silicon nanorods.....	103
Figure 3.13. Light trapping by silicon nanorod structure.....	104
Figure 3.14. Device characterization of silicon nanorod photodiodes.....	105
Figure 3.15. Aquatic-vision-inspired imaging system.....	108
Figure 3.16. Integrated aquatic-vision-inspired imaging system.....	109
Figure 3.17. Experimental setup for the imaging demonstration.....	110
Figure 3.18. Imaging demonstration.....	111

Chapter 4

Figure 4.1. Imaging and data processing system.....	121
--	-----

Figure 4.2. Curved neuromorphic imaging device inspired by the human visual recognition system.....	128
Figure 4.3. Image acquisition and neuromorphic preprocessing based on the imaging and data processing system.....	129
Figure 4.4. MoS ₂ -pV3D3 phototransistor.....	134
Figure 4.5. Electrical characterization of the MoS ₂ -pV3D3 phototransistor.....	135
Figure 4.6. Photon-triggered neuromorphic behavior of the MoS ₂ -pV3D3 phototransistor.....	136
Figure 4.7. Photocurrent and decaying characteristics.....	137
Figure 4.8. Synaptic weight.....	138
Figure 4.9. Photocurrent generation in the pV3D3-PTr.....	139
Figure 4.10. Kelvin probe force microscopy.....	140
Figure 4.11. Analytical modeling of photoresponse.....	141
Figure 4.12. Analytical parameters of the MoS ₂ -pVD3 phototransistor.....	142
Figure 4.13. Image acquisition and neuromorphic preprocessing from noisy optical inputs.....	146
Figure 4.14. Curved neuromorphic imaging device.....	147
Figure 4.15. Neuromorphic image sensor array on planar substrate.....	148
Figure 4.16. Measurement setup.....	149
Figure 4.17. Neuromorphic imagery pattern recognition.....	150
Figure 4.18. Set of noisy images.....	151

List of Tables

Chapter 2

Table 2.1. Information of each lens component in the Double Gauss lens.....	32
Table 2.2. Information of the plano-convex lens in the optical characterization setup.....	33

Chapter 3

Table 3.1. Comparison of the aquatic-vision-inspired camera with the conventional wide field-of-view camera.....	80
Table 3.2. Information of the monocentric lens in the aquatic-vision-inspired optical system.....	83
Table 3.3. Information of each lens component in the conventional wide angle multi-lens.....	84
Table 3.4. Information of each lens component in the homogeneous ball lens.....	85

Chapter 1. Introduction

1.1 Structural and functional features of camera-type eyes

Humanity has devoted significant effort over a long time to advance imaging technologies capable of recording and/or detecting objects similar to human vision¹. Camera-related technologies have been matured continuously by imitating key features of the human eye, such as the lens and retina²⁻⁴. However, in terms of simplicity, miniaturization, energy efficiency, and functional aspects, conventional imaging technologies still have many challenges compared to the eyes in animals⁵⁻⁷. For example, the conventional cameras require complicated, bulky, and heavy multi-lens optics, typically consisting of 8-13 lenses, to correct the mismatch between flat imaging surface and the focal plane (*i.e.*, Petzval Surface)¹, whereas the natural eye enables aberration-free imaging using only a single lens^{2,8}.

In this regard, there have been many efforts to mimic the structural and functional features of eyes in nature⁹⁻¹¹. The eye of living organisms has been optimized through evolution over a long period¹². Figure 1.1 shows the evolution process of eyes, from single non-directional photoreceptor to high resolution vision¹. The eyes in nature began with the non-directional photoreceptor that enables simple monitoring of ambient light intensities (Class I; Figure 1.1a). This non-directional photoreceptor can only measure water depth or detect ultraviolet irradiation, both of which are far from imaging. After screening pigment is formed through long

evolution, the organisms can recognize directional light (Class II; Figure 1.1a), but they can only determine direction of incident light, which is still far from imaging. By forming aperture that blocks the unwanted incident lights, the animals could barely have low resolution vision (Class III; Figure 1.1a). However, their visual acuity is still poor to acquire useful visual information. Thus the animals evolve to have the focusing optics, such as lens in their eyes, and thereby most of vertebrate and aquatic animals finally have achieved high-resolution visions (Class IV; Figure 1.1a).

The camera-type eyes, found in vertebrate and aquatic animals, consists of a crystalline lens that focuses the image to the retina, an iris that controls the amount of entering light, and a hemispherically curved retina that recognizes the light and generates action potentials (Figure 1.2a). The hemispherical retina is entirely matched with the Petzval field surface formed by the crystalline lens, therefore imaging without optical aberrations is enabled (Figure 1.2b)⁴. In addition, the graded refractive index in crystalline lens reduces monochromatic/chromatic aberrations¹³, and active shape-variation by the ciliary body regulates the focal length for visual accommodation⁵. Using these attributes, the camera-type eyes features the miniaturized and simple optics¹, wide field-of-view (FoV)¹⁴, highly sensitive and efficient photo-detection¹⁵, deep depth-of-field (DoF)¹⁶, and facile accommodation¹⁷.

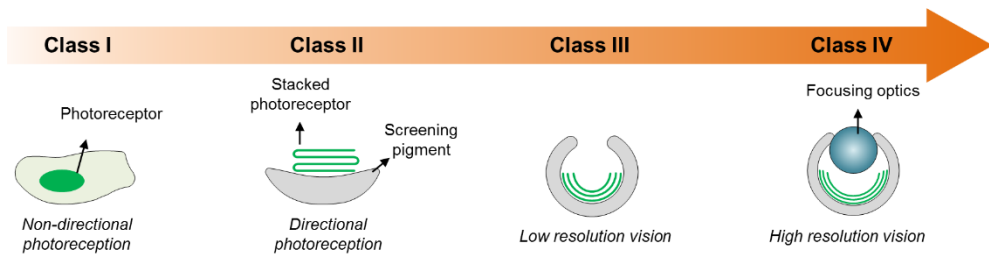


Figure 1.1. Evolution of camera-type eyes. Evolution of eyes from non-directional photoreceptors to high-resolution vision.

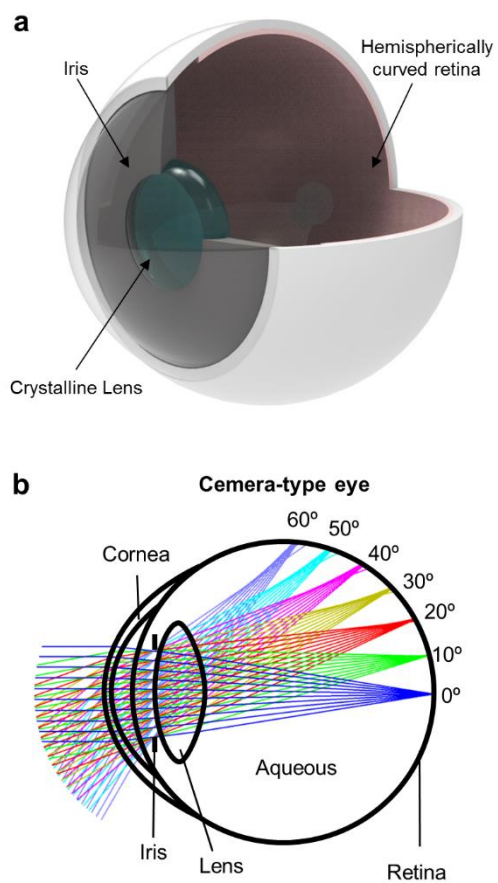


Figure 1.2. Schematic of camera-type eyes. (a) Schematic illustration of camera-type eyes consisting of the crystalline lens, the hemispherically curved retina, and the iris. **(b)** Ray-tracing simulation for an optical system of human eye with corneal.

1.2 Bio-inspired imaging system

The camera-type eye has simple configuration composed of a concavely hemispherical retina, a single lens, and light-management components for accommodation and adaptation. Over a past decade, there have been many efforts to imitate such features by developing the curved image sensor arrays, designing the graded refractive index (GRIN) lenses, and fabricating tunable lens and iris (Figure 1.3).

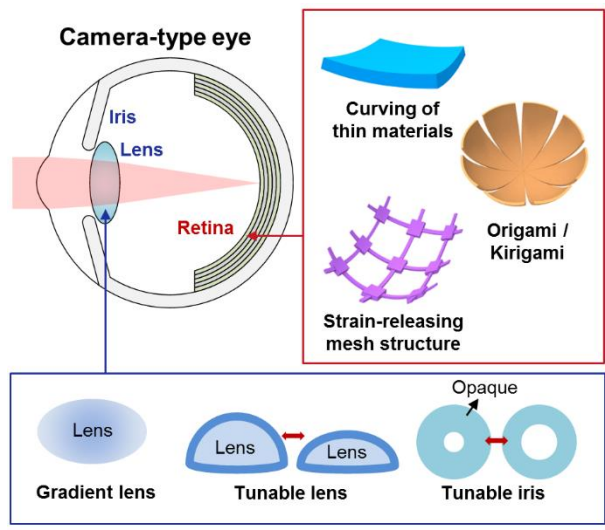


Figure 1.3. Device designs of camera-type eyes. Schematic illustration of major components of imaging system inspired by camera-type eyes.

1.2.1 Curved image sensor array inspired by the hemispherical retina

The curved configuration of hemispherical retina in camera-type eyes offers inspiration for reducing the complexity of optical systems. The incident light passing through a single lens forms the hemispherical focal plane¹⁴. However, current image sensor technologies are based on complementary metal-oxide semiconductor (CMOS) and charge-coupled device (CCD) architecture, which are rigid and flat. Therefore, for focusing the images onto the flat and rigid image sensors, the complicated multi-lens optics is required in the conventional cameras to flatten the focal plane¹. On the other hand, the hemispherical form of image sensors, inspired by the hemispherical retina, can be perfectly matched with the Petzval surface formed by the lens^{14,17}, thus enables aberration-free imaging with the single lens^{18,19}.

One strategy for mimicking curvilinear shape of retina is to employ thin and/or soft materials that offer mechanical deformability (Figure 1.4a). Thick single-crystalline silicon photodetectors, used in conventional cameras, is not deformable due to its high stiffness, low fracture toughness, and high modulus (2-5 GPa)²⁰. However, thin silicon membrane (25 μm thick) is mechanically flexible, thus can be curved to a radius less than 1 mm without mechanical fracture. Therefore the curved image sensor based on a bulky CMOS/CCD device is fabricated by thinning the silicon thickness, placing the thinly planar image sensor into a mold, and deforming via pneumatic pressure (Figure 1.4b)²⁰. However, such bulk curved image sensors still demand further improvements in terms of the coverage area and the radius of curvature (RoC) compared to the single-chambered eye systems. For example, the

retina in human eye covers most of the hemispherical chamber, and the RoC of the human eye is as small as 12 mm. Other strategies is to use intrinsically soft materials, such as inorganic nanomembranes^{3,8}, organics/polymers²¹⁻²³, and nanomaterials²⁴⁻²⁷. The soft materials provide high deformability, thus facilitates the fabrication of highly curved photodetector arrays (Figure 1.4c)²⁵.

However, the hemispherical deformation of the planar photodetector arrays, although it is mechanically flexible, is difficult because additional stretchability is required²⁸. By employing strain releasing/isolation device design, concavely curved photodetector arrays with complete coverage have been developed (Figure 1.4d)^{2,3}. The Si photodiode arrays is isolated into the islands, the metal interconnections connects the silicon photodiodes, and the polyimide encapsulation film is patterned as the mesh structure. Since most of strains are released into the deformable interconnections, the strain induced on the active silicon photodiode is much lower than the fracture strain of silicon. Therefore, inspired from the human eye, the electronic eye was fabricated using the concave mesh-structured photodetector array (Figure 1.4e)². This electronic eye showed high surface coverage, small RoC, and single lens optics. The RoC-tunable photodetector array is also demonstrated using the stretchable mesh-structured interconnections, which enables variable zoom in/out and excellent imaging characteristics (Figure 1.4f)³.

However, these mesh-structured interconnection designs take space, thus the density of image sensor array is limited. In this regard, origami/kirigami techniques is promising strategies for fabricating the high-density curved image sensor (Figure

1.4g). The thin Si nanomembrane-based photodiode array with a high-pixel density is patterned as an icosahedron pattern, and transferred to the hemispherical surface (Figure 1.4h)⁸. The Si photodetector array, patterned as petal design, also covers hemispherical surface without wrinkles (Figure 1.4i)⁹. Thin silicon whose thickness is less than 20 μm provides material flexibility and the tessellated hexagonal structures also allow mechanical flexibility, both of which are helpful for forming the hemispherical imager.

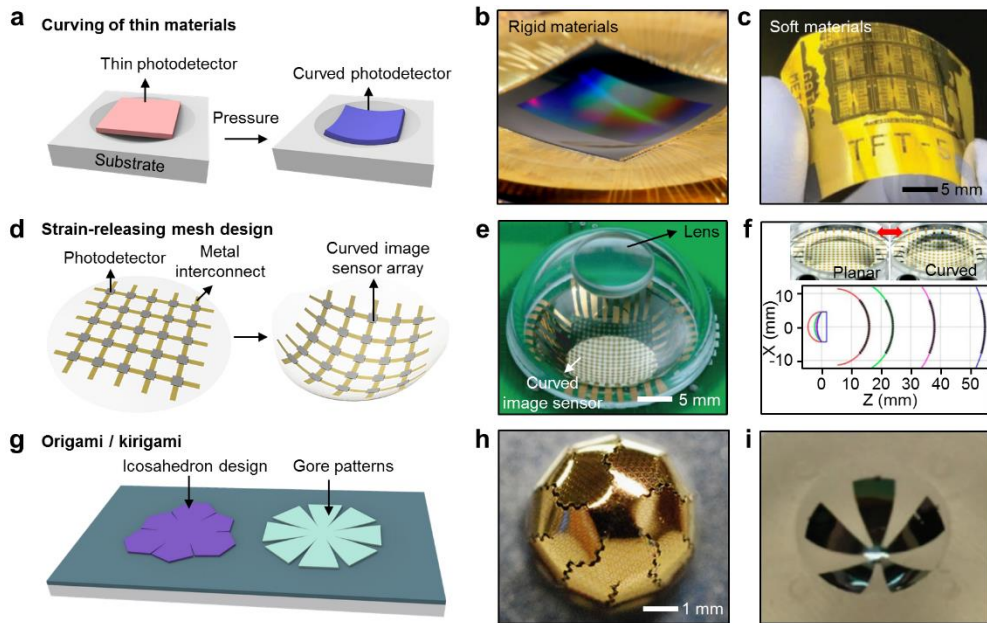


Figure 1.4. Curved image sensors inspired by hemispherical retina. (a) Schematic illustration of curving deformation method. (b,c) Photographs of the curved image sensor arrays based on thin rigid materials²¹ b and soft materials²⁵ c. (d) Schematic illustration of strain-releasing mesh structure. (e,f) Photographs of the human-eye-inspired curved image sensor arrays employing mesh-structured interconnection designs^{2,3}. (g) Schematic illustration of kirigami device designs. (h,i) Photographs of the curved image sensor arrays with icosahedron designs⁸ h and petal designs⁹ i.

1.2.2 Optical components inspired by camera-type eyes.

In most camera-type eyes, lens have graded refractive index profiles. It is because gradual distribution of refractive index of the lens corrects chromatic and monochromatic aberrations, while homogeneous lens shows large chromatic aberrations. The ray tracing analysis shows that the GRIN lens shows the smaller optical aberration compared the homogeneous lens (Figure 1.5a)²⁹. To mimic the crystalline lens, the GRIN lens needs a conical shape and radial index profile. Recently, human eye-inspired GRIN lens is fabricated using coextruded PMMA/SAN17 nanolayered optical film, whose gradual refractive index ranges from 1.489 to 1.573 (Figure 1.5b)¹³. The refractive index distribution of human's crystalline lens is in 1.37 to 1.41, whereas the GRIN lens has a higher refractive index as 0.12 than human's lens, but both of lenses shows similar gradual profile of refractive index. Aquatic animals have ball-lens with parabolic refractive index profile to obtain wide FoV focusing capabilities in underwater environment³⁰. The parabolic refractive index profile of the ball lens can eliminate the most of chromatic and monochromatic aberrations. With such advantages, the GRIN ball lens is also fabricated by stacking different nanolayered polymer (Figure 1.5c)³¹.

Visual accommodation, which enables image acquisition for the objects at different distance, is unique features of camera-type eyes (Figure 1.5d). The ciliary body deforms the lens shape by protracting/retracting the lens. There are two methods to mimic the ciliary body: 1) using a plastic ciliary body and elastomeric lens, and 2) fabricating shape-changeable lens. Liquid crystal elastomer (LCE) can be used as an

artificial ciliary body that controls the shape of the elastomeric lens (Figure 1.5e)³². LCE is the mixture of the elastomeric liquid crystal having the arranging properties by temperature change. The temperature variation significantly changes the length of elastomer, thus deforming the shape of the elastomeric lens by contraction and expansion. The shape-changeable lens is based on liquid-injectable lens. The liquid-based lens enables the aspherical shape lens that reduces longitudinal spherical aberration (Figure 1.5f)³³. The curvature of lens is deformed by applied electric fields, thus its focal length can be adjusted^{2,34}.

Excessively strong light can damage the retina, and weak light hinders object recognition. In camera-type eyes, the amount of incident light is controlled by the iris to adapt to light environment variation (Figure 1.5g)³⁵. The artificial iris that provide active adaption function was developed by employing thermally expanded LCE. In ambient condition, the LCE segments bend along with outer direction, thus the iris is opened (Figure 1.5h)³⁶. However, the LCD segment become bent in the opposite direction to the initial bending because the thermal energy induced by light irradiation creates the stress, thus iris is closed (Figure 1.5i)³⁶.

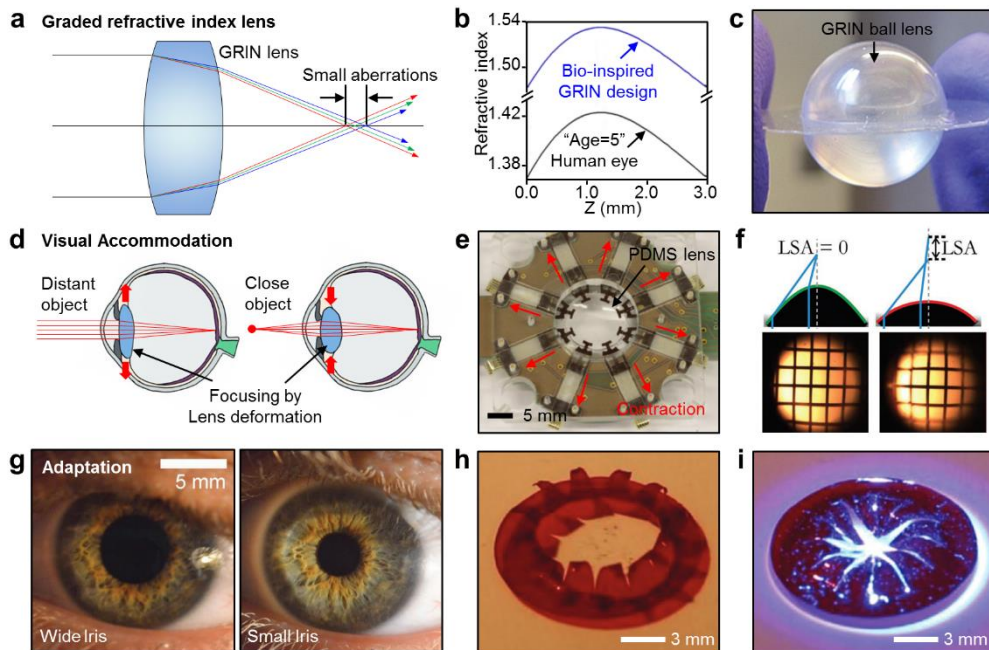


Figure 1.5. Optical components inspired by camera-type eyes. (a) Ray tracing simulation for GRIN lens. **(b)** Refractive index profile of a GRIN lens in comparison to the human eye lens¹³. **(c)** Photograph of GRIN ball lens³². **(d)** Schematic illustration of visual accommodation in human eye. **(e)** Photographs of LCE-actuated elastomeric lens³². **(f)** Cross-section view of a fluidically tunable lens³³. **(g)** Photographs of irises for adaption³⁵. **(h,i)** Photographs an artificial iris under wide **h** and narrow **i** states³⁶.

1.3 Retinal prosthesis

Another goal of the researches on bio-inspired imaging system is the development of a visual prosthesis. People recognize objects using their eyes. However, patients who suffer from retinal degeneration (*e.g.*, macular degeneration or retinitis pigmentosa) lose their vision because the degraded neurons in the retina cannot be activated by the external light³⁷. In the past few decades, many studies have reported the visual prostheses that complement the degenerated function of the retina and ultimately attempt to restore human vision³⁸. Among them, the retinal prosthesis that mimics the light recognition principles of the retina is the most prevalent prosthetic device because of the relatively easy surgery and the intuitive retinotopic mapping. The retina prosthesis consists of the image sensor array for recognizing incoming light, an electronic device for processing the optical information and generating programmed electrical pulses, and a microelectrode array for electrically stimulating the optic nerves.

1.3.1 The structure of eye and the principle of light recognition

In order to understand the working mechanism of a visual prosthesis, it is important to know the structure of the human eye and the principle of light recognition. The human eye consists of a cornea that protects the eyes from the external environment, a lens that focuses the image, an iris that controls the amount of incoming light, a sclera muscle that maintains the shape of the eye, and a retina that recognizes the light using the visual neurons (Figure 1.6a left)³⁹. Among these,

the neurons in the retina recognize the light and convert it into neural signals. The retina is composed of three layers of an outer nuclear layer (ONL), an inner nuclear layer (INL), and a ganglion cell layer (GCL) (Figure 1.6a right). Cones and rods, well-known photoreceptor cells, are distributed in the ONL. The INL contains horizontal cells, bipolar cells, and amacrine cells that transmit neural signals to the GCL. The GCL has retinal ganglion cells (RGC) that receive the signals from the bipolar cells and transmit action potentials to the visual cortex via the optic nerves.

Figure 1.6b shows the mechanism in which light is recognized by the retinal neurons⁴⁰. Photoreceptor cells in the ONL convert the incoming light into electrical and chemical signals through phototransduction. The generated signal is transferred to the RGC via the bipolar cells of the INL. The RGC collects the visual information obtained by various photoreceptors, analyzes and processes the information, and fires the optic nerves. Retinal degeneration usually occurs when the photoreceptor cells in the ONL become degraded.

Retinal prosthesis can restore vision by electrically stimulating the retinal neurons. Depending on the position where the device is implanted, the retinal prosthesis is divided into the epiretinal prosthesis, the subretinal prosthesis, the suprachoroidal prosthesis (Figure 1.6b bottom)³⁸. The epiretinal prosthesis, in which electrodes are attached on the GCL, directly stimulates the RGC^{41,42}. The subretinal prosthesis stimulates photoreceptor cells and/or bipolar cells using electrodes inserted between the ONL and the retinal pigment epithelium^{43,44}.

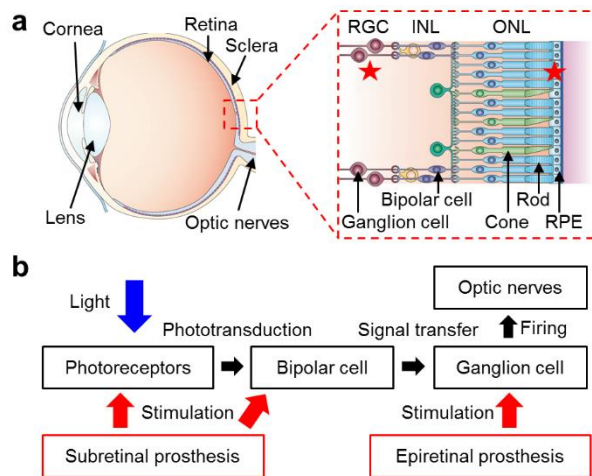


Figure 1.6. Structure of eyes. (a) Schematic illustration showing the structure of eyes⁴⁰. (b) Block diagram showing the principles of light recognition.

1.3.2 Configuration of the visusal prosthesis

Each visual prosthesis has unique advantages and limitations⁴⁵. The Argus II prosthetic system is the most advanced form of the epiretinal prosthesis^{41,42}. It consists of a head-mounted camera, a video processor, and an epiretinal electrode array (Figure 1.7a)⁴¹. The external camera mounted in a pair of glasses recognizes an image, and the video processor converts it to signals for retinal stimulation (Figure 1.7b)⁴². The converted information is wirelessly transmitted to the implanted electronics by an inductive coil, and is used to apply electrical stimulation to the RGC through 60 electrodes (Figure 1.7c)⁴². The epiretinal prosthesis can successfully restore vision even when bipolar cells or the RGC are injured because it directly stimulates the RGC and optic nerves. Due to direct stimulation of the RGC, however, the inner retinal processing by the bipolar cells and the RGC cannot be used. Therefore extra processing elements for generating programmed stimulation are needed. In addition, because the RGC requires high thresholds to be stimulated, the stimulation of the RGC can also stimulate the axons. This axonal stimulation hinders the implementation of high visual acuity by spreading electrical stimulation widely⁴⁶. In last, the hardware of epiretinal prostheses needs further improvements. When people see an object, the stability of the image is improved through feedback between the visual information perceived by the eye and the motion of the muscles around the eye, known as efference copy. However, the external camera in the glasses prevents the efference copy, resulting in the image fading^{47,48}.

The subretinal prosthesis can be applied to patients whose photoreceptors

are degenerated but whose bipolar cells and RGC are intact⁴⁹. Alpha-IMS is a European-approved subretinal prosthetic device. The Alpha-IMS system consists of an antenna and electronics to receive the power and the controlling commands from outside, a sclera fixation that fixes the device to the eye bulb, and a subretinal chip that detects the external light and applies electrical stimulation (Figure 1.7d and 1.7e)⁴⁶. The subretinal chip has 1,500 pixels, each of which contains a photodiode, an amplifier, and an electrode⁴⁴. When the photodiode recognizes the light coming from the outside, the electronics containing the amplifier generates the electrical pulse and the electrode on the same pixel stimulates the photoreceptor cells (Figure 1.7f)⁴⁴. The produced action potentials are collected and processed by the healthy RGC, and are transferred to the visual cortex via the optic nerves. Given that light recognition, processing, and electrical stimulation are done in the subretinal chip, the Alpha-IMS can reduce the number of wires and realize a high-density pixel array. Due to low threshold for subretinal stimulation, focal stimulation is also available. However, retinal detachment caused by the implantation surgery results in further degradation of live photoreceptors^{50,51}. Moreover, because the subretinal space is narrow, the size of the device is limited. Therefore, the device covers a small area of the retina, limiting the FoV⁴³.

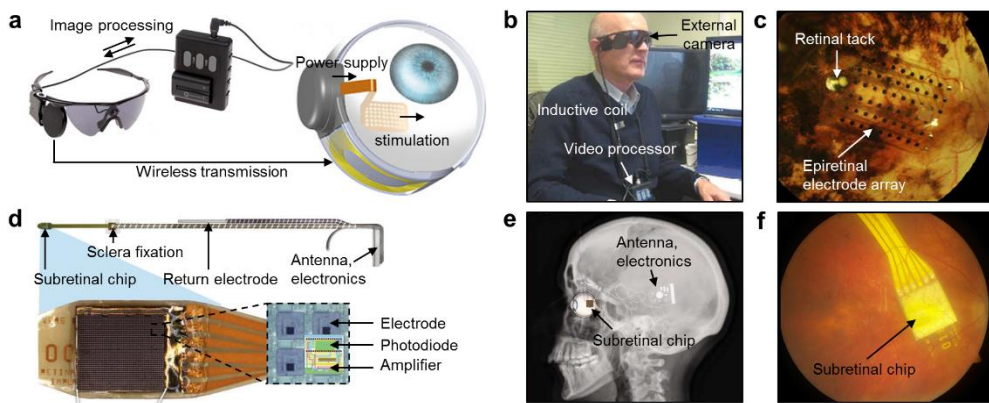


Figure 1.7. Epiretinal and subretinal prosthesis. (a) Schematic image of Argus II system⁴¹. (b) Photograph of the patient with Argus II system⁴². (c) Optical microscope image of the retina implanted with the epiretinal electrode array⁴². (d) Photograph of Alpha-IMS⁴⁵. (e) X-ray image of the patient with Alpha-IMS⁴⁵. (f) Optical microscope image of the retina implanted with the subretinal chip⁴⁴.

1.4 Conclusion

Many scientists and engineers have continuously pursued mimicking of biological eyes in nature to implement optically outstanding and remarkably compact imaging devices. These efforts have resulted in significant progress in the imaging industries as well as emerging fields such as robotics and prosthetics. Although recent progress in bio-inspired imaging systems has yielded significant advances, conferring the novel functionalities to the image sensors would provide new paradigms for advanced imaging technologies. For example, ultrathin thickness of curved image sensor array allows the development of soft and biocompatible retinal implants. In another examples, wide FoV, deep DoF, and small form factor would be helpful for the mobile optoelectronic devices, and neuromorphic preprocessing functions would be crucial for efficient image-based applications. In this regard, I have developed the ultrathin curved image sensor array based on the MoS₂-graphene heterostructure, the aquatic-vision-inspired wide FoV camera, and the curved neuromorphic image sensor array inspired by the human visual recognition system for the advanced imaging technologies.

1.5 Reference

* Some contents of this chapter were published in *Advanced Functional Materials* (2018, 28, 1705202)

1. Lee, G. J., Choi, C., Kim, D.-H. & Song, Y.-M. Bioinspired artificial eyes: optic components, digital cameras, and visual prostheses. *Adv. Funct. Mater.* **28**, 1705202 (2018).
2. Jung, I. *et al.* Dynamically tunable hemispherical electronic eye camera system with adjustable zoom capability. *Proc. Natl. Acad. Sci. USA* **108**, 1788-1793 (2011).
3. Ko, H. C. *et al.* A hemispherical electronic eye camera based on compressible silicon optoelectronics. *Nature* **454**, 748-753 (2008).
4. Choi, C. *et al.* Human eye-inspired soft optoelectronic device using high-density MoS₂-graphene curved image sensor array. *Nat. Commun.* **8**, 1664 (2017).
5. D. Atchison, G. Smith, *Optics of the Human Eye*, Butterworth-Heinemann, Oxford, UK (2000).
6. Posch, C., Serrano-Gotarredona, T., Linares-Barranco, B. & Delbruck, T. Retinomorphic event-based vision sensors: bioinspired cameras with spiking output. *Proc. IEEE* **102**, 1470-1484 (2014).
7. Ahn, J. *et al.* Advanced image sensor technology for pixel scaling down toward 1.0 μm . in *IEEE Int. Electron Devices Meeting*, IEEE, San Francisco, CA, USA (2008).

8. Zhang, K. *et al.* Origami silicon optoelectronics for hemispherical electronic eye systems. *Nat. Commun.* **8**, 1782 (2017).
9. Wu, T., *et al.* Design and fabrication of silicon-tessellated structures for monocentric imagers. *Microsyst. Nanoeng.* **2**, 16019 (2016).
10. Song, Y. M., *et al.* Digital cameras with designs inspired by the arthropod eye. *Nature* **497**, 95-99 (2013).
11. Jeong, K.-H., Kim, J. & Lee, L. P. Biologically inspired artificial compound eyes. *Science* **312**, 557-561 (2006).
12. Nilsson, D.-E. Eye evolution and its functional basis. *Visual Neurosci.* **30**, 5-20 (2013).
13. Ji, S. *et al.* A bio-inspired polymeric gradient refractive index (GRIN) human eye lens. *Opt. Express* **20**, 26746-26754 (2012).
14. Rim, S.-B., Catrysse, P. B., Dinyari, R., Huang, K., & Peumans, P. The optical advantages of curved focal plane arrays. *Opt. Express* **16**, 4965-4971 (2008).
15. Wagner, H.-J., Frohlich, E., Negishi, K. & Collin, S. P. The eyes of deep-sea fish II. Functional morphology of the retina. *Prog. Retin. Eye Res.* **17**, 637-685 (1998).
16. Charman, W. N. & Tucker, J. The optical system of the goldfish eye. *Vision Res.* **13**, 1-8 (1973).
17. Lee, G. J., Nam, W. I. & Song, Y. M. Robustness of an artificially tailored fisheye imaging system with a curvilinear image surface. *Opt. Laser Technol.* **96**, 50-57 (2017).
18. Xu, F., Huang, W. J., Liu, J. & Pang, W. Design of lenses with curved Petzval

- image surfaces. *J. Mod. Opt.* **63**, 2211-2219 (2016).
19. Dumas, D., Fendler, M., Baier, N., Primot, J. & Coarer, I. E. Curved focal plane detector array for wide field cameras. *Appl. Opt.* **51**, 5419-5424 (2012).
 20. Guenter, B. *et al.* Highly curved image sensors: a practical approach for improved optical performance. *Opt. Express* **25**, 13010-13034 (2017).
 21. Xu, X., Mihnev, M., Taylor, A. & Forrest, S. R. Organic photodetector arrays with indium tin oxide electrodes patterned using directly transferred metal masks. *Appl. Phys. Lett.* **94**, 043313 (2009).
 22. Xu, X., Davanco, M., Qi, X. & Forrest, S. R. Direct transfer patterning on three dimensionally deformed surfaces at micrometer resolutions and its application to hemispherical focal plane detector arrays. *Org. Electron.* **9**, 1122-1127 (2008).
 23. Liu, X., Lee, E. K., Kim, D. Y., Yu, H. & Oh, J. H. Flexible organic phototransistor array with enhanced responsivity via metal-ligand charge transfer. *ACS Appl. Mater. & Interfaces* **8**, 7291-7299 (2016).
 24. Fan, D., Lee, K. & Forrest, S. R. Flexible thin-film InGaAs photodiode focal plane array. *ACS Photonics* **3**, 670-676 (2016).
 25. Seo, J.-H. *et al.* Flexible phototransistors based on single-crystalline silicon nanomembranes. *Adv. Opt. Mater.* **4**, 120-125 (2016).
 26. Li, L., Gu, L., Lou, Z., Fan, Z. & Shen, G. ZnO quantum dot decorated Zn₂SnO₄ nanowire heterojunction photodetectors with drastic performance enhancement and flexible ultraviolet image sensors. *ACS Nano* **11**, 4067-4076 (2017).
 27. Lim, S. *et al.* Broadband omnidirectional light detection in flexible and

- hierarchical ZnO/Si heterojunction photodiodes. *Nano Res.* **10**, 22-36 (2017).
28. Kim, J. *et al.* Stretchable silicon nanoribbon electronics for skin prosthesis. *Nat. Commun.* **5**, 5747 (2014).
 29. Zuccarello, G., Scribner, D., Sands, R. & Buckley, L. J. Materials for bio-inspired optics. *Adv. Mater.* **14**, 1261-1264 (2002).
 30. Jagger, W. S. & Sands, P. J. A wide-angle gradient index optical model of the crystalline lens and eye of the rainbow trout. *Vision Res.* **36**, 2623-2639 (1996).
 31. Ji, S. *et al.* Polymeric nanolayered gradient refractive index lenses: technology review and introduction of spherical gradient refractive index ball lenses. *Opt. Eng.* **52**, 112105 (2013).
 32. Petsch, S., Schuhladen, S., Dreesen, L. & Zappe, H. The engineered eyeball, a tunable imaging system using soft-matter micro-optics. *Light: Sci. Appl.* **5**, e16068 (2016).
 33. Mishra, K. *et al.* Optofluidic lens with tunable focal length and asphericity. *Sci. Rep.* **4**, 6378 (2014).
 34. Moran, P. M. *et al.* Fluidic lenses with variable focal length. *Appl. Phys. Lett.* **88**, 041120 (2006).
 35. Schuhladen, S. *et al.* Iris-like tunable aperture employing liquid-crystal elastomers. *Adv. Mater.* **26**, 7247-7251 (2014).
 36. Zeng, H., Wani, O. M., Wasylczyk, P., Kaczmarek, R. & Priimagi, A. Self-regulating iris based on light-actuated liquid crystal elastomer. *Adv. Mater.* **29**, 1701814 (2017).

37. Duncan, J. L. *et al.* High-resolution imaging with adaptive optics in patients with inherited retinal degeneration. *Invest. Ophthalmol. Visual Sci.* **48**, 3283-3291 (2007).
38. Chuang, A. T., Margo, C. E. & Greenberg, P. B. Retinal implants: a systematic review. *Br J. Ophthalmol.* **98**, 852-856 (2014).
39. Zhang, K., Zhang, L. & Weinreb, R. N. Ophthalmic drug discovery: novel targets and mechanisms for retinal diseases and glaucoma. *Nat. Rev. Drug Discovery* **11**, 541-559 (2012).
40. Zrenner, E. Will retinal implants restore vision? *Science* **295**, 1022-1025 (2002).
41. Dagnelie, G. *et al.* Performance of real-world functional vision tasks by blind subjects improves after implantation with the Argus II retinal prosthesis system. *Cli. Exp. Ophthalmol.* **45**, 152-159 (2017).
42. Cruz, d. L. *et al.* The Argus II epiretinal prosthesis system allows letter and word reading and long-term function in patients with profound vision loss. *Br J. Ophthalmol.* **97**, 632-636 (2013).
43. Zrenner, E. *et al.* Subretinal electronic chips allow blind patients to read letters and combine them to words. *Proc. R. Soc. B* **278**, 1489-1497 (2011).
44. Stingl, K. *et al.* Subretinal visual implant Alpha IMS-clinical trial interim report. *Vision Res.* **111**, 149-160 (2015).
45. Zrenner, E. Fighting blindness with microelectronics. *Sci. Transl. Med.* **5**, 210ps16 (2013).
46. Weitz, A. C. *et al.* Improving the spatial resolution of epiretinal implants by

- increasing stimulus pulse duration. *Sci. Transl. Med.* **7**, 318ra203 (2015).
47. Villalobos, J. *et al.* A wide-field suprachoroidal retinal prosthesis is stable and well tolerated following chronic implantation. *Invest. Ophthalmol. Visual Sci.* **54**, 3751-3762 (2013).
 48. Dowling, J. Current and future prospects for optoelectronic retinal prostheses. *Eye* **23**, 1999-2005 (2009).
 49. MacLaren, R. E. Electronic retinal implant surgery. *Eye* **31**, 191-195 (2017).
 50. Mandel, Y. *et al.* Cortical responses elicited by photovoltaic subretinal prostheses exhibit similarities to visually evoked potentials. *Nat. Commun.* **4**, 1980 (2013).
 51. Ayton, L.N. *et al.* First-in-human trial of a novel suprachoroidal retinal prosthesis. *PLoS ONE* **9**, e115239 (2014).

Chapter 2. Human-eye-inspired soft optoelectronic device using high-density MoS₂-graphene curved image sensor array

2.1 Introduction

Soft bioelectronic devices¹⁻³, employing soft materials⁴⁻⁶ and/or ultrathin device designs⁷⁻⁹, have attracted significant attention particularly in implantable device applications¹⁰. For instance, the silicone-encapsulated soft neural implant effectively stimulates spinal cord to rehabilitate the disabled leg¹, and ultrathin prosthetic skin connected to peripheral nerves perceives external mechanical/thermal signals and transfers the corresponding signals to brain^{11,12}. Likewise, the soft bioelectronic device can play an important role in the intraocular retinal prosthesis for patients with retinal degeneration (*e.g.*, macular degeneration or retinitis pigmentosa). As the optic nerves widely spread in the soft (~ 20 kPa)¹³ and hemispherically-shaped retina, a soft and curved form of the high-density image sensor and electrode array which mechanically matches with the human retina is significantly needed particularly for the long-term retinal prosthesis. Conventional wafer-based rigid and planar imaging modules, however, are far from this goal because i) lamination of planar devices can cause the retinal deformation¹⁴, ii) stiff devices can damage the non-regenerative optic nerves¹⁵, and iii) bulky multi-lens

optics is required to focus on the flat image sensor (Figure 2.1a and Table 2.1).

Recently, new image sensor arrays based on novel materials^{16,17} and device designs¹⁸⁻²¹ have been proposed. Among these, hemispherically curved image sensor (CurvIS) arrays have gained particular attention, since they can achieve the aberration-free imaging¹⁸ (Figure 2.1b and Table 2.2) and the wide field-of-view¹⁹. These CurvIS arrays have employed distinctive interconnect designs (*e.g.*, pop-up¹⁸ and/or serpentine-shaped¹⁹ structures) to absorb bending induced strains in the rigid silicon-based photodetector array. However, these interconnect designs take space and hence limit the density of the image sensor array (Figure 2.2). A relatively high-density cylindrical silicon image sensor array was reported²⁰, but the unidirectionally curved imager cannot provide all benefits of the omnidirectionally curved system^{18,19}. Ultrathin MoS₂²², an inherently soft two-dimensional (2D) nanomaterial^{23,24}, is a promising candidate of a photo-absorbing component in the high-density omnidirectional CurvIS array attributing to its unique advantages, such as the superb photo-absorption coefficient ($>5 \times 10^7 \text{ m}^{-1}$)²⁵, photoresponsivity (2200 A W^{-1})²⁶, and high fracture strain ($\sim 23\%$)²³. The softness^{23,27} and ultrathin thickness^{28,29} of MoS₂ are additional factors that enable the fabrication of the soft optoelectronic device. However, an ultrasoft MoS₂-based multicell optoelectronic device that can capture images on the hemispherical surface and its application to soft bioelectronics have not been reported yet.

Here, we present an ultrasoft and high-density curved MoS₂-graphene photodetector array using single-lens optics. Unique advantages of the soft

omnidirectional CurvIS array include the high-density array design, small optical aberration, and simplified optics. The MoS₂-graphene-based CurvIS array shows much lower induced strain than the fracture strain of composing materials because of the ultrathin thickness and softness of 2D materials^{23,30}. In addition, the truncated icosahedron design (fullerene-like structure) and the strain-isolation device design enable the CurvIS array to have an almost complete coverage on the hemispherical surface. The high-density MoS₂-graphene CurvIS array successfully recognizes various projected images without infrared (IR) noise. It is the first attempt to achieve high-quality imaging using the ultrathin MoS₂-based optoelectronic device in a hemispherically curved format with the single lens optics. Then we propose a human-eye-inspired soft implantable optoelectronic device consisting of the CurvIS array and ultrathin neural-interfacing electrodes (UNE) by mimicking structural features of the human eye. A soft and flexible image processing unit is also introduced to construct the fully integrated soft implantable electronic system. The soft CurvIS array and UNE system minimizes mechanical distortion of the retina and effectively stimulates the retinal nerves in response to external optical signals.

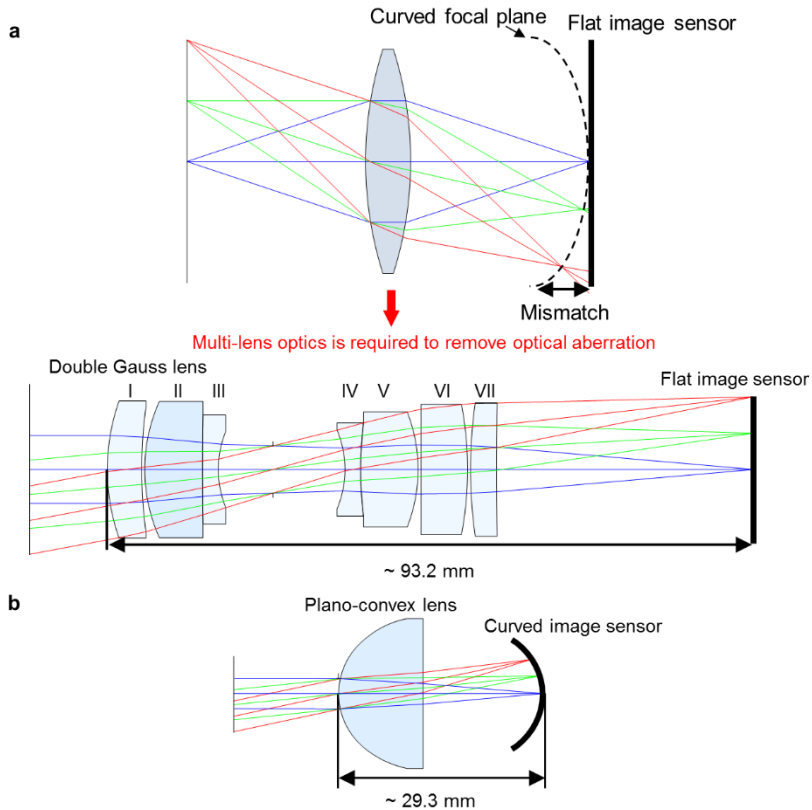


Figure 2.1. Ray tracing simulation of each optical system. (a) Optical aberration originated from the mismatch between the curved focal plane and the flat image sensor (top). Conventional Double Gauss lens to remove optical aberration for the flat image sensor (bottom). **(b)** Simplified optics consisting of a single plano-convex lens for the curved image sensor.

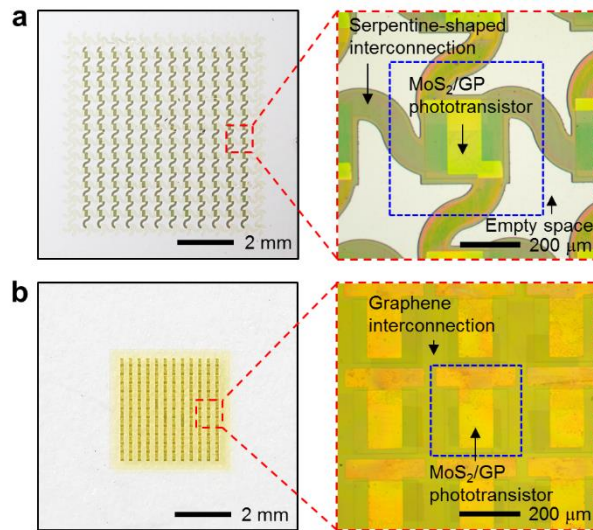


Figure 2.2. Device array design with and without serpentine-shaped interconnection. (a) Image of the device array with serpentine-shaped interconnections (left) and its magnified view (right). (b) Image of the compact device array without serpentine-shaped interconnections (left) and its magnified view (right). Blue dashed box indicates a single pixel.

Table 1 Lens information of Double Gauss lens.					
Surface	Label of lens	Radius (mm)	Thickness (mm)	Material	Semi-diameter (mm)
Object		Infinity	Infinity	-	Infinity
1	I	34.333	4.435	N-BASF2	10.061
2		78.925	0.381	-	9.193
3	II	27.554	7.452	N-LAK8	10.000
4	III	592.999	2.032	SF2	8.000
5		16.807	7.036	-	5.625
Stop		Infinity	9.276	-	3.471
7	IV	-16.965	2.032	SF2	5.784
8	V	69.433	7.394	N-LAK33	6.843
9		-25.644	0.381	-	8.454
10	VI	Infinity	5.989	N-LAK33	8.888
11		-58.641	0.381	-	9.579
12	VII	79.263	3.348	N-LAK8	9.771
13		699.404	33.035	-	9.797
Image		Infinity	-	-	10.679

Table 2.1. Information of each lens component in the Double Gauss lens. The radii, thicknesses, materials, and semi-diameters of each lens used in the Double Gauss lens.

Table 2 Lens information of measurement setup				
Surface	Radius (mm)	Thickness (mm)	Material	Semi-diameter (mm)
Object	Infinity	Infinity	-	Infinity
Stop	Infinity	0.000	-	2.532
1	13.127	12.220	N-BK7	12.700
2	Infinity	17.045	-	3.653
Image	-11.340	-	-	9.500

Table 2.2. Information of the plano-convex lens in the optical characterization setup. The radii, thicknesses, materials, and semi-diameters of lens used in the optical system for the CurvIS array.

2.2 Experimental section

2.2.1 Synthesis of the ultrathin MoS₂ film

An ultrathin MoS₂ film was synthesized on a SiO₂ wafer using CVD. Crucibles containing 0.1 g sulphur (Alfa, USA) and 0.3 g MoO₃ (Sigma Aldrich, USA) were placed at the upstream and centre of the chamber, respectively. The growth substrate was treated using the piranha solution and oxygen plasma, and placed at the downstream of the MoO₃ crucible. The chamber was annealed at 150 °C before the synthesis. The chamber was heated at a rate of 25 °C min⁻¹, and maintained at 650 °C and 10 torr with Ar flow of 50 sccm for 5 minutes. The temperature of sulphur was maintained at 160 °C during the reaction. The chamber was naturally cooled after the reaction was complete. A Raman spectrum of the synthesized MoS₂ film was analysed using T64000 (Horiba, Japan) at NCIRF.

2.2.2 Synthesis of the ultrathin graphene film

A graphene film was synthesized using the chemical vapour deposition (CVD). A 25 nm-thick copper foil (Alfa Aesar, USA) was cleaned with isopropyl alcohol and annealed at 1,000 °C for 30 min under constant H₂ flow (8 sccm, 0.08 Torr). After 30 minutes annealing, additional CH₄ flow (20 sccm, 1.6 Torr) was introduced for 20 minutes at 1,000 °C. When the synthetic procedure was finished, the chamber was rapidly cooled to room temperature under H₂ flow (8 sccm, 0.08 Torr). The synthesized graphene film is analysed by Raman spectroscopy.

2.2.3 Fabrication and characterization of the CurvIS array

The fabrication process of the CurvIS array began with spin-coating of a thin PI film (420 nm, bottom encapsulation; Sigma Aldrich, USA) on a SiO₂ wafer. A thin layer of Si₃N₄ (5 nm, substrate) was deposited using the plasma-enhanced CVD. Using photolithography and dry etching, an island-shape array of the Si₃N₄ film was defined. The graphene layer (2 nm) was transferred onto the Si₃N₄ layer and patterned as an interdigitated source/drain electrode whose channel length is 10 μm. The ultrathin MoS₂ layer (4 nm, photo-absorbing layer) was transferred onto the graphene electrodes, and patterned by photolithography and reactive ion etching. Ti/Au layer (5 nm/10 nm) was deposited for the etch mask and used as probing pads. The Al₂O₃ dielectric layer (25 nm) was deposited at 200 °C through the thermal atomic layer deposition. The Al₂O₃ layer was etched with a buffered oxide etchant after photolithography as an island-shape array. Then lift-off process was used to pattern the Ti/Au layer (5 nm/10 nm, gate electrode) deposited by the thermal evaporation. Additional spin-coating of a thin PI film (420 nm, top encapsulation) and dry etching completed fabrication of the phototransistor array with a truncated icosahedron design. The truncated icosahedron structure is an Archimedean solid made by cutting out the corners of a regular twenty-sided face and composed of 12 pentagons and 20 hexagons. Its shape is similar with the Telstar soccer ball and fullerene (C₆₀). We utilized the partial structure of the truncated icosahedron design to minimize the induced mechanical stress on the hemispherical surface. The fabricated phototransistor array was detached from the SiO₂ wafer with a water-soluble tape

(3M Corp., USA). This tape was cut into the truncated icosahedron design. The detached phototransistor array was transfer-printed onto the polydimethylsiloxane (PDMS; Dow Corning, USA) hemispherical dome.

2.2.4 Comparison of photoresponsivity between the MoS₂-graphene phototransistor and the silicon photodiode with the same thickness

The silicon photodiode consists of single crystal silicon 1.25 μm -thick PN junction. The fabrication of the film-type silicon photodiode array began with spin-coating of the precursor solution of the thin PI film (420 nm) on a SiO₂ wafer. 1.25 μm -thick Si nano-membranes were prepared from the silicon-on-insulator wafer (SOITEC, France), which was doped by boron and phosphorous in advance, and then transferred to the prepared PI film. Each photodiode pixel was fabricated by photolithography and dry etching. Additional spin-coating of a thin PI film (420 nm, top encapsulation) and following photolithography and dry etching completed fabrication of the film-type device array. Since the photoresponsivity of silicon is proportional to the thickness, the theoretical photoresponsivity of 3 nm-thick silicon photodiode was calculated by dividing the photoresponsivity of 1.25 μm -thick silicon device by the thickness. The estimated photoresponsivity of the silicon device was compared to that of the MoS₂-graphene-based phototransistor.

2.2.5 Customized imaging setup for the CurvIS array

A white light-emitting diode (LED; Advanced Illumination, USA) blocked

with a metal shadow mask generated the patterned light, the aperture controlled the quantity of the passed light, and the plano-convex lens focused the light on the CurvIS array. The CurvIS array was constructed on a transparent convex hemispherical dome composed of PDMS. Since the patterned light is illuminated from the bottom side, passed through the transparent PDMS support of the convex shape, and then reached the CurvIS array, the CurvIS array on the convex hemisphere can be considered as a concavely curved imager. The calibrated 12×12 phototransistor array located at the centre of the CurvIS array acquired the focused light pattern. The light intensity incident on each pixel was individually measured by probing tips with a parameter analyser (B1500A; Agilent, USA), and then the pixelated image was processed by applying the interpolation function of Matlab (MathWorks, USA). The averaged values of neighbouring cells were used for dead pixels. All the captured images were rendered on a concave hemisphere.

2.2.6 Characterization of mechanical deformation of the eye model by the implanted devices

To mimic the structure of retina and sclera, an eye model, a double-layered hemispherical PDMS shell, was fabricated; PDMS layers with different modulus (40 kPa and 1.2 MPa) were sequentially coated on the hemispherical mould, cured, and detached from the mould. Three kinds of implantable devices (*i.e.*, soft optoelectronics, flexible film-type device, and wafer-based electronics) were attached onto the concave surface of the eye model, and three-dimensional deformations of

the eye models were observed by a micro computed tomography (micro CT, Viva CT 80; Scanco Medical, Swiss).

2.2.7 Fabrication of the UNE

The UNE fabrication began with spin-coating of the PI film (420 nm) on a SiO₂ wafer. A lift-off process was used to pattern Cr/Au layer (7 nm/40 nm) and Pt layer (25 nm) deposited by thermal evaporation and sputtering, respectively. Additional spin-coating of PI film (420 nm) and dry etching completed fabrication of the UNE. The electrode of the low impedance (1.31 k Ω at 1 kHz) was used for the neural stimulation.

2.2.8 Animal preparation for the *in vivo* experiment

In this study, we used male Wistar rats whose weights are in the range of 280–300 g (Japan SLC; Hamamatsu, Japan). The animals were caged at the temperature of 22–24 °C with a 12/12 hr light/dark cycle. The rats were given at least 1 week to adapt to their environment before experiments. The Institutional Animal Care and Use Committee at the Korea Basic Science Institute (KBSI-AEC 1601) reviewed and approved this study. All animal procedures were in accordance with the Guide for the Care and Use of Laboratory Animals issued by the Laboratory Animal Resources Commission of KBSI.

2.2.9 *In vivo* animal experiment to confirm biocompatibility of the soft

optoelectronic device

The rat's eye in which soft optoelectronic device is implanted for 7 days was compared with the normal eye. The soft optoelectronic device is implanted into the eye by minimally invasive surgery. Antibiotics and dexamethasone were treated to prevent inflammation by the surgical procedures. The eyes were fixed at 4% paraformaldehyde solution, were embedded in paraffin, and were sliced at coronal plane to 5 μm thickness by a microtome. These sliced tissues were mounted on slide glasses, and stained with Hematoxylin-Eosin (MHS16, HT110180, Sigma Aldrich, USA) by following the standard histochemical procedures. We also utilized 4',6-diamidino-2-phenylindole (DAPI; Vectors Laboratories, USA), FGF2 (1:200, Santa Cruz biotechnology, USA), and GFAP (1:800, Santa Cruz biotechnology, USA) staining by following the standard protocol to obtain fluorescence imaging data of key factors related with retinal biocompatibility. Histofluorescence images were obtained by a confocal microscope (LSM 780 NLO, Carl Zeiss, Germany).

2.2.10 *In vivo* animal experiment for the retinal stimulation

This study compared optical and electrical stimulation to retina of a healthy rat. The rat was fixed in a stereotaxic frame. A commercial white LED was fixed in front of the eyeball and delivered light for the optical stimulation. Lensectomy was performed to conformally attach the UNE onto the retina. The extraocular light detection was performed to prevent the activation of the healthy retina and the signal interference by external light. MoS₂-graphene-based phototransistors generated

photocurrent by the illuminated light, and the photocurrent was amplified by the external amplifier. The data acquisition system detected the amplified photocurrent and triggered a function generator. The function generator applied biphasic electrical pulses (80 μ A, 50 μ s, and 20 Hz) to the retinal nerves via a single-channel UNE. The optical and electrical stimulations were repeated at least 20 times for statistical analyses. To record the neural responses by the stimulations, Parylene-C insulated tungsten microelectrodes (\sim 1 M Ω at 1 kHz, 100 μ m diameter) were inserted into the primary visual cortex (7.0 mm posterior to bregma, 3.0–4.0 mm lateral to the midline, 800–1000 μ m ventral to dura mater) and frontal lobe (Supplementary Fig. 16c). The neural signal was filtered between 0.3 and 10 kHz and sampled at 25 kHz. The neural signals were separated into spikes and LFPs by 300 Hz high- and 100 Hz low-pass filter, respectively. To remove the stimulation artefacts and detect spikes, the curve-fitting method was used. Time-frequency analysis was performed to allow tracking of the time-varying energy in the frequency band of the LFP signals. In order to visualize the time-varying energy, we calculated the spectrograms that were baseline-corrected and averaged across all trials.

2.3 Result and discussion

2.3.1 Materials and device designs for the high-density curved image sensor array

Figure 2.3a, 2.3b show a schematic illustration and a corresponding image of the MoS₂-graphene-based high-density CurvIS array. The light signal is focused by the plano-convex lens and measured by the CurvIS array. Constructing a high-density image sensor array on the hemispherical surface (Figure 2.4) to achieve optical advantages (Figure 2.1) requires development of a novel soft photodetector array. When a conventional film-type image sensor array is laminated on the hemispherical dome, for example, the bending induced strain causes folds and wrinkles in the array that dramatically increase the chance of mechanical failures in devices (Figure 2.5). On the other hand, the high-density CurvIS array can be fabricated on the hemisphere without mechanical fractures (Figure 2.4 and Figure 2.6c) by introducing the ultrathin device structure (51 nm; Figure 2.6a and 2.6b), using inherently soft materials (MoS₂²³ and graphene³⁰; Figure 2.7), applying a strain-isolation device design³¹ (isolation of Al₂O₃ and Si₃N₄; Figure 2.6a, 2.6a inset, and Figure 2.8), and introducing a truncated icosahedron design (Figure 2.3). The resulting CurvIS array successfully visualizes the focused optical image (*e.g.*, university logo; inset of Figure 2.3b).

The phototransistor array is composed of a MoS₂-graphene heterostructure (6 nm; synthesis process in Methods) and other nanomembranes (Al₂O₃ dielectric (25 nm), Ti/Au gate (5 nm/10 nm), and Si₃N₄ substrate (5 nm)). As shown in Figure 2.6b,

the layer number of the MoS₂ and graphene are six and four, respectively. The entire thickness of the device is 51 nm (Figure 2.6a and 2.6b), which is much thinner than conventional silicon-based photodetectors whose thickness is in the range of micrometers or thicker. Top and bottom polyimide (PI) encapsulations (420 nm each) protect the device. The ultrathin thickness of the device dramatically decreases the bending induced strain in the curved system^{7,8}. Furthermore, MoS₂ and graphene, which are used as a photo-absorbing layer and interconnection, respectively, have the much higher fracture strain (~23% and ~25%, respectively)²³ than silicon (~1%)³². Unlike silicon that needs a thick active layer due to its low photo-absorption coefficient, MoS₂ is atomically thin²³ and has a high photo-absorption coefficient²⁵, both of which are favorable for fabrication of a much thinner photo-absorbing layer.

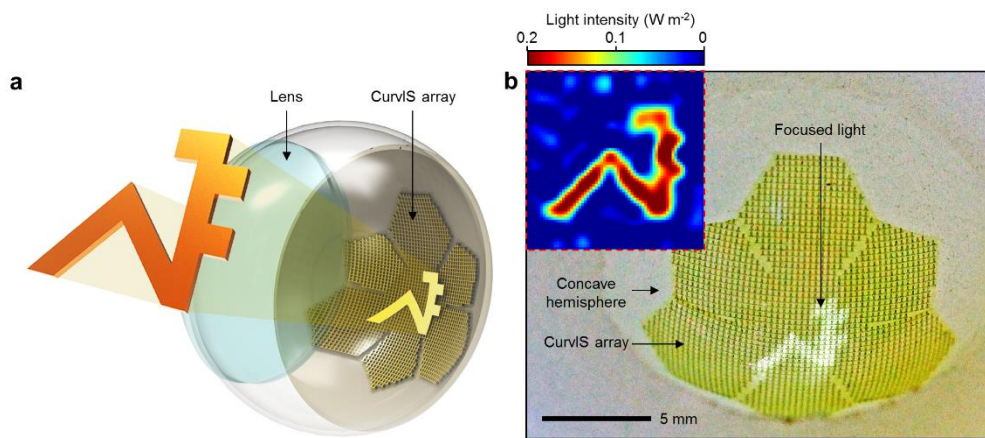


Figure 2.3. High-density curved image sensor array based on the MoS₂-graphene heterostructure. (a) Schematic illustration of the high-density CurvIS array based on the MoS₂-graphene heterostructure. (b) Optical camera image of the high-density CurvIS array. Inset shows the image (*i.e.*, university logo) captured by the CurvIS array.

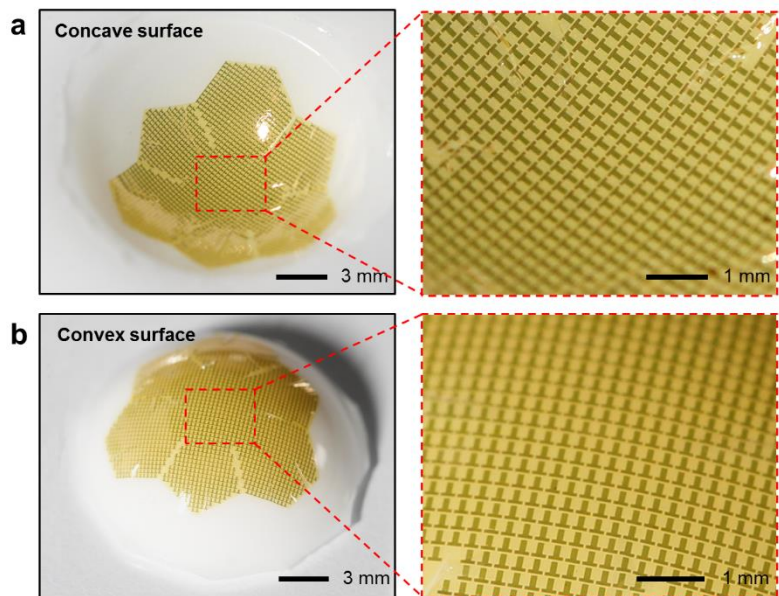


Figure 2.4. The curved image sensor array on the concave and convex hemisphere. (a) Optical camera image of the CurVIS array on a concave surface (left) and its magnified view (right). **(b)** Optical camera image of the CurVIS array on a convex surface (left) and its magnified view (right).

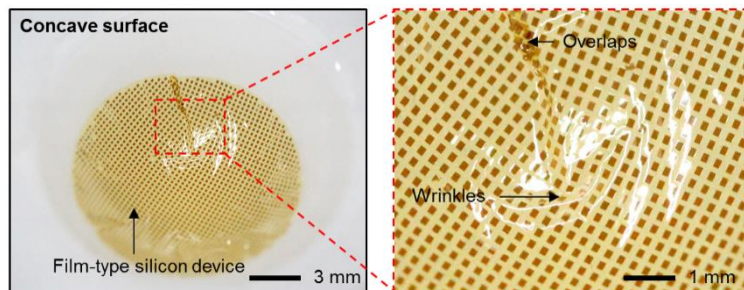


Figure 2.5. Circular film-type device array on the concave hemisphere. Optical camera image of the conventional film-type silicon ($1.25\ \mu\text{m}$) photodiode array on a concave surface (left) and its magnified view (right).

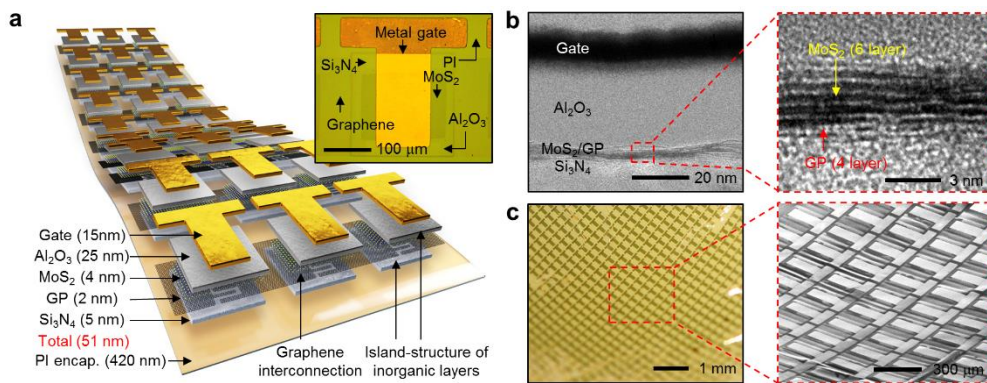


Figure 2.6. Device design and materials in the curved image sensor array. (a) Schematic illustration of the device design. Inset shows an optical microscope image of a single phototransistor. (b) Cross-sectional transmission electron microscope image of the MoS₂-graphene phototransistor (left) and the magnified image of the MoS₂-graphene heterostructure (right). (c) Optical (left) and magnified scanning electron microscope (right) image of the high-density CurvIS array on the concave hemisphere.

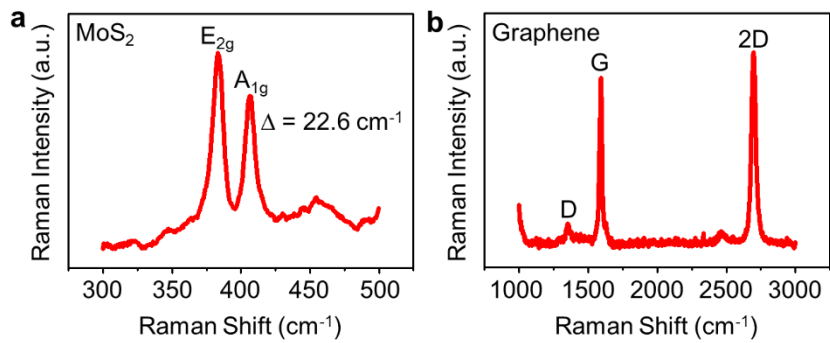


Figure 2.7. Characterization of synthesized MoS₂ and graphene film. (a) Raman spectrum of MoS₂ film. **(b)** Raman spectrum of graphene film.

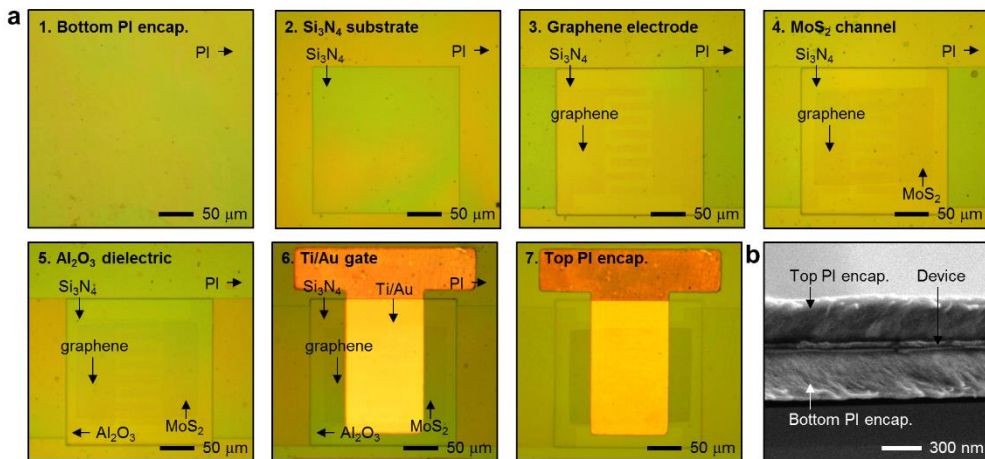


Figure 2.8. Fabrication of the phototransistor array based on the MoS₂-graphene heterostructure. (a) Optical microscope images for showing the fabrication process of a single phototransistor. **(b)** Scanning electron microscope image of the vertical structure of the device and the top and bottom PI encapsulations.

2.3.2 Curved image sensor array based on the MoS₂-graphene heterostructure

A phototransistor array based on the MoS₂-graphene heterostructure with the PI encapsulation is fabricated on a flat substrate (Figure 2.9a). This array is transferred to a hemispherical surface for fabricating the CurvIS array (Figure 2.10). Detailed fabrication steps are described in Methods. The exploded schematic of a single phototransistor is shown in the Figure 2.9a inset.

The transfer curve (I_d - V_g) shows a typical light-sensitive field effect transistor behavior (Figure 2.9b). Under illumination (515 nm), the MoS₂ channel generates a photocurrent whose normalized magnitude (I_d/I_{dark}) is proportional to the illuminated light intensity (Figure 2.9c). The photoresponsivity of the MoS₂-graphene phototransistor is compared with the theoretical photoresponsivity of a silicon photodiode whose silicon thickness is same as MoS₂ (Figure 2.9d; details of the photoresponsivity comparison in Experimental Section). It is found that the former is 2-3 orders higher than the latter, which is due to the efficient photo-absorption of MoS₂²⁵. Conventional silicon image sensors absorb IR light (850 nm) (Figure 2.10e inset), which causes IR noises. On the contrary, the MoS₂ photodetector does not absorb the IR spectrum because of its wide bandgap (Figure 2.10e). Therefore, an IR filter is unnecessary in the MoS₂ device, which helps reduce the thickness and increase the softness of the CurvIS array. As shown in Figure 2.11, the calibrated MoS₂-graphene phototransistor array presents the spatially uniform signal distributions under two different light intensities (2.2 W m⁻² and 3.7 W m⁻²).

The CurvIS array captures various images successfully (Figure 2.3b inset and 2.12). The CurvIS array visualizes the alphabet sigma (Σ) (Figure 2.12a) using a single plano-convex lens (Figure 2.1b) installed in a customized setup (Figure 2.13). Detailed optical imaging procedures are included in Experimental Section. The captured image is not affected by the IR radiation (Figure 2.12b) due to IR blindness of the MoS₂-based phototransistor (Figure 2.10e), whereas a conventional silicon photodetector array without an IR filter shows reddish IR noises (Figure 2.12 inset right). Other imaging results (*e.g.*, cross and heart) are shown in Figure 2.12c and 2.12d.

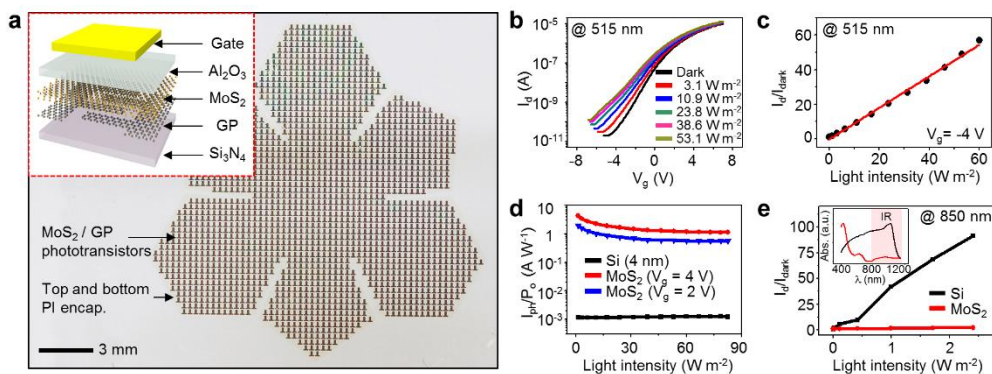


Figure 2.9. Device characterization and imaging using the curved image sensor array. (a) The optical camera image of the phototransistor array with a truncated icosahedron design on a planar substrate. Inset shows a schematic illustration of the device structure. (b) Transfer curves of the phototransistor under different light (515 nm) intensities. (c) Normalized photocurrent change under different light intensities. (d) Photoresponsivity of the MoS₂-graphene phototransistor compared to the silicon photodetector with the same thickness. (e) Normalized photocurrent change under IR illumination (850 nm) of different light intensities. Inset shows the light absorbance of MoS₂ and silicon.

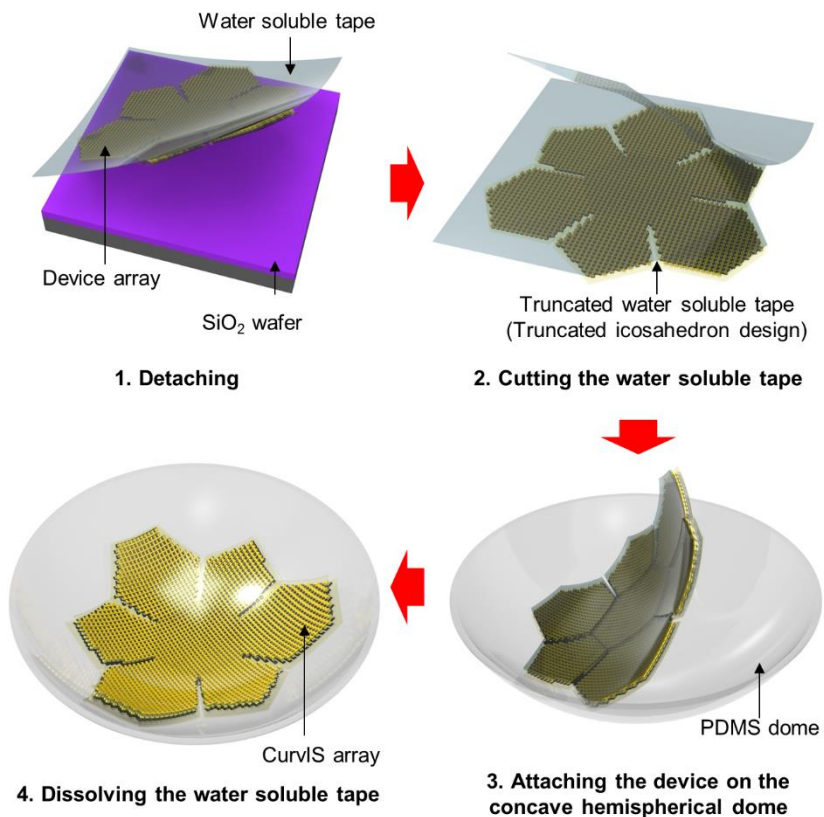


Figure 2.10. Integration of the curved image sensor array on the hemispherical surface. Method for transferring the MoS₂-graphene-based phototransistor array to the concave hemispherical dome.

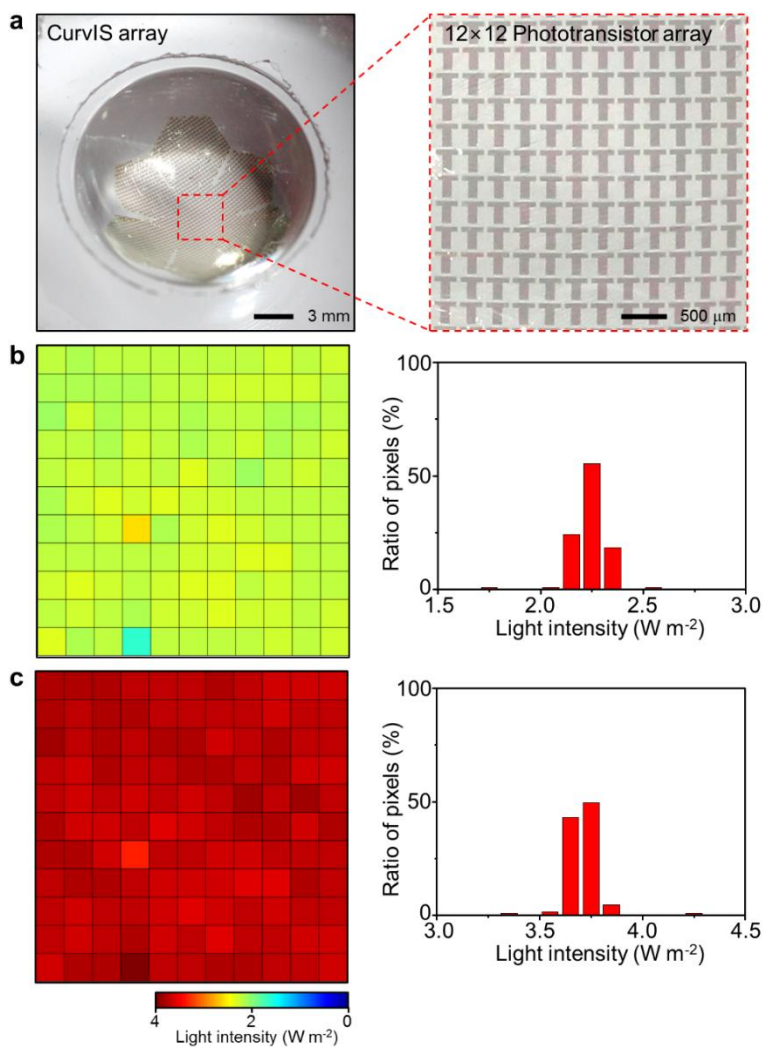


Figure 2.11. Characterization of the phototransistor array. (a) Optical camera image of the CurvIS array on the transparent concave hemispherical dome (left) and its magnified image showing the 12×12 phototransistor array (right). (b,c) Spatial distribution of measured light intensities using the calibrated phototransistor array (left) and its statistical analysis (right) under illumination of different light intensities (2.2 W m⁻² and 3.7 W m⁻² at 515 nm; for b and c, respectively).

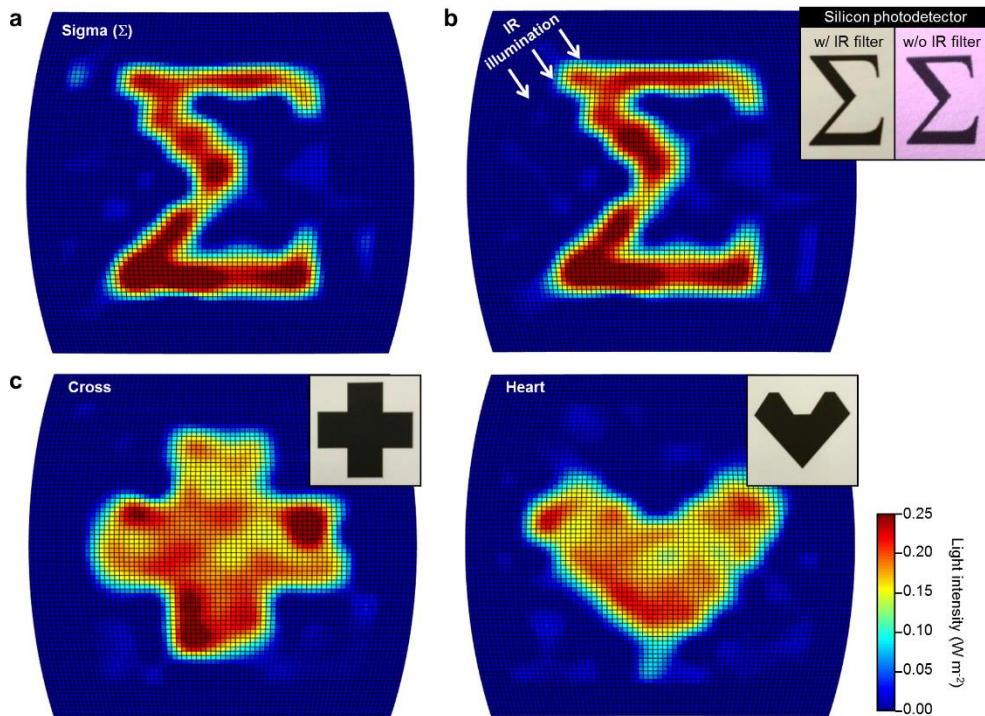


Figure 2.12. Imaging results using the curved image sensor array. (a) Sigma-shaped image captured by the CurvIS array. (b) The same image with Figure 2.12a but captured under IR illumination. Inset images are acquired by a commercial silicon photodetector array with (left) and without (right) an IR filter under IR illumination. (c) Cross- and heart- shaped images obtained by the CurvIS array. Insets show original patterns.

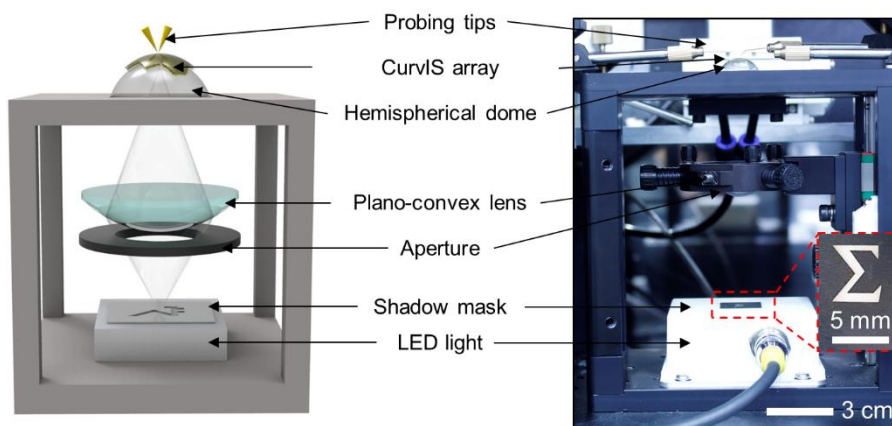


Figure 2.13. Experimental setup for imaging. Schematic illustration (left) and optical camera image (right) of the experimental setup. The setup consists of a white LED blocked with a metal shadow mask, an aperture, a plano-convex lens, the CurvIS array, and probing tips connected to a parameter analyzer.

2.3.3 Human-eye-inspired soft implantable optoelectronics

The ultrathin CurvIS array whose shape and mechanical softness are similar to those of the human retina has high potential to be used as a soft photodetecting component in the retinal prosthesis. Hence the developed ultrathin CurvIS array is applied to the human-eye-inspired soft implantable optoelectronic device. The human eye consists of a lens that collects light, a retina that converts lights into action potentials, and optic nerves that transmit action potentials to the brain (Figure 2.14a). Since the photoreceptors are distributed over the hemispherical retina, the human eye can recognize exact shapes of objects with a single-lens. Patients with retinal degeneration, however, lose vision because the incoming light cannot activate optic nerves due to degenerated photoreceptors³³. The retinal prosthesis restores the vision by acquiring optical information through image sensors, converting the measured optical information into electric signals, and stimulating optic nerves using an electrode array.

Conventional retinal prostheses consist of an external camera module (*e.g.*, camera on eyeglasses) connected to an intraocular micro-electrode array (Figure 2.15a)³⁴. This bulky wearable camera module is uncomfortable, causes unnatural appearances, and leads to image fading due to absence of efference copy from the eye movement³⁵. Recently, retinal prostheses using intraocular image sensors have been reported as alternatives (Figure 2.15b), but these still suffer from various issues; absence of a multi-lens system for focusing images³⁵ and unwanted immune

responses caused by non-conformal integration and/or mechanical mismatch¹⁵ between soft retina and rigid devices.

As shown in Figure 2.14b, we propose a soft implantable optoelectronic device by mimicking the structural features of the human eye. The ultrathin soft optoelectronic device consisting of the CurvIS array and UNE is conformally laminated on the hemispherical retina. This configuration enables the compact optic system, broadens the viewing angle, and captures lights over a large area, just like a human retina (Figure 2.15c). It is especially important to integrate the optoelectronic device onto the hemispherical retina without retinal deformation. The mechanical mismatch between the implanted device and retina may apply continuous pressures to the eye and cause neural degradation particularly in long-term implantation^{1,2,8}. This potentially leads to further degeneration of photoreceptors¹⁴ and immune responses¹.

An artificial retina and sclera model (*i.e.*, a double-layered elastomeric hemispherical shell having similar modulus with human eye) is prepared to reveal mechanical deformation of the eye by the device implantation (Figure 2.16). As shown in Figure 2.14c, the soft optoelectronic device conforms to the artificial eye model (i; original model) with minimal deformation (ii; 1.4 μm -thick soft optoelectronic device), while lamination of a flexible film (iii; 15 μm -thick flexible film) and wafer-based electronics (iv; 525 μm -thick silicon device) induce significant distortion. Smaller interfacial traction is a critical factor because the traction deforms the soft eye model. The soft optoelectronic device causes stress to the artificial eye

model in the orders-of-magnitude lower level than others (0.61 MPa; Figure 2.14d), hence inducing minimal deformation to the eye model (ii; Figure 2.14c). The interfacial traction between the flexible film and the eye model is estimated to be 183 MPa, which would induce visible distortion in the eye model (iii; Figure 2.14c). When attaching the wafer-based electronics to the eye model, the upper limit of the required traction is 2.27 GPa, which induces significant deformation of the eye model (iv; Figure 2.14c).

Minimal mechanical disturbance by the soft optoelectronic device is also analysed by comparing the histology results of the device-implanted retina (experiment group) and the normal retina (control group). The soft optoelectronic device implanted in the retina both for the short (1 week) and long (9 weeks) period shows good biocompatibility in comparison with the control group (normal retina; Figure 2.14e and Figure 2.17). The expression of the fibroblast growth factor 2 (FGF2)³⁶ and the glial fibrillary acidic protein (GFAP)³⁶ in the retina implanted with the soft optoelectronic device show similar tendency with those in the normal retina (Figure 2.17), which indicates the long-term mechanical and material biocompatibility.

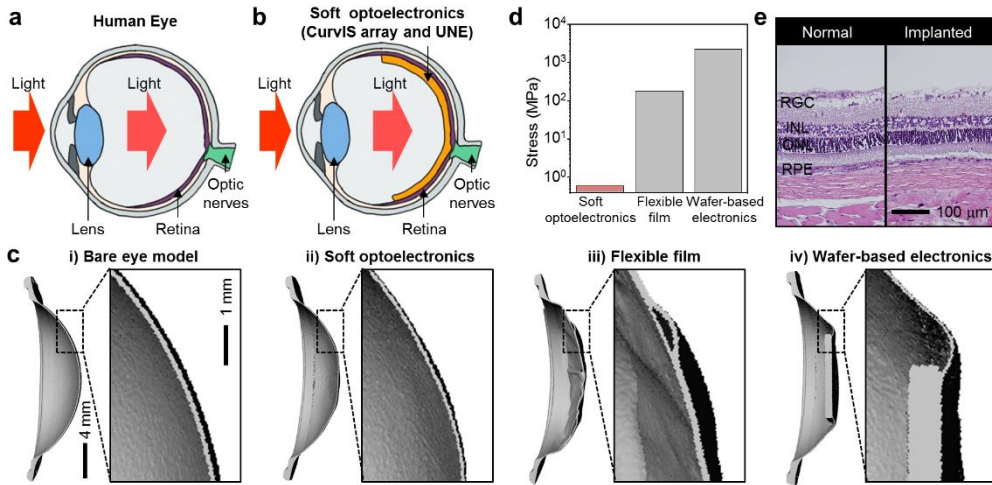


Figure 2.14. Human-eye-inspired soft optoelectronic device. (a) Schematic illustration showing the ocular structure of human. (b) Schematic illustration showing the ocular structure with the soft optoelectronic device. (c) Micro CT image (left) and magnified image (right) showing deformation of (i) the bare eye model, attached by (ii) the soft optoelectronic device, (iii) a flexible film device, and (iv) wafer-based electronics. (d) Induced Stress by three different implanted devices. (e) The H&E stain histology of the normal retina and the retina implanted with the soft optoelectronic device.

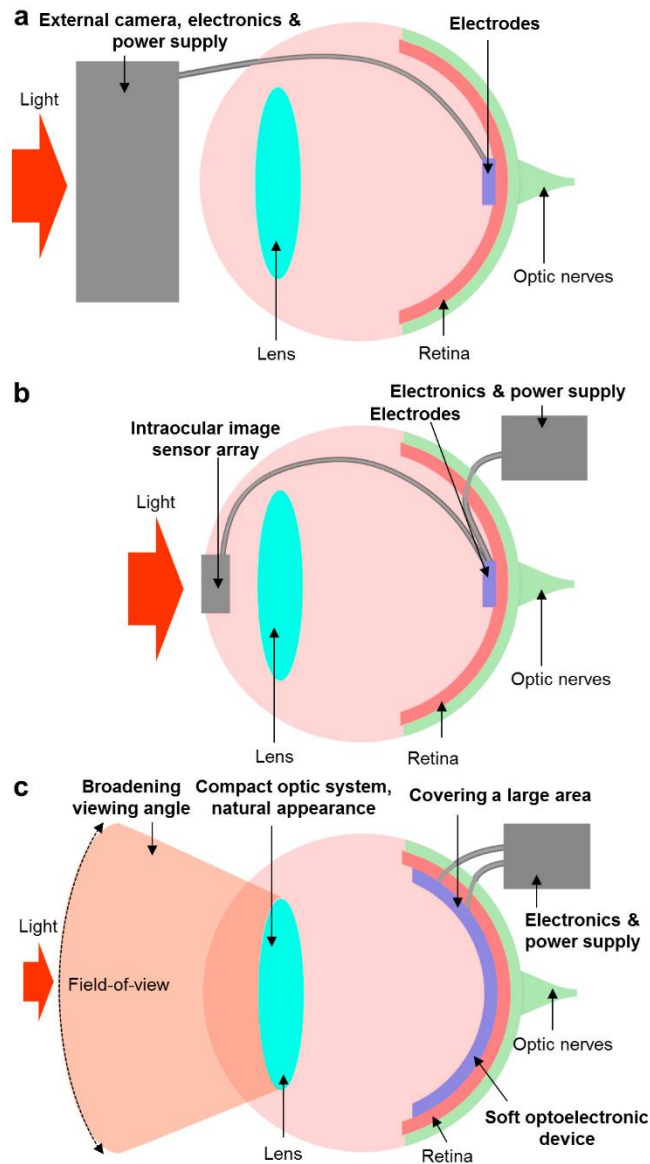


Figure 2.15. Schematic ocular structure implanted with retinal prostheses and the soft optoelectronic device. (a-c) Schematic drawing showing the ocular structure implanted with conventional retinal prostheses (*e.g.*, wearable head-mounted camera (a) and intraocular image sensor array (b)) and the soft optoelectronic device (c).

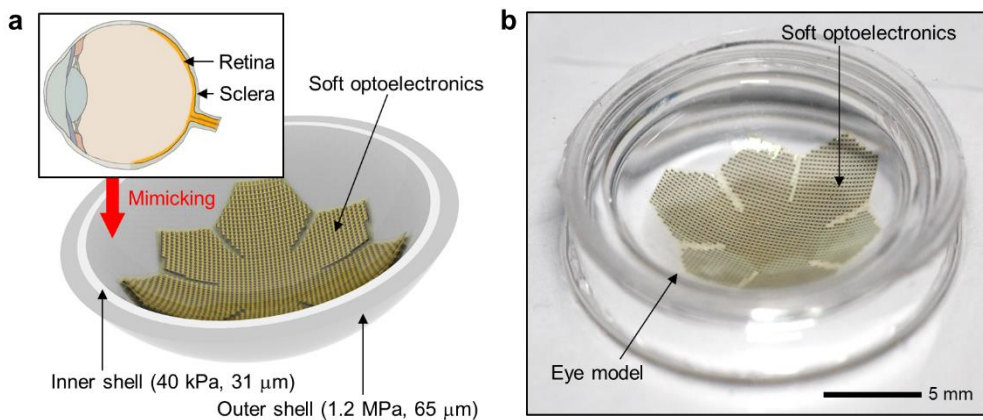
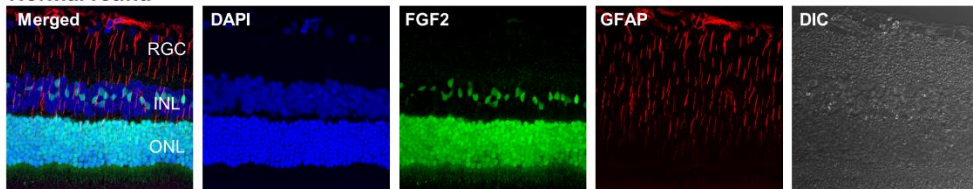


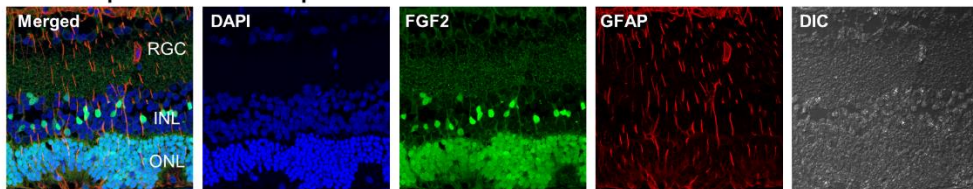
Figure 2.16. Eye model for analyzing the retinal deformation. (a) Schematic illustration of the double-layered eye model that mimics retina (20 kPa)^{S4} and sclera (1.84 MPa)^{S5} in human eye. (b) Optical camera image of the eye model attached with the soft optoelectronic device.

a [Short-term Biocompatibility : 1 week]

Normal retina

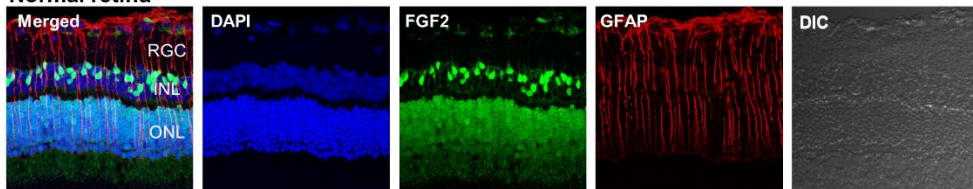


Retina implanted with soft optoelectronics



b [Long-term Biocompatibility : 9 weeks]

Normal retina



Retina implanted with soft optoelectronics

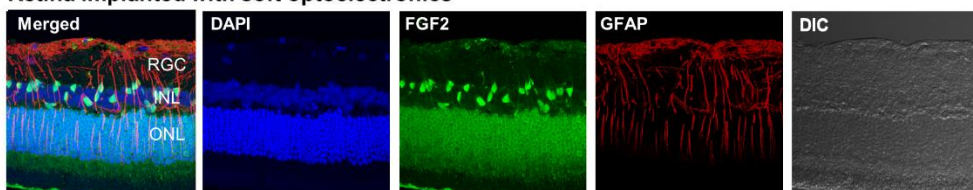


Figure 2.17. Biocompatibility of the soft optoelectronic device. (a,b) The histological staining data (DAPI, FGF2, and GFAP) and differential interference contrast (DIC) microscope image of the normal retina and the retina implanted with the soft optoelectronic device for the short-term (a) and long-term (b) period.

2.3.4 Flexible electronic system integrating the curved image sensor array and ultrathin neural-interfacing electrodes

One of the important issues in the retinal implant is how to convert the visual information obtained by the image sensor array to the corresponding electrical signals to be conveyed to the retina via the micro-electrode array³⁹. In commercial retinal implants³⁸ (*e.g.*, Argus II, Second Sight), the visual information is recognized by a wearable camera module and translated to the electric signals by a video processor to be transmitted to the intraocular micro-electrode array. The electronic devices that supply power and control the system are usually implanted in the extraocular position due to the spatial limitation, but these rigid and bulky devices may cause immune responses and mechanical damages to the surrounding tissues. A photovoltaic type retinal prosthesis without external power sources has been recently reported^{14,39}, but head-mounted glasses are still needed to transfer the IR beam to Si photovoltaic devices. Therefore, the soft CurvIS array and UNE integrated with the flexible implantable electronics⁴⁰ coated with the soft silicone rubber can be a promising candidate of the soft retinal implant due to minimal mechanical mismatch¹⁵ between the tissue and the implanted device.

Figure 2.18a and 2.18b show a schematic and a corresponding optical camera image of the integrated soft electronic system. The photocurrent is generated by each phototransistor of the soft CurvIS array in response to external light, and is amplified by a transimpedance amplifier and an inverter. The micro-controller unit (MCU) measures the amplified signal, processes it, and produces programmed

electrical pulses. The pulse electrically stimulates the retina via the electrode stacked with the corresponding phototransistor. The ultrathin soft optoelectronic device array is conformally laminated on the eye model (Figure 2.18c). As shown in Figure 2.18d, each phototransistor of the CurvIS array and a corresponding electrode in the UNE are vertically stacked in the ultrathin and soft platform. To develop a soft form of the fully implantable system, we introduce the flexible printed circuit board with the soft surface coating (soft FPCB; Figure 2.18e). The soft FPCB includes all electronics for image processing as depicted in Figure 2.18a, analyzes the photocurrent produced from the phototransistor, and transfers the programmed electrical pulses to the stimulation electrode integrated in the same pixel (Figure 2.18d).

Mechanical flexibility and softness of the soft FPCB is confirmed by experimental analyses. The conventional rigid electronics has the modulus in the range of GPa and shows significant mechanical mismatch to the soft human tissues. The surface of the FPCB is coated with thick silicone rubber whose modulus (~ 50 kPa) is similar to that of human tissues (100 - 1500 kPa)¹. This mechanically-matched material property allows soft and conformal interfaces with surrounding tissues. Figure 2.18f shows the soft FPCB poked by the tip of a pipet tube. Thick coating of the FPCB with silicone rubber provides the cushion-like surface. The silicone rubber coating also effectively protects the electronic chips from external impact and water exposure. Unlike conventional rigid electronics, the soft FPCB also can be easily deformed (Figure 2.18g).

The integrated form of the soft optoelectronic system can successfully recognize the illuminated light and generate programmed electrical pulses. The soft integrated system with the FPCB measures the photocurrent generated at each phototransistor, and delivers electrical stimulation to the eye model using the integrated electrode. When light is illuminated to the pixel 'a' and pixel 'b' as shown in Figure 2.18c, electrical pulses are selectively generated at the electrode of the pixel 'a' and pixel 'b', respectively (Figure 2.18h white region). Figure 2.18i shows the magnified electrical signals in Figure 2.18h. When light is simultaneously illuminated to the pixel 'a' and pixel 'c', the soft FPCB processes the measured signals from image sensors and successfully generates electrical pulses on both electrodes of pixel 'a' and pixel 'c' (Figure 2.18h blue region).

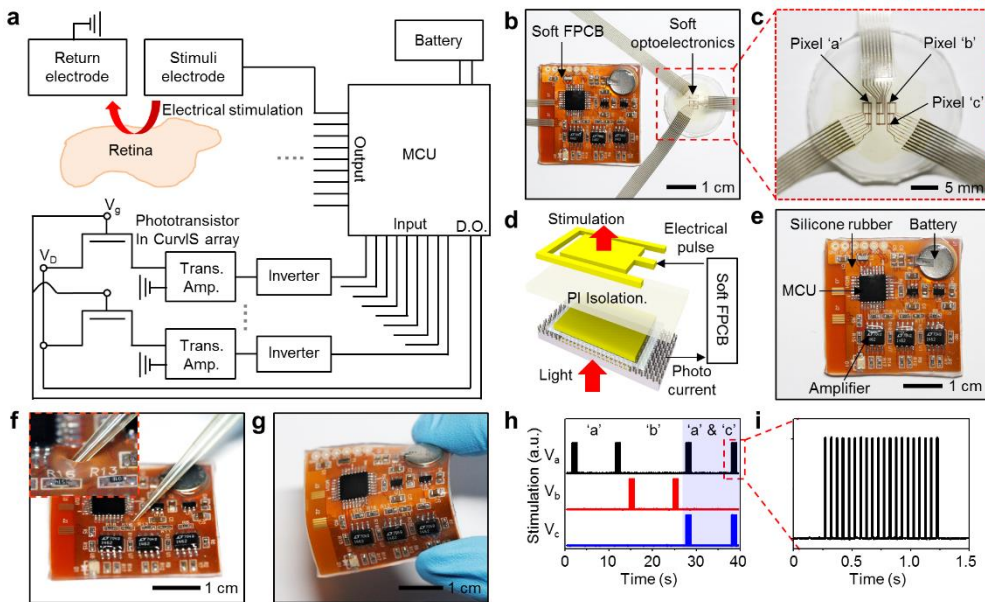


Figure 2.18. Soft flexible printed circuit board that integrates the CurvIS array with UNE. (a) Schematic drawing of the electronics for detecting the external light (bottom) and for applying the stimulation (top). (b) Optical camera image of the CurvIS array and the UNE on the eye model, which are connected by the soft FPCB. (c) Magnified optical camera image of the vertically stacked the CurvIS array and the UNE. (d) Schematic illustration of the phototransistor (bottom) and the stimulation electrode (top) stacked together and connected via the soft FPCB. (e) Optical camera image of the soft FPCB. (f,g) Optical camera image of the soft FPCB under poking (f) and bending (g). (h,i) Generated electrical pulses at three different pixels by responding the light on/off (h), and magnified electrical pulse (i).

2.3.5 Retinal stimulation by the soft optoelectronic device

Figure 2.19a shows a schematic that describes the *in vivo* animal experiment using the soft optoelectronic device and a neural recording system. The extraocular imager is used to detect the incoming light signals without causing interferences with healthy photoreceptors. The electrode attached on the retina successfully stimulates the optic nerves. The excitation of optic nerves is monitored by penetrative electrodes at the visual cortex (Figure 2.19a). The stimulation of the retina^{4,14} is confirmed by the elicited spikes⁴¹ and changes in local field potential (LFP)³, which are simultaneously measured at the rat's primary visual cortex^{12,41}. Detailed animal preparation and experiment conditions are described in Experimental section. When pulsed optical signals are applied to the rat's eye, the rat's retina senses the light being on/off. This optical information is transferred to the visual cortex via optic nerves, resulting in elicited spikes (Figure 2.19b) and LFP changes in the frequency range of 4-15 Hz (Figure 2.19c). Similarly, the MoS₂-graphene-based soft optoelectronic device detects the light being on/off, and the corresponding electrical pulses are applied to the optic nerve through the UNE. Consequently, the visual cortex is similarly activated, leading to elicited spikes (Figure 2.19d) and LFP changes in the same frequency range (Figure 2.19e).

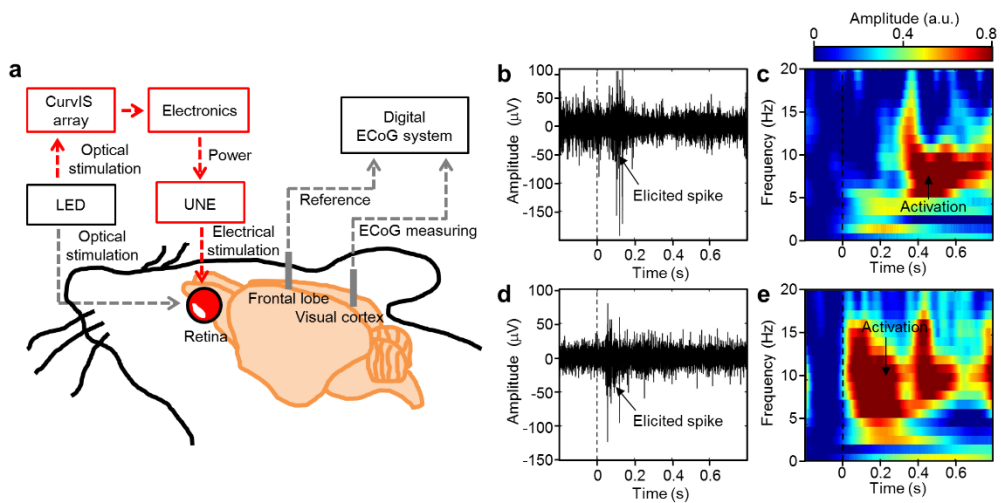


Figure 2.19. Retinal stimulation by the soft optoelectronic device. (a) Schematic drawing of the experimental setup for stimulating the retina (left) and for recording neural signals from the visual cortex (right). **(b,c)** Measurement of elicited spikes **(b)** and LFP changes **(c)** in the visual cortex by optical stimulation. **(d,e)** Measurement of elicited spikes **(d)** and LFP changes **(e)** in the visual cortex by electrical stimulation.

2.4 Conclusion

In summary, the high-density MoS₂-graphene CurvIS array is developed by using ultrathin soft materials and strain-isolating/-releasing device designs. Mechanical and optical analyses corroborate the validity of proposed materials and device designs for the CurvIS array. The CurvIS array with the single-lens optics effectively obtains pixelated images without IR noises. The CurvIS array and UNE are integrated through the soft FPCB to form a human-eye-inspired soft implantable optoelectronic device, which causes minimal mechanical deformation to the eye model as validated by both experiments and corresponding FEA simulations. The soft optoelectronic device successfully stimulates the optic nerves of a rat model in response to the pulsed external light, which is confirmed by recording spikes and LFP changes at the visual cortex of the rat. The proposed human-eye-inspired soft optoelectronic device is a step forward to the next generation soft bioelectronics and the soft imaging element of the retinal prosthesis.

2.5 Reference

* The contents of this chapter were published in *Nature Communications* (2017, **8**, 1664)

1. Mineev, I. R. *et al.* Electronic dura mater for long-term multimodal neural interfaces. *Science* **347**, 159–163 (2015).
2. Chortos, A., Liu, J. & Bao, Z. Pursuing prosthetic electronic skin. *Nat. Mater.* **15**, 937–950 (2016).
3. Khodagholy, D. *et al.* *In vivo* recordings of brain activity using organic transistors. *Nat. Commun.* **4**, 1575 (2013).
4. Maya-Vetencourt, J. F. *et al.* A fully organic retinal prosthesis restores vision in a rat model of degenerative blindness. *Nat. Mater.* DOI:10.1038/nmat4874 (2017).
5. Keplinger, C. *et al.* Stretchable, transparent, ionic conductors. *Science* **341**, 984–987 (2013).
6. Yuk, H. *et al.* Skin-inspired hydrogel-elastomer hybrids with robust interfaces and functional microstructures. *Nat. Commun.* **7**, 12028 (2016).
7. Kaltenbrunner, M. *et al.* An ultra-lightweight design for imperceptible plastic electronics. *Nature* **499**, 458–463 (2013).
8. Son, D. *et al.* Multifunctional wearable devices for diagnosis and therapy of movement disorders. *Nat. Nanotech.* **9**, 397–404 (2014).
9. Sekitani, T. *et al.* Ultraflexible organic amplifier with biocompatible gel

- electrodes. *Nat. Commun.* **7**, 11425 (2016).
10. Liu, J. *et al.* Syringe-injectable electronics. *Nat. Nanotech.* **10**, 629–636 (2015).
 11. Tee, B. C.-K. *et al.* A skin-inspired organic digital mechanoreceptor. *Science* **350**, 313–316 (2015).
 12. Kim, J. *et al.* Stretchable silicon nanoribbon electronics for skin prosthesis. *Nat. Commun.* **5**, 5747 (2014).
 13. Jones, I. L., Warner, M. & Stevens, J. D. Mathematical modelling of the elastic properties of retina: a determination of Young's modulus. *Eye* **6**, 556–559 (1992).
 14. Mandel, Y. *et al.* Cortical responses elicited by photovoltaic subretinal prostheses exhibit similarities to visually evoked potentials. *Nat. Commun.* **4**, 1980 (2013).
 15. Fu, T.-M. *et al.* Stable long-term chronic brain mapping at the single-neuron level. *Nat. Methods* **13**, 875–882 (2016).
 16. Kang, P., Wang, M. C., Knapp, P. M. & Nam, S. Crumpled graphene photodetector with enhanced, strain-tunable, and wavelength-selective photoresponsivity. *Adv. Mater.* **28**, 4639–4645 (2016).
 17. Choi, W. *et al.* High-detectivity multilayer MoS₂ phototransistors with spectral response from ultraviolet to infrared. *Adv. Mater.* **24**, 5832–5836 (2012).
 18. Ko, H. C. *et al.* A hemispherical electronic eye camera based on compressible silicon optoelectronics. *Nature* **454**, 748–753 (2008).
 19. Song, Y. M. *et al.* Digital cameras with designs inspired by the arthropod eye. *Nature* **497**, 95–99 (2013).
 20. Floreano, D. *et al.* Miniature curved artificial compound eyes. *Proc. Natl. Acad.*

- Sci. USA* **110**, 9267–9272 (2013).
21. Seo, J.-H. *et al.* Flexible phototransistors based on single-crystalline silicon nanomembranes. *Adv. Opt. Mater.* **4**, 120–125 (2015).
 22. Amani, M. *et al.* Near-unity photoluminescence quantum yield in MoS₂. *Science* **350**, 1065–1068 (2015).
 23. Akinwande, D., Petrone, N. & Hone, J. Two-dimensional flexible nanoelectronics. *Nat. Commun.* **5**, 5678 (2014).
 24. Lee, G.-H. *et al.* Flexible and transparent MoS₂ field-effect transistors on hexagonal boron nitride-graphene heterostructures. *ACS Nano* **7**, 7931–7936 (2013).
 25. Ling, Z. P. *et al.* Large-scale two-dimensional MoS₂ photodetectors by magnetron sputtering. *Opt. Express* **23**, 13580–13586 (2015).
 26. Zhang, W. *et al.* High-gain phototransistors based on a CVD MoS₂ monolayer. *Adv. Mater.* **25**, 3456–3461 (2013).
 27. Chang, H.-Y. *et al.* High-performance, highly bendable MoS₂ transistors with high-k dielectrics for flexible low-power systems. *ACS Nano* **7**, 5446–5452 (2013).
 28. Yin, Z. *et al.* Single-layer MoS₂ phototransistors. *ACS Nano* **6**, 74–80 (2012).
 29. Lopez-Sanchez, O. *et al.* Ultrasensitive photodetectors based on monolayer MoS₂. *Nat. Nanotech.* **8**, 497–501 (2013).
 30. Lee, H. *et al.* A graphene-based electrochemical device with thermoresponsive microneedles for diabetes monitoring and therapy. *Nat. Nanotech.* **11**, 566–572

- (2016).
31. Cheng, H. *et al.* An analytical model of strain isolation for stretchable and flexible electronics. *Appl. Phys. Lett.* **98**, 061902 (2011).
 32. Park, S.-I. *et al.* Theoretical and experimental studies of bending of inorganic electronic materials on plastic substrates. *Adv. Funct. Mater.* **18**, 2673–2684 (2008).
 33. Duncan, J. L. *et al.* High-resolution imaging with adaptive optics in patients with inherited retinal degeneration. *Invest. Ophthalmol. Vis. Sci.* **48**, 3283–3291 (2007).
 34. Dowling, J. Current and future prospects for optoelectronic retinal prostheses. *Eye* **23**, 1999–2005 (2009).
 35. Stingl, K. *et al.* Subretinal visual implant alpha IMS-clinical trial interim report. *Vision Res.* **111**, 149–160 (2015).
 36. Antognazza, M. R. *et al.* Characterization of a polymer-based, fully organic prosthesis for implantation into the subretinal space of the rat. *Adv. Health. Mater.* **5**, 2271–2282 (2016).
 37. Zrenner, E. Fighting blindness with microelectronics. *Sci. Transl. Med.* **5**, 210ps16 (2013).
 38. Humayun, M. S. *et al.* Interim results from the international trial of second sight's visual prosthesis. *Ophthalmology* **119**, 779-788 (2012).
 39. Mathieson, K. *et al.* Photovoltaic retinal prosthesis with high pixel density. *Nat. Photon.* **6**, 391-397 (2012).

40. Wei, G. *et al.* Fully integrated wearable sensor arrays for multiplexed *in situ* perspiration analysis. *Nature* **529**, 509-514 (2016).
41. Canales, A. *et al.* Multifunctional fibers for simultaneous optical, electrical and chemical interrogation of neural circuits *in vivo*. *Nat. Biotech.* **33**, 277–284 (2015).

Chapter 3. Aquatic-vision-inspired imaging system using a single monocentric lens and a silicon nanorod photodiode array

3.1 Introduction

Advanced mobile electronics has promoted the development of a wide field-of-view (FoV), miniaturized, and light-weight imaging system, particularly for applications in security monitoring, obstacle avoidance, and object tracking^{1,2}. However, due to the large Petzval field curvature of panoramic scenes, a large number of lenses are required to focus the panoramic scenes onto a flat rigid image sensor array^{3,4}, which increases the overall volume and weight of the camera module⁵. For example, the conventional wide angle lenses whose FoV is over 120° require even more lenses, typically 8-13 lenses (Figure 3.1)⁶. Therefore, such a wide FoV imaging system necessarily involves with the eight-fold increased module size to standard one as well as heavy-weight and complicated system construction (Table 3.1).

The eyes of living organisms, biological imaging systems optimized through evolution, have inspired development of novel biomimicry cameras that do not require the complicated multi-lens optics⁷⁻⁹. For example, the curved image sensor arrays inspired by the human eye have enabled the aberration-free imaging using single-lens optics (Fig. 3.2a)¹⁰⁻¹². But such human-eye-inspired cameras inherently

offer the limited FoV around 100° due to serious off-axis aberration^{3,13}. In another example, the compound eye imaging system inspired by the eyes of arthropods has exhibited wide FoV characteristics (Figure 3.2b)¹⁴⁻¹⁷. However, the visual acuity of the compound eyes is far inferior to that of the eyes of vertebrates and aquatic animals⁵ because of the diffraction limit of a corneal lens.

On the other hand, aquatic eyes found in the fish¹⁸, cephalopod¹⁹, and aquatic mammals²⁰, feature a wide FoV ($\sim 160^\circ$) with high visual acuity⁶. The aquatic eye also exhibits i) small form factor⁶, ii) minimal aberration optics¹⁹, iii) deep depth-of-field (DoF)²¹, and iv) facile accommodation²². Furthermore, the retina of the aquatic eye shows the superior light sensitivity, which allows highly sensitive vision even in the dim underwater condition²³. Such advantages in the aquatic vision are due to a single protruding spherical monocentric lens (*mo*-lens) with the parabolic refractive index^{6,18} and a hemispherical focal plane retina with the highly light-sensitive rod cells²⁴. Such unique features found in the aquatic eyes can inspire development of a novel imaging system that can meet the requirements in advanced mobile electronics applications^{25,26}.

Here, we present an aquatic-vision-inspired imaging system featured with a wide FoV, miniaturized design, deep DoF, and enhanced light-sensitivity by integrating a tailored *mo*-lens with a hemispherical silicon nanorod photodiode array (*h-SiNR*-PDA). In detail, the aquatic-vision-inspired system features wide FoV ($\sim 120^\circ$), small form factor (~ 11.5 mm), minimal optical aberrations, deep DoF (10 cm to infinity), and facile accommodation. In addition, the *h-SiNR*-PDA exhibits

enhanced light-sensitivity by employing nanorod-texturing and Al_2O_3 passivation of the silicon photodiode surface, which enables sensitive detection of the collected lights even including low intensity ones. We analyzed the developed aquatic-vision-inspired system theoretically and experimentally to validate that such all features could be realized in one single integrated system. The developed system could successfully capture the projected images from wide angular directions.

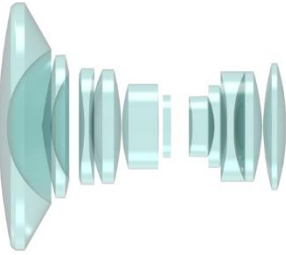
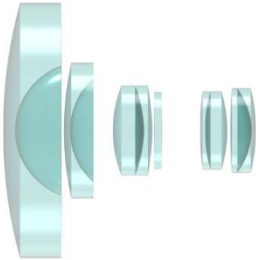
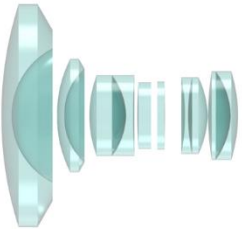
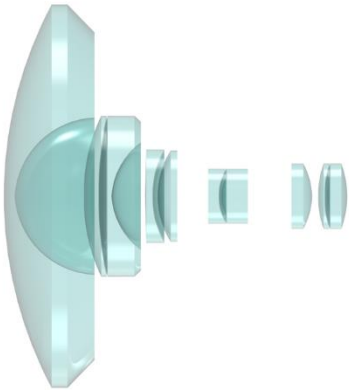
Schematic of conventional wide angle multi-lens	Parameters
	<p>The number of lenses: 11 Length : 101.6 mm Maximum diameter: 58.2 mm Volume : 2703 cm³</p>
	<p>The number of lenses: 9 Length : 95.5 mm Maximum diameter: 59.5 mm Volume : 2827 cm³</p>
	<p>The number of lenses: 10 Length : 85.7 mm Maximum diameter: 50.4 mm Volume : 1710 cm³</p>
	<p>The number of lenses: 10 Length : 125 mm Maximum diameter: 90 mm Volume : 7308 cm³</p>

Figure 3.1. Conventional wide angle multi-lens. Schematic illustration and detailed parameters of conventional wide angle multi-lenses.

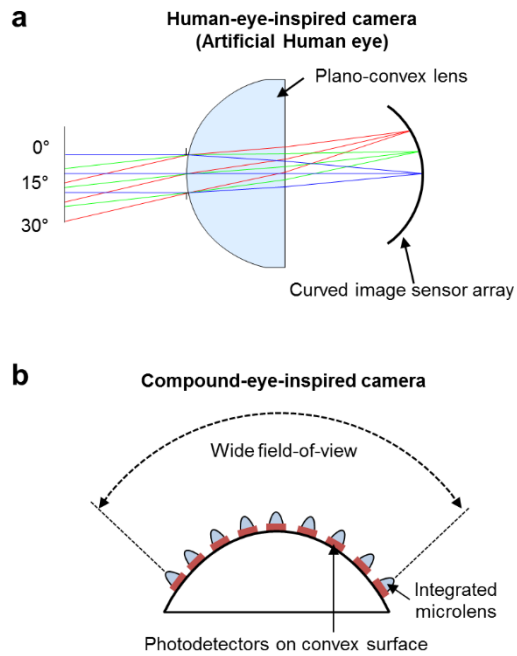


Figure 3.2. Conventional bio-inspired imaging system. (a) Human-eye-inspired imaging system based on a plano-convex lens and a curved image sensor array. **(b)** Arthropod-inspired compound eye using a hemispherically curved image sensor array in which each photodetector is integrated with a microlens.

	Conventional wide FoV camera	Aquatic-vision-inspired camera
Number of lens	11	1
Form factor	93.7 mm	11.5 mm
Field-of-view	> 160°	> 120°
Optical aberration	Low	Low
Focusing method	Difficult	Easy

Table 3.1. Comparison of the aquatic-vision-inspired camera with the conventional wide field-of-view camera. The number of lens, form factor, field-of-view, optical aberration, and focusing method of the conventional wide FoV camera and the fish-eye-inspired imaging system.

3.2 Experimental section

3.2.1 Fabrication of the tailored *mo*-lens and detailed specifications

For fabricating the tailored *mo*-lens, two kinds of lenses (BK7 and SF16) were used. Refractive index at the wavelength of 588 nm and the radius of curvature (RoC) of BK7 are 1.52 and 2 mm, and those of SF16 are 1.65 and 4.1 mm, respectively. Transparent optical adhesive (NOA 61, Norland Products) whose refractive index is 1.56 was used to fill the vacancy between the lenses.

The fabrication of the tailored *mo*-lens began with placing SF16 on the center of a holder. NOA 61 was then dropped on SF16, BK7 was inserted inside SF16, and NOA 61 was cured by ultraviolet irradiation to fix the lenses, which completes the fabrication of half of the *mo*-lens. The other part of the *mo*-lens was fabricated by following the same process. The aperture was assembled with both sides of *mo*-lens after precise alignment, and the vacancy between the half-ball lenses was filled with NOA 61.

3.2.2 Fabrication of the hemispherical silicon nanorod photodiode array

The fabrication of *h-SiNR*-PDA began with spin-coating of the polystyrene (PS) microsphere solution (0.5 μm diameter; Thermo Fisher scientific) on a SOI wafer (1.25 μm -thick top silicon; SOITEC). A series of dry etching processes with oxygen and SF_6 form *SiNR* texturing. The residual PS microsphere monolayer was removed by sonication and piranha solution treatment. After a series of doping processes by using spin-on-dopants, the nanorod-textured silicon nanomembrane was

transfer-printed onto the prepared polyimide (PI) film ($\sim 1 \mu\text{m}$, bottom encapsulation; Sigma Aldrich) spin-coated on a SiO_2 wafer. The active silicon diode region was isolated using photolithography and dry etching. Then, the Al_2O_3 passivation layer ($\sim 25 \text{ nm}$) was deposited through the plasma enhanced atomic layer deposition, and was isolated through photolithography and wet etching using a buffered oxide etchant. An additional PI film ($\sim 1 \mu\text{m}$, 2nd encapsulation) was spin-coated and cured. The VIA region was patterned through photolithography and dry etching, and Cr/Au layers (10/100 nm, 1st metal electrode) was deposited and patterned by thermal evaporation and wet etching. Additional spin-coating and curing of a PI film ($\sim 1 \mu\text{m}$, 3rd encapsulation) and deposition of Cr/Au layers (10/100 nm, 2nd metal electrode) were performed using the same process. A final PI film ($\sim 1 \mu\text{m}$, top encapsulation) was spin-coated and cured, and then the entire PI film was etched into a hexagonal mesh structure by dry etching. The fabricated *h-SiNR*-PDA was detached from the SiO_2 wafer using a water-soluble tape (3 M Corp., USA), and transfer-printed onto a hemispherically curved substrate made of polydimethylsiloxane (PDMS; Dow, Corning, USA).

3.2.3 Optical simulation for the aquatic-vision-inspired imaging system

Monochromatic spot radius and Seidel aberration coefficients of each optical systems were calculated using Radiant ZEMAX LLC. For comparison with the tailored *mo*-lens (Table 3.2), the conventional wide angle multi-lens (Table 3.3) and the homogeneous ball lens (Table 3.4) were prepared as controls.

Table 2 Tailored monocentric lens (F/# = 2.63)				
Surface	Radius (mm)	Thickness (mm)	Material	Semi-diameter (mm)
OBJECT	Infinity	Infinity	-	Infinity
1	4.100	2.100	SF16	4.100
2	2.000	2.000	BK7	2.000
STOP	Infinity	0.500	NOA61	1.000
4	Infinity	2.000	BK7	1.700
5	-2.000	2.100	SF16	2.000
6	-4.100	2.789	-	4.100
IMAGE	-7.500	-	-	7.500

Table 3.2. Information of the monocentric lens in the aquatic-vision-inspired optical system. The radii, thicknesses, materials, and semi-diameters of each lens used in the tailored *mo*-lens.

Table 3 Conventional wide angle multi-lens (F/# = 2.63)				
Surface	Radius (mm)	Thickness (mm)	Material	Semi-diameter (mm)
OBJECT	Infinity	Infinity	-	Infinity
1	-117.300	3.162	N-SK4	18.081
2	16.378	1.168	-	12.724
3	17.551	6.871	SF1	12.645
4	-69.066	2.718	N-SK4	12.472
5	11.336	5.245	-	8.327
6	-23.402	1.765	SF1	8.304
7	-19.359	2.629	N-SK4	8.311
8	-27.730	14.427	-	8.218
STOP	Infinity	3.797	-	4.202
10	-84.131	2.870	N-SK4	5.966
11	-25.071	0.267	-	6.654
12	325.992	4.318	N-SK4	7.078
13	-13.186	1.854	SF1	7.453
14	-53.364	9.627	-	8.242
15	104.798	2.629	SF1	11.229
16	30.725	0.267	-	11.689
17	31.138	5.613	N-SK4	11.899
18	-43.514	0.902	-	12.119
19	27.558	4.026	N-SK4	12.432
20	427.548	20.271	-	12.240
Image	Infinity	-	-	7.648

Table 3.3. Information of each lens component in the conventional wide angle multi-lens. The radii, thicknesses, materials, and semi-diameters of each lens used in the conventional wide angle multi-lens.

Table 4 Homogeneous ball lens (F/# = 2.63)				
Surface	Radius (mm)	Thickness (mm)	Material	Semi-diameter (mm)
OBJECT	Infinity	Infinity	-	Infinity
1	4.900	4.900	BK7	4.900
STOP	Infinity	0.500	NOA61	1.000
4	Infinity	4.900	BK7	1.700
5	-4.900	3.085	-	4.900
IMAGE	-7.500	-	-	7.500

Table 3.4. Information of each lens component in the homogeneous ball lens. The radii, thicknesses, materials, and semi-diameters of each lens used in the homogeneous ball lens.

3.3 Result and discussion

3.3.1 Structural and functional features of the natural aquatic eye

Figure 3.3a shows a photograph of an aquatic animal (*i.e.*, *Labidochromis caeruleus*), and the inset shows a corresponding schematic illustration highlighting the anatomy of its eye. The aquatic vision exhibits the outstanding wide FoV based on only a single-lens^{6,23} to protect itself from predators or to hunt for prey in wide angular directions. It also shows superior light sensitivity compared to that of terrestrial animals due to its highly light-sensitive rod cells, which enables clear vision in the dim underwater environment.

Such optical properties arise from the unique structural design of the aquatic vision. The aquatic vision system consists of a protruding *mo*-lens with parabolic refractive index, a hemispherical retina with highly sensitive elongated rod cells, cornea and iris, and retractor/protractor muscles (Figure 3.3b). The protruding *mo*-lens with spherical symmetry enables wide FoV vision by forming the hemispherical focal plane that is matched with the hemispherical retina. The parabolic gradient refractive index profile of the *mo*-lens (Figure 3.3b) further minimizes chromatic and monochromatic optical aberrations, allowing nearly zero aberrations. Meanwhile, the retina of the aquatic eye contains many rod cells, much more than cone cells, thus suitable to detect the low-intensity light in undersea conditions²³. Furthermore, the elongated outer segment of rod cells enhances their photo-absorption by extending the length of the light pathway. In addition, the cornea protects the inside of the eye, and the iris blocks stray light. The retractor/protractor muscles precisely move the

mo-lens back and forth to adjust the focal length²².

For quantitative understanding of such properties, optical simulation on the aquatic vision is performed. The aquatic vision can focus the light from wide angular directions ($< 160^\circ$) to an extremely tiny focal spot. The three-dimensional ray-tracing simulation based on the Monte-Carlo method validates the inherent superiority of the *mo*-lens in wide FoV focusing compared to a control case, the homogeneous spherical lens. The protruding *mo*-lens forms a small focal spot, whose size is $16.9\ \mu\text{m}$, $23.1\ \mu\text{m}$, and $20.9\ \mu\text{m}$, for the light from 0° , 40° , and 80° (*i.e.*, FoV is 160°), respectively, on the hemispherical retina (Figure 3.3c top). However, the homogeneous spherical lens forms a relatively larger focal spot with the size of $23.4\ \mu\text{m}$, $62.5\ \mu\text{m}$, and $62.7\ \mu\text{m}$ for 0° , 40° , and 80° , respectively, on the hemispherical retina, which indicates its large coma aberration. Ray-tracing simulation further supports the effective correction of off-/on-axis aberrations by the *mo*-lens (Figure 3.2b).

In addition, the aquatic vision shows deep DoF, which enables well-focused imaging for the objects located at a wide range of object distances (d_o ; the distance between the *mo*-lens and object) (Figure 3.3 bottom), due to the inherently short focal length (d_f ; the distance between the *mo*-lens and hemispherical focal plane) ($3.55\ \text{mm} \sim 5.5\ \text{mm}$) (Figure 3.4). With maintaining the d_f of $3.55\ \text{mm}$, all objects far from $10\ \text{cm}$ can be perfectly focused (red dotted box in Figure 3.3d). In the case of the object located at $2\ \text{cm}$, the d_f slightly changes from $3.55\ \text{mm}$ to $5.5\ \text{mm}$. However, by slightly modulating the image distance (d_i ; the distance between the *mo*-lens and hemispherical retina) to be equal to the changed d_f ($5.5\ \text{mm}$) using the

retractor/protractor muscles (Figure 3.5), the blurred images can be re-focused (blue dotted box in Figure 3.3d).

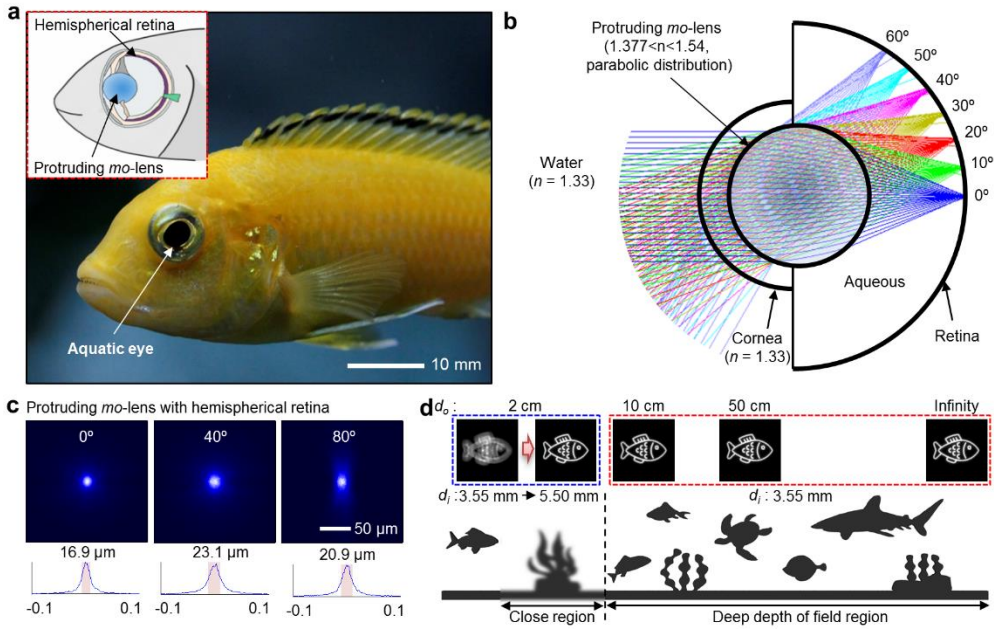


Figure 3.3. Structural and functional features of the aquatic vision in nature. (a) Photograph of *Labidochromis caeruleus*. Inset shows an anatomic illustration of the aquatic eye. **(b)** Ray tracing simulation of the optical system mimicking the aquatic vision. **(c)** Simulation of focused light spots (top) by the protruding *mo*-lens for point-light sources from three incident angles (0° , 40° , and 80°). Line graphs (bottom) show corresponding cross-sectional intensity profiles. **(d)** Simulation results (top) to focus objects located at different d_o (e.g., 2 cm for blue dashed box; 10 cm, 50 cm, and infinity for red dashed box). The object located at $d_o = 2$ cm is re-focused by visual accommodation (d_i change from 3.55 mm to 5.50 mm). The bottom frame shows a schematic drawing that shows the deep DoF feature.

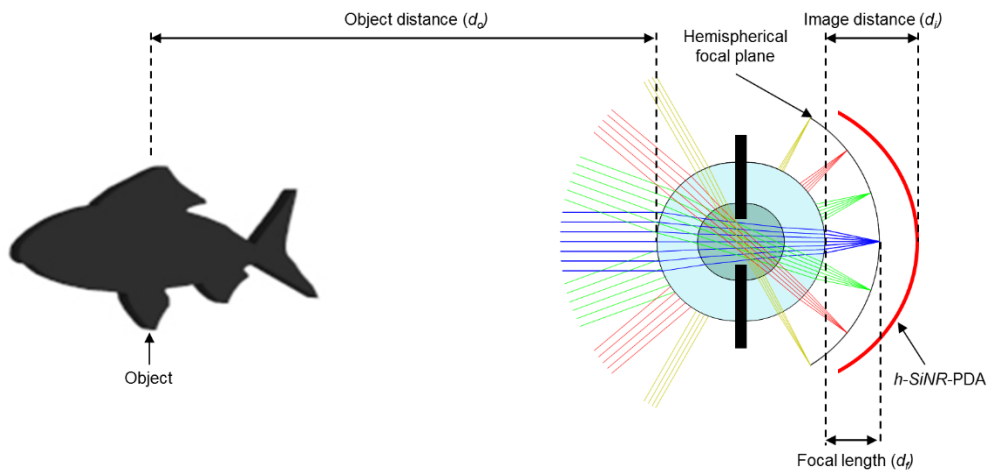


Figure 3.4. Imaging parameters. Schematic illustration showing imaging parameters, such as object distance (d_o ; distance between the object and *mo*-lens), image distance (d_i ; distance between *mo*-lens and retina), and focal length (d_f ; distance between *mo*-lens and focal plane).

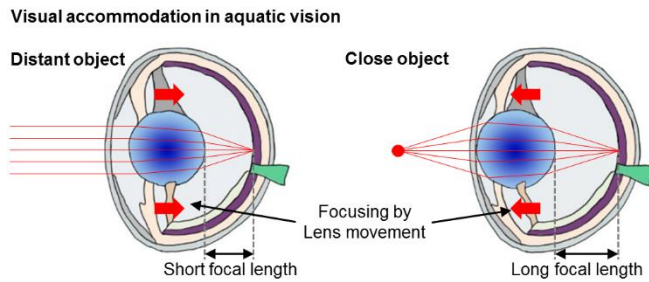


Figure 3.5. Visual accommodation in aquatic vision. Visual accommodation in the aquatic eye by moving the protruding *mo*-lens back and forth.

3.3.2 Optical analysis on the aquatic-vision-inspired imaging system

The optical system inspired by the aquatic vision provides negligible aberration, wide FoV, and deep DoF, mainly due to the integration of the tailored *mo*-lens with the *h-SiNR*-PDA (Figure 3.6a). The tailored *mo*-lens is a spherically symmetric lens, in which the half-ball lens (BK7) and the shell lens (SF16) are assembled on both sides of the aperture using transparent optical adhesive (Figure 3.6b). The photographs of assembled form of the tailored *mo*-lens are shown in Figure 3.6c. Detailed fabrication process of the tailored *mo*-lens is also described in Experimental section.

Such a core-shell structure (Figure 3.6b) is inspired by the parabolic RI profile in the protruding *mo*-lens of aquatic eyes (Figure 3.3b). However, in the tailored *mo*-lens, the outer shell (SF16, $R_{\text{out}} = 4.1$ mm) is designed to have a larger RI ($n_{\text{out}} = 1.65$) than the inner core (BK7, $R_{\text{in}} = 2$ mm; $n_{\text{in}} = 1.52$) to achieve the small focal spot radius, because the imaging system is under air, not underwater. The optimal RI difference of the lenses ($\Delta n = n_{\text{out}} - n_{\text{in}}$) and the radius ratio ($R_{\text{in}}/R_{\text{out}}$) are around 0.13 and 0.48, respectively (Figure 3.7). In addition, the aperture whose radius is as small as 1 mm blocks the stray light, thus minimizing optical aberration. Furthermore, the aperture is placed at the center of individual ball lenses to achieve wide FoV feature without light intensity attenuation at wide angular directions.

The engineered core-shell structure of the tailored *mo*-lens dramatically reduces the optical aberration by correcting monochrome and multi-chrome aberration for both of on- and off-axis. The reduced optical aberration is theoretically

analyzed by optical simulations for the tailored *mo*-lens to those for the conventional wide angle multi-lens and the homogeneous ball lens. The monochromatic spot radius by the tailored *mo*-lens maintains $\sim 4 \mu\text{m}$ for all incident angles, while that by the conventional wide angle multi-lens increases to $13.2 \mu\text{m}$ at wide angles and that by the homogeneous ball lens is always larger than $14.5 \mu\text{m}$ (Figure 3.8a). The coefficients of spherical aberration (SPHA), coma aberration (COMA), chromatic longitudinal aberration (CLA), chromatic transverse aberration (CTA), and astigmatism aberration (ASTI) of the tailored *mo*-lens are much smaller than those of the controls, indicating nearly aberration-free imaging capabilities by the tailored *mo*-lens (Figure 3.8b).

The tailored *mo*-lens also provides a deep DoF characteristics due to its short focal length ranging from 2.83 mm to 5.87 mm. Figure 3.8c shows the focal length of the objects at different distances focused by the tailored *mo*-lens, indicating that those objects can be focused by adjusting the image distance (d_i) to be equal to its focal length. The aquatic-vision-inspired imaging system can capture the well-focused images of objects with distances from 10 cm to infinity without blur when the image distance (d_i) is as same as the focal length of 2.95 mm (Figure 3.9a). The objects close to the aquatic-vision-inspired imaging system (*i.e.*, $< 10 \text{ cm}$) can be also focused by simply adjusting the image distance (d_i) while maintaining its original lens shape (Figure 3.9b and 3.9c).

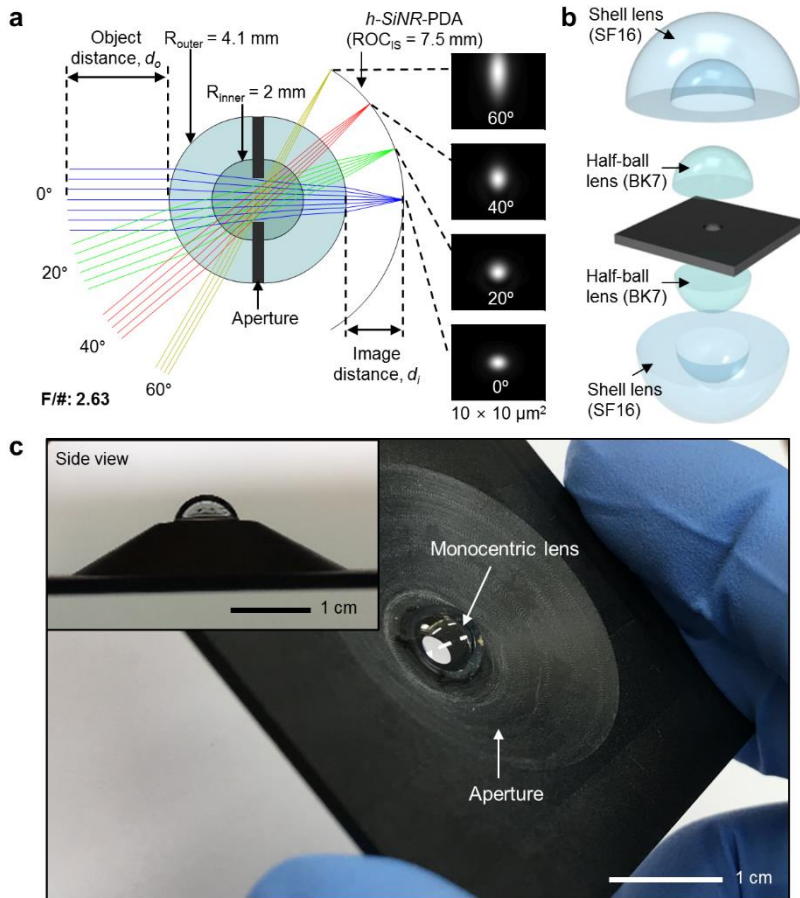


Figure 3.6. Tailored monocentric lens inspired by the protruding monocentric lens of aquatic eyes. (a) Ray tracing simulation of the aquatic-vision-inspired camera. (b) Exploded schematic illustration of the tailored *mo*-lens. (c) Photograph showing an assembled form of the tailored *mo*-lens.

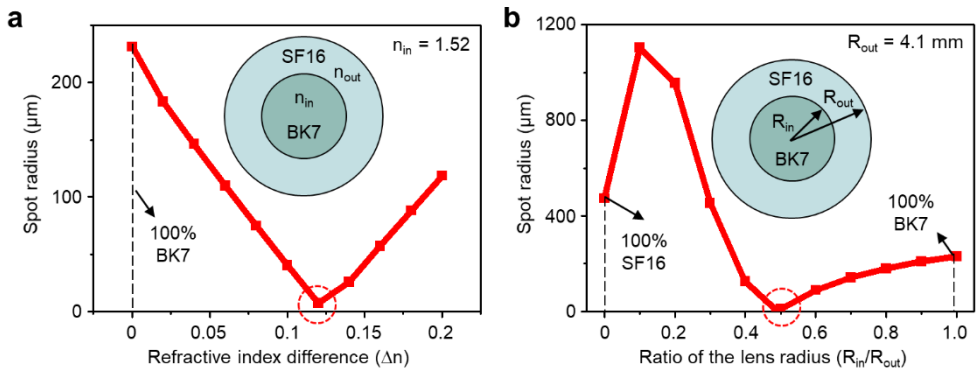


Figure 3.7. Optimized design factors of the tailored monocentric lens. (a,b) Optical simulation of the monochromatic spot radius for various RI differences (Δn) **a** and for various ratios of the lens radius ($R_{\text{in}}/R_{\text{out}}$) **b**.

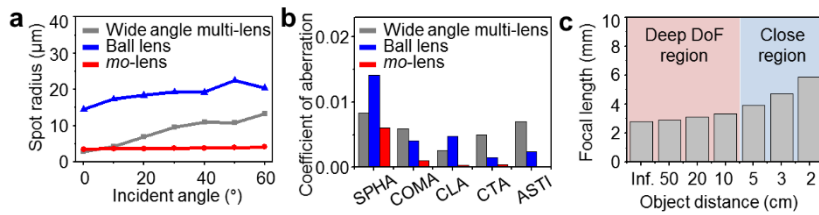


Figure 3.8. Theoretical analysis on the tailored monocentric lens. (a) Optical simulation of the monochromatic spot radius for different incident angles. (b) Seidel aberration coefficients of the tailored *mo*-lens and controls with R_{aperture} of 1 mm. (c) Focal length for objects at different distances, focused by the tailored *mo*-lens (reddish region for deep DoF region and bluish region for close region).

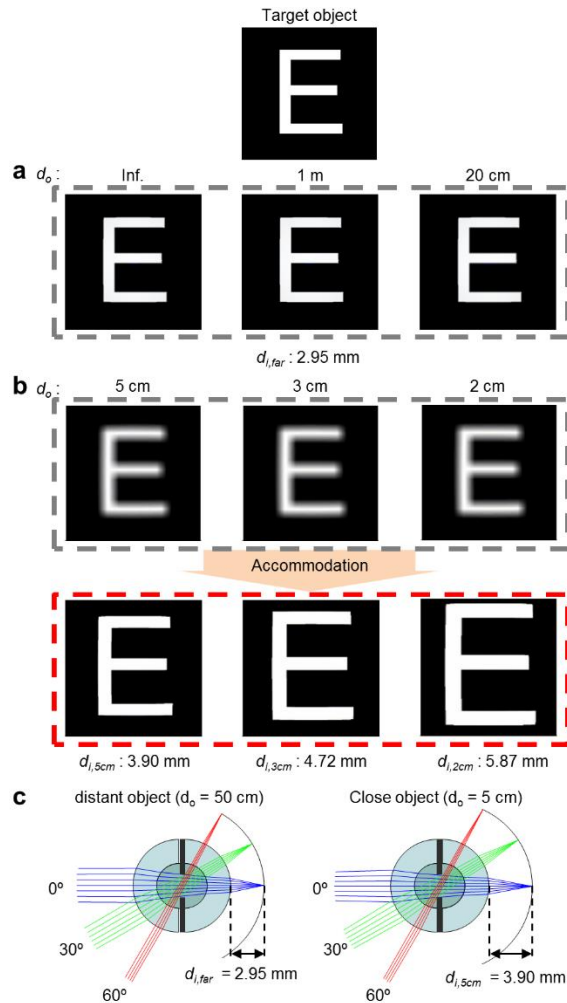


Figure 3.9. Optical simulation for visual accommodation of the tailored monocentric lens. (a) Imaging simulation for objects located at different d_o . The clear images are obtained for objects at $d_o = 20$ cm ~ infinity. (b) Imaging simulation for objects located at different d_o for the closer objects ($d_o < 5$ cm). The images focused by the *mo*-lens are blurred, but they can be easily accommodated by adjusting d_i . (c) Schematic drawing showing the visual accommodation for focusing an object located at distant (left) and close (right) position.

3.3.3 Hemispherical silicon nanorod photodiode array inspired by the retina of aquatic eyes

Inspired by the hemispherical retina with elongated rod cells in aquatic eyes, we developed *h-SiNR*-PDA, 23-by-23 passive matrix array of silicon photodiodes that have nanorod-textured surface with Al₂O₃ passivation (Figure 3.10a and inset). The array has hexagonal mesh structure (Figure 3.10a), and individual pixels are placed inside the hexagonal islands (Figure 3.10b left). Each pixel consists of a photodiode and a blocking diode, which are connected as n-p-n configuration for the passive matrix array operation (Figure 3.10c)^{14,27}. The detailed fabrication process of *h-SiNR*-PDA is described in Experimental section.

The hexagonal mesh array design minimizes the strain induced on the array by releasing the strain in interconnections²⁸⁻³⁰. The induced strain on the photodiode is 0.02% which is much lower than the fracture strain of silicon (~ 1%)³¹. The ultrathin thickness of the array (~ 5.5 μm) including silicon (~ 1.25 μm) is helpful to enhance mechanical flexibility of the array^{32,33}. Therefore, *h-SiNR*-PDA could be conformally laminated on the concavely hemispherical surface without mechanical fracture (Figure 3.10d). The pixel distribution at the perimeter of *h-SiNR*-PDA is close to a circle (Figure 3.10a), and thus the array can cover almost entire hemispherical surface.

In wide FoV imaging, vignetting (*i.e.*, light intensity attenuation at wide angles) has been a serious issue. For example, the light intensity after passing the conventional wide angle multi-lens is attenuated proportional to the fourth power of cosine function of incident angles³⁴. Although the spherical shape of *mo*-lens corrects

vignetting, the passed light intensity is still attenuated proportional to the cosine function of incident angles³⁴. In addition, thin flexible silicon photodiodes accompany limited photo-absorption³⁵⁻³⁷. Therefore, nanorod-texturing and passivation of the silicon photodiode surface are adopted to enhance photo-absorption and sensitivity. The texturing forms nanorods structure similar to the rod cells in aquatic eyes (Figure 3.10b right and inset for atomic force microscope (AFM) image and profile). The silicon nanorods (*SiNR*) have the height of 220 nm, diameter of 200 nm, and pitch of 520 nm, and a thin Al₂O₃ layer (~ 25 nm) passivates the textured surface (Figure 3.11a and 3.11b for transmission electron microscope (TEM) image and energy dispersive spectrometry (EDS) data), respectively).

The *SiNR* shows enhanced photo-absorption in visible spectrum compared to the bare silicon because its nanorod-textured surface reduces surface reflection and transmission (Figure 3.12)^{35,38}. The enhanced photo-absorption of *SiNR* is due to the light trapping effect by the periodic nanorods structure (*i.e.*, photonic crystal structure). The incident light is diffracted by the nanorod-textured surface and trapped inside the thin silicon due to total internal reflection, thus the light path for absorption is elongated (Figure 3.13). Such a photo-absorption enhancement principle is similar to that of elongated rod cells in aquatic eyes.

However, the nanorod-texturing of silicon surface forms surface dangling bonds that generate surface leakage current and thus increase I_{dark} (blue bar in Figure 3.14a left)³⁹. Furthermore, the surface dangling bonds contribute to undesirable charge carrier recombination sites, which reduces I_{photo} (blue bar in Figure 3.14a

right)³⁷. In this regard, Al₂O₃ passivation of nanorod-textured silicon surface suppresses the surface leakage current³⁹ and inhibits charge carrier recombination³⁸ by removing the dangling bonds. Therefore, more reduced I_{dark} and enhanced I_{photo} are observed in the *SiNR* photodiode with Al₂O₃ passivation (red bar in Figure 3.14a), compared to those in the photodiode fabricated with bare silicon and Al₂O₃ passivation (grey bar in Figure 3.14a).

With these attributes, the *SiNR* photodiode with Al₂O₃ passivation can measure the incident light intensities with enhanced sensitivity compared to the controls, such as the photodiode fabricated with *SiNR* but without Al₂O₃ passivation and that with bare silicon and Al₂O₃ passivation (Figure 3.14b). Figure 3.14c shows I-V curves of the *SiNR* photodiode with Al₂O₃ passivation under different illumination intensities. Under the light irradiation of 10.4 Wm⁻², the light intensity (I_{photo}/I_{dark}) of our *SiNR* photodiode with Al₂O₃ passivation is 86, which is 1.5 times larger than that of the photodiode fabricated with bare silicon and Al₂O₃ passivation.

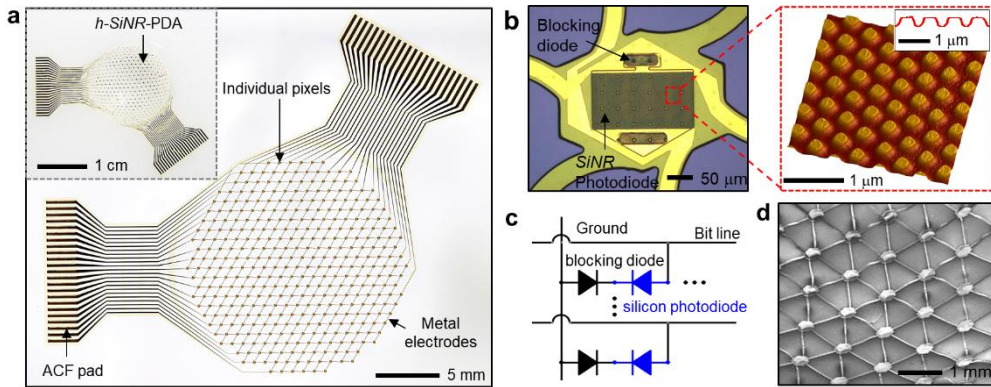


Figure 3.10. Hemispherical silicon nanorod photodiode array inspired by the retina of aquatic eyes. (a) Photograph of the *SiNR* photodiode array fabricated on a flat substrate. Inset shows a photograph of the same array transferred to the hemispherical surface. (b) Optical microscope image of an individual pixel consisting of a photodiode and a blocking diode (left). Three-dimensional AFM image of the surface morphology of *SiNR* (right). Inset shows the height profile of *SiNR*. (c) Schematic circuit diagram showing connection of a silicon nanorod photodiode and a blocking diode in a single pixel for the passive matrix array operation. (d) SEM image of the center part of *h-SiNR-PDA*.

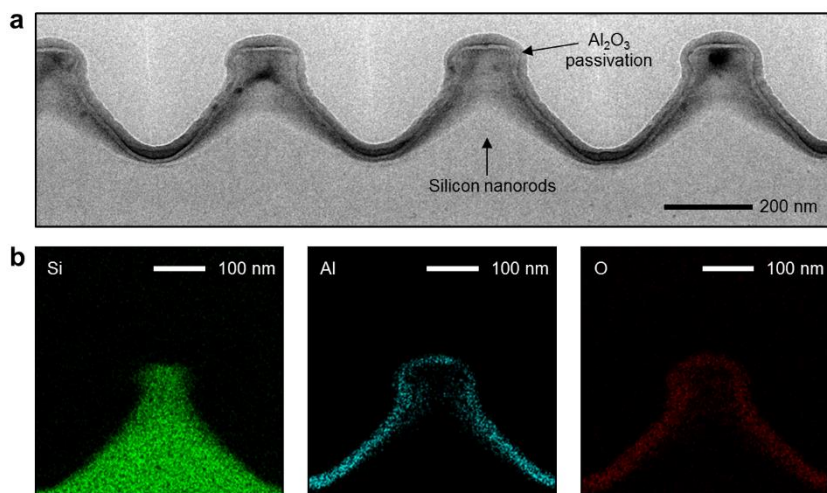


Figure 3.11. Characterization of silicon nanorods. (a) Cross-sectional TEM image of *SiNR* passivated with a thin Al_2O_3 layer. (b) EDS scan data of *SiNR*. The EDS scan analysis shows elemental distribution of Si (green; left), Al (cyan; middle), and O (red; right), and shows the shape of the Al_2O_3 layer.

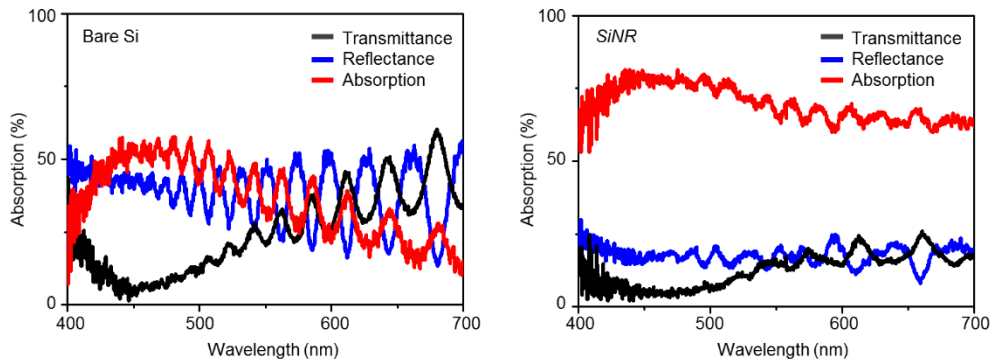


Figure 3.12. Optical characteristics of bare silicon and silicon nanorods.

Transmittance, reflectance, and absorption of bare silicon (left) and *SiNR* (right).

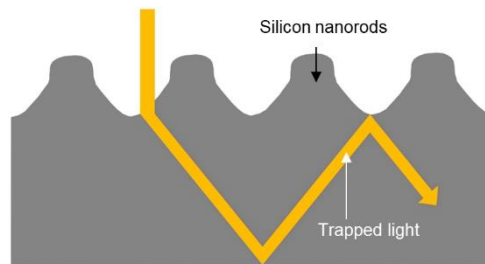


Figure 3.13. Light trapping by silicon nanorod structure. Schematic drawing showing the light diffracted by the *SiNR* structure and trapped inside the silicon nanomembrane due to the internal reflection.

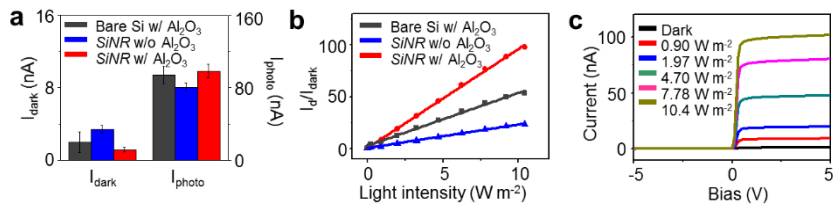


Figure 3.14. Device characterization of silicon nanorod photodiodes. (a) Statistical analysis ($N = 6$) for the I_{dark} and I_{photo} of the SiNR photodiode with Al_2O_3 passivation and controls (e.g., photodiode fabricated with bare silicon and Al_2O_3 passivation, photodiode fabricated with SiNR without Al_2O_3 passivation). (b) $I_{\text{photo}}/I_{\text{dark}}$ of SiNR Photodiode compared to controls under different light intensities. (c) I-V curve of the SiNR photodiode serially connected with a blocking diode under different light intensities.

3.3.4 Imaging demonstrations by using the integrated camera module

The tailored *mo*-lens and *h-SiNR*-PDA are assembled with a custom-made housing to fabricate the aquatic-vision-inspired imaging system (Figure 3.15). The image of the assembled camera module and their components are shown in Figure 3.16a and its inset, respectively. The aquatic-vision-inspired imaging system enables aberration-free wide FoV imaging, but the module size (*i.e.*, optical axis length) is eight times smaller than that of the conventional wide FoV camera module (Figure 3.16b). The module size of the developed imaging system is comparable to the size of a nickel coin (Figure 3.16b inset). The comparison of each system is summarized in Table 3.1.

The aquatic-vision-inspired imaging system successfully captures various pixelated panoramic images with wide FoV characteristics and without optical aberration. The optical camera image of the experimental setup for imaging demonstration and the data acquisition system is described in Figure 3.17. A scanning process was employed to enhance the effective resolution, where the aquatic-vision-inspired camera was rotated from -7° to 7° and -5° to 5° in the horizontal and vertical direction with the increment of 0.7° and 0.5° , respectively. Figure 3.18 shows the captured images, such as, a fish-shaped image and a letter ‘SNU’ (Figure 3.18 left and right, respectively). The captured images were rendered on the hemispherical surface whose radius is matched with the curvature of *h-SiNR*-PDA. Their original incident images are shown in inset of Figure 3.18. In wide FoV imaging, the outer side of the images corresponding to wide FoV of 120° can be effectively detected

using the pixels at the perimeter of the h -SiNR-PDA.

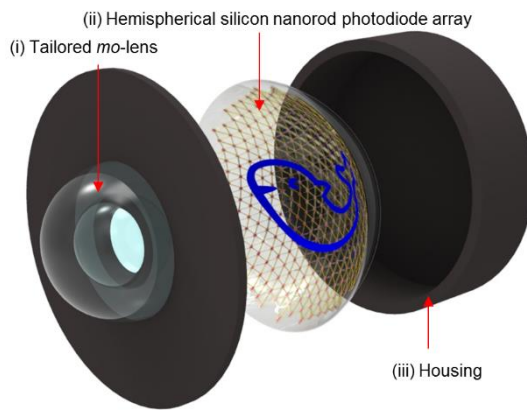


Figure 3.15. Aquatic-vision-inspired imaging system. Exploded schematic illustration of the aquatic-vision-inspired imaging system, consisting of (i) a tailored *mo*-lens, (ii) *h-SiNR*-PDA, and (iii) a housing.

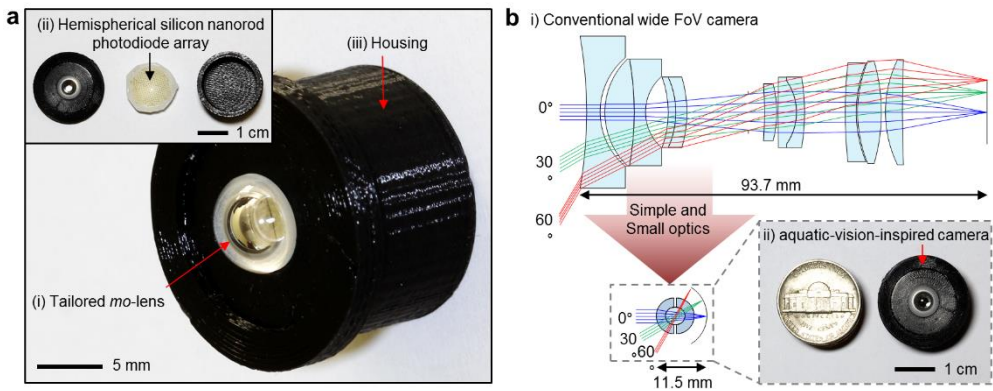


Figure 3.16. Integrated aquatic-vision-inspired imaging system. (a) Photograph of the assembled aquatic-vision-inspired imaging system. Inset shows its disassembled form. (b) Ray tracing simulation of the conventional wide FoV camera module (top) and the aquatic-vision-inspired imaging system (bottom). Inset compares the size of the aquatic-vision-inspired imaging system with a nickel coin.

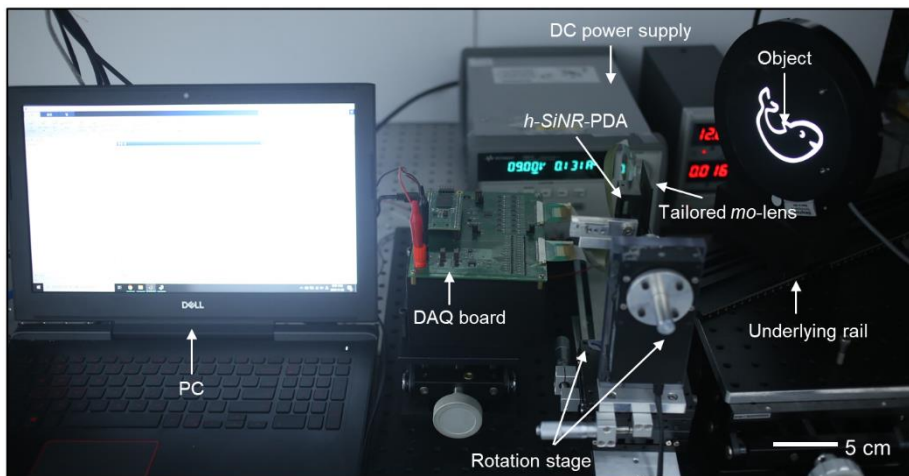


Figure 3.17. Experimental setup for the imaging demonstration. Optical camera image of the experimental setup including the data acquisition system. The shadow mask mounted on the light source generates the object, whose image is captured by the aquatic-vision-inspired camera. The underlying rails and rotation stages control the distances and angles of the object.

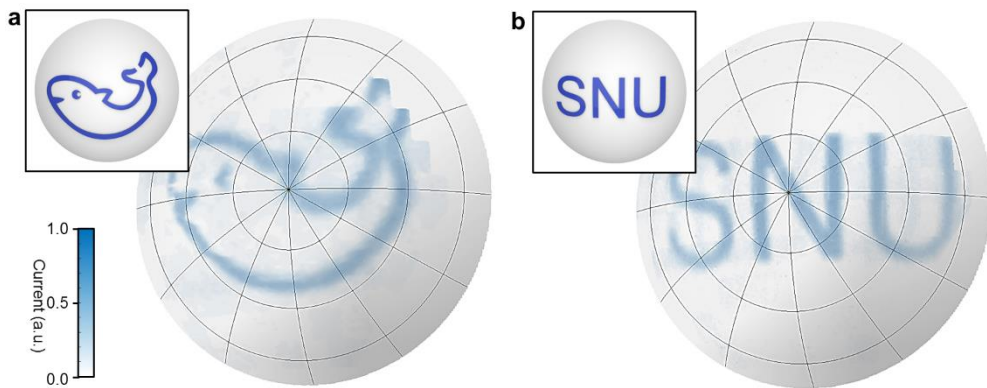


Figure 3.18. Imaging demonstration. (a,b) Panoramic imaging demonstrations (*e.g.*, fish-shape image **a** and the letter ‘SNU’ **b**).

3.4. Conclusion

The aquatic vision in nature, which consists of a protruding *mo*-lens and a highly sensitive hemispherical retina, inspires development of a novel miniaturized wide FoV camera by integrating the tailored *mo*-lens and *h-SiNR*-PDA. The unique features of the aquatic-vision-inspired camera include the wide FoV, miniaturized design, minimum optical aberration, deep DoF, facile accommodation, and enhanced light sensitivity, which enables high quality panoramic imaging by using single, small-sized optics. Through theoretical analyses and imaging demonstrations, we validate that all such characteristics are accomplished in one simple device. Furthermore, the passive matrix form of image sensor array, comprising of the silicon photodiode serially connected with the corresponding blocking diode, provides the way to enhance the imaging pixel density. Further integration of switching transistor which allows active matrix operation would be helpful for reducing the dark current and thus enhancing pixel density. The proposed aquatic-vision-inspired camera is expected to have advantages in obstacle avoidance and object tracking, providing new opportunities for advanced mobile electronics.

3.5. Reference

1. Floreano, D. & Wood, R. J. Science, technology and the future of small autonomous drones. *Nature* **521**, 460-466 (2015).
2. Jang, H. S., *et al.* A bezel-less tetrahedral image sensor formed by solvent-assisted plasticization and transformation of an acrylonitrile butadiene styrene framework. *Adv. Mater.* **30**, (2018).
3. Lee, G. J., Choi, C., Kim, D.-H. & Song, Y. M. Bioinspired artificial eyes: optic components, digital cameras, and visual prostheses. *Adv. Funct. Mater.* **28**, 1705202 (2018).
4. Chung, T., Lee, Y., Yang, S.-P., Kim, K., Kang, B.-H., & Jeong, K.-H. Mining the smartness of insect ultrastructures for advanced imaging and illumination. *Adv. Funct. Mater.* **28**, 1705912 (2018).
5. Dinyari, R., Rim, S.-B., Huang, K., Catrysse, P. B. & Peumans, P. Curving monolithic silicon for nonplanar focal plane array applications. *Appl. Phys. Lett.* **92**, 091114 (2008).
6. Lee, G. J., Nam, W. I. & Song, Y. M. Robustness of an artificially tailored fisheye imaging system with a curvilinear image surface. *Opt. Laser Technol.* **96**, 50-57 (2017).
7. Zhou, F., *et al.* Optoelectronic resistive random access memory for neuromorphic vision sensors. *Nat. Nanotechnol.* **14**, 776-782 (2019).
8. Lee, W., *et al.* Two-dimensional materials in functional three-dimensional

- architectures with applications in photodetection and imaging. *Nat. Commun.* **9**, 1417 (2018).
9. Tsai, W.-L., Chen, C.-Y., Wen, Y.-T., Yang, L., Cheng, Y.-L. & Lin, H.-W. Band tunable microcavity perovskite artificial human photoreceptors. *Adv. Mater.* **31**, 1900231 (2019).
 10. Choi, C., *et al.* Human eye-inspired soft optoelectronic device using high-density MoS₂-graphene curved image sensor array. *Nat. Commun.* **8**, 1664 (2017).
 11. Zhang, K., *et al.* Origami silicon optoelectronics for hemispherical electronic eye systems. *Nat. Commun.* **8**, 1782 (2017).
 12. Ko, H. C., *et al.* A hemispherical electronic eye camera based on compressible silicon optoelectronics. *Nature* **454**, 748-753 (2008).
 13. Artal, P. Optics of the eye and its impact in vision: a tutorial. *Adv. Opt. Photon.* **6**, 340-367 (2014).
 14. Song, Y. M., *et al.* Digital cameras with designs inspired by the arthropod eye. *Nature* **497**, 95-99 (2013).
 15. Floreano, D., *et al.* Miniature curved artificial compound eyes. *Proc. Natl. Acad. Sci. USA* **110**, 9267-9272 (2013).
 16. Jeong, K.-H., Kim, J. & Lee, L. P. Biologically inspired artificial compound eyes. *Science* **312**, 557-561 (2006).
 17. Huang, C.-C., Wu, X., Liu, H., Aldalali, B., Rogers, J. A. & Jiang, H. Large-field-of-view wide-spectrum artificial reflecting superposition compound eyes. *Small* **10**, 3050-3057 (2014).

18. Jagger, W. S. & Sands, P. J. A wide-angle gradient index optical model of the crystalline lens and eye of the rainbow trout. *Vision Res.* **36**, 2623-2639 (1996).
19. Jagger, W. S. & Sands, P. J. A wide-angle gradient index optical model of the crystalline lens and eye of the octopus. *Vision Res.* **39**, 2841-2852 (1999).
20. Mass, A. M. & Supin, A. Y. Adaptive features of aquatic mammals' eye. *Anat. Rec.* **290**, 701-715 (2007).
21. Charman, W. N. & Tucker, J. The optical system of the goldfish eye. *Vision Res.* **13**, 1-8 (1973).
22. Ott, M. Visual accommodation in vertebrates: mechanisms, physiological response and stimuli. *J. Comp. Physiol. A* **192**, 97-111 (2006).
23. Wagner, H.-J., Frohlich, E., Negishi, K. & Collin, S. P. The eyes of deep-sea fish II. Functional morphology of the retina. *Prog. Retin. Eye Res.* **17**, 637-685 (1998).
24. Partridge, J. C., Archer, S. N. & Lythgoe, J. N. Visual pigments in the individual rods of deep-sea fishes. *J. Comp. Physiol. A* **162**, 543-550 (1988).
25. Wu, T., *et al.* Design and fabrication of silicon-tessellated structures for monocentric imagers. *Microsyst. Nanoeng.* **2**, 16019 (2016).
26. Liu, H. W., Huang, Y. & Jiang, H. Artificial eye for scotopic vision with bioinspired all-optical photosensitivity enhancer. *Proc. Natl. Acad. Sci. USA* **113**, 3982-3985 (2016).
27. Lee, W., *et al.* High-resolution spin-on-patterning of perovskite thin films for a multiplexed image sensor array. *Adv. Mater.* **29**, 1702902 (2017).
28. Sim, K., *et al.* Three-dimensional curvy electronics created using conformal

- additive stamp printing. *Nat. Electron.* DOI: 10.1038/s41928-019-0304-4 (2019).
29. Shin, G., *et al.* Micromechanics and advances designs for curved photodetector arrays in hemispherical electronic-eye cameras. *Small* **6**, 851-856 (2010).
 30. Huang, Z., *et al.* Three-dimensional integrated stretchable electronics. *Nat. Electron.* **1**, 473-480 (2018).
 31. Park, S.-I., *et al.* Theoretical and experimental studies of bending of inorganic electronic materials on plastic substrates. *Adv. Funct. Mater.* **18**, 2673-2684 (2008).
 32. Choi, M. K., *et al.* Wearable red-green-blue quantum dot light-emitting diode array using high-resolution intaglio transfer printing. *Nat. Commun.* **6**, 7149 (2015).
 33. Kim, J., *et al.* stretchable silicon nanoribbon electronics for skin prosthesis. *Nat. Commun.* **5**, 5747 (2014).
 34. Rim, S.-B., Catrysse, P. B., Dinyari, R., Huang, K., & Peumans, P. The optical advantages of curved focal plane arrays. *Opt. Express* **16**, 4965-4971 (2008).
 35. Sheng, X., Johnson, S. G., Michel, J. & Kimerling L. C. Optimization-based design of surface textures for thin-film Si solar cells. *Opt. Express* **19**, A841-A850 (2011).
 36. Sheng, X., *et al.* Printing-based assembly of quadruple-junction four-terminal microscale solar cells and their use in high-efficiency modules. *Nat. Mater.* **13**, 593-598 (2014).
 37. Hoang, N.-V., *et al.* Giant Enhancement of Luminescence Down-Shifting by a

- Doubly Resonant Rare-Earth-Doped Photonic Metastructure. *ACS Photonics* **4**, 1705-1712 (2017).
38. Savin, H., *et al.* Black silicon solar cells with interdigitated back-contacts achieve 22.1% efficiency. *Nat. Nanotechnol.* **10**, 624-628 (2015).
39. Gao, Y., *et al.* Photon-trapping microstructures enable high-speed high-efficiency silicon photodiodes. *Nat. Photonics* **11**, 301-308 (2017).

Chapter 4. Curved neuromorphic image sensor array using MoS₂-organic heterostructure inspired by human visual recognition system

4.1 Introduction

Advances in the imaging, data storage, and processing technology have enabled diverse image-data-based processing tasks¹. And the recognition of the target image is a key procedure in many image-data-based applications^{1,2}, such as facial recognition³ and object detection². The image recognition based on conventional image sensors and data processing systems, however, is not ideal in terms of efficiency and power consumption^{4,5}, which are particularly important aspects for advanced mobile electronic devices⁶. This is because conventional systems recognize objects through a series of iterative computing steps that require the massive data storage, high-speed data processing, and numerous chip-to-chip data communications^{7,8} (Figure 4.1a).

For the image recognition process using the conventional system, the raw imagery data over the entire time domain is obtained by the flat image sensor array with the multi-lens optics^{9,10} and stored in a memory device for the frame-based image acquisition¹. The massive raw data is iteratively processed and stored by the central processing unit (CPU) and memory device for event detection and data

preprocessing³. Then the preprocessed data is transferred to and processed by the graphics processing unit (GPU) based on the neural network algorithm⁷ (*e.g.*, vector matrix multiplication¹¹) for feature extraction and classification¹². Such a series of iterative computing steps¹ as well as the multi-lens optics in conventional imaging devices¹³ increase the system-level complexity.

On the other hand, the human visual recognition system outperforms the conventional imaging and data processing systems particularly in the unstructured data classification such as the image recognition¹⁴. The human-eye optics is also much simpler than the multi-lens optics in conventional cameras^{9,13}. In the human visual recognition system, visual scenes are focused by a single lens, detected by the hemispherical retina, transmitted to the brain through optic nerves, and recognized by a neural network in the visual cortex¹ (Figure 4.1b). In the neural network, a distinctive feature is extracted from the acquired visual information through the synaptic plasticity^{15,16} (*i.e.*, short-term plasticity (STP) and long-term potentiation (LTP)), which is used for image identification by matching with the relevant memories¹⁷. From image sensing to recognition, therefore, the human visual recognition system can achieve the higher efficiency than conventional image sensors and data processing systems¹.

Inspired by human brain, the memristor crossbar array has been proposed as a neuromorphic data processing device^{3,18} which can potentially replace the GPU^{7,12}. Memristor arrays have demonstrated efficient vector matrix multiplications by physically implementing the neural network in hardware^{5,11}. However, these electrical

neuromorphic devices cannot directly respond to optical stimuli, and thus still need separate image sensors, memory, and processors to capture, store, and preprocess the massive visual information, respectively¹ (Figure 4.1c). Meanwhile, inspired by human eye, the curved image sensor arrays have been proposed^{19,20}. Although they could simplify the structure of the imaging module¹⁰, they don't have data processing capabilities and thus additional processing units and memory modules are still needed.

Ideally, a novel image sensor array, which enables the neuromorphic data preprocessing as well as the simplified image acquisition, is needed to dramatically improve the efficiency of the image recognition process²¹. We herein present a curved neuromorphic image sensor array (cNISA) using a heterostructure of MoS₂ and poly(1,3,5-trimethyl-1,3,5-trivinyl cyclotrisiloxane) (pV3D3), aiming for the highly efficient image acquisition and data preprocessing with a single neuromorphic imaging device (Figure 4.1d). The cNISA realizes the unique features of the human visual recognition system in a single integrated device, such as imaging with simple optics and processing with photon-triggered synaptic plasticity. The cNISA derives a preprocessed image from a set of noisy optical inputs through a single readout operation without the repetitive data storage, processing, and communications required in the conventional systems.

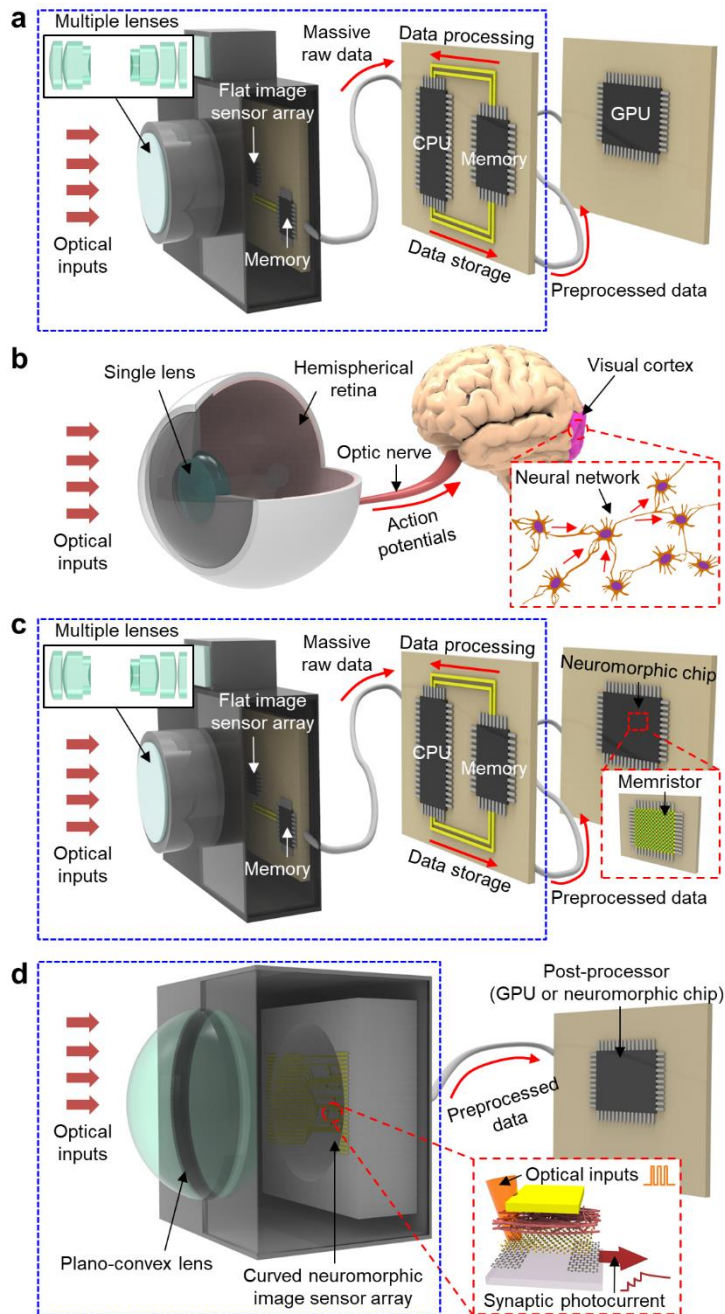


Figure 4.1. Imaging and data processing systems. (a) Schematic illustration of the conventional imaging and data processing system composed of multiple lenses, an

image sensor array, memory modules, and processing units (*e.g.*, CPU and GPU). **(b)** Schematic illustration of the human visual recognition system composed of a single human-eye lens, a hemispherical retina, optic nerves, and a neural network in the visual cortex. **(c)** Schematic illustration of the recently proposed imaging and data processing system composed of multiple lenses, an image sensor array, memory modules, and processing units (*e.g.*, CPU and neuromorphic chip). **(d)** Schematic illustration of the proposed curved neuromorphic imaging system composed of a single plano-convex lens, the cNISA, and a post-processor.

4.2. Experimental section

4.2.1 Fabrication of the curved neuromorphic image sensor array

The fabrication of cNISA began with spin-coating of a PI film ($\sim 1 \mu\text{m}$, bottom encapsulation; Sigma Aldrich, USA) on a SiO_2 wafer. A thin layer of Si_3N_4 ($\sim 15 \text{ nm}$, substrate) was deposited using the plasma-enhanced chemical vapor deposition (CVD) process, and was etched as an island-shape array using photolithography and dry etching. Graphene and MoS_2 were synthesized using CVD. Graphene ($\sim 2 \text{ nm}$, electrode) was transferred onto the Si_3N_4 layer. A thin Ti/Au layer ($\sim 5 \text{ nm}/25 \text{ nm}$) was deposited for the etch mask and used as probing pads. Graphene was patterned as an interdigitated source/drain electrode whose channel length is $5 \mu\text{m}$. The ultrathin MoS_2 layer ($\sim 4 \text{ nm}$, light-sensitive channel) was transferred onto the graphene electrodes, and patterned by photolithography and dry etching. A pV3D3 dielectric layer ($\sim 25 \text{ nm}$) was deposited through the initiated CVD. The pV3D3 layer was etched by photolithography and dry etching as an island-shape array. Then a lift-off process was used to pattern the Ti/Au layer ($\sim 5 \text{ nm}/25 \text{ nm}$, gate electrode) deposited by thermal evaporation. Additional deposition of parylene film ($\sim 1 \mu\text{m}$, top encapsulation) and dry etching completed fabrication of the neuromorphic image sensor array. The fabricated image sensor array was detached from the SiO_2 wafer using a water-soluble tape (3M Corp., USA), and then transfer-printed onto the polydimethylsiloxane (PDMS; Dow Corning, USA) hemispherical dome. The housing for mechanically supporting the plano-convex lens and cNISA was fabricated using a 3D printer (DP200, prototech Inc.).

4.2.2 Characterization of MoS₂-pV3D3 heterostructure

High-resolution TEM images of the vertical configuration of pV3D3-PT_r were obtained by using Cs corrected transmission microscope (JEM-ARM200F, JEOL). The surface potential of the MoS₂-pV3D3 heterostructure were measured by using KPFM (Dimension Icon, Bruker). Electrical properties were measured using a parameter analyzer (B1500A, Agilent). A white light-emitting diode was used as a light source. The pulsed optical inputs were generated using the Arduino UNO, and electrical properties were measured using a parameter analyzer (B1500A, Agilent).

4.2.3 Image acquisition and neuromorphic data preprocessing

A series of 20 images within the dataset of flipped images are irradiated to the cNISA with 0.5 sec time intervals. Then, the aperture blocked the stray light, and the plano-convex lens focused the incoming images on the cNISA. The cNISA constructed on a transparent convex hemispherical PDMS dome received the incident images and generated the synaptic photocurrent. The current amplifiers were fabricated on fabricated on the printed circuit board (PCB). The photocurrents of individual pixels were amplified using the connected current amplifiers, and were measured using a multi-channel data acquisition system (USB-6289, National Instruments). In addition, the photocurrents of individual pixels were individually recorded using the probe station.

4.3 Result and discussion

4.3.1 Curved neuromorphic imaging device inspired by the human visual recognition system

Figure 4.2a and 4.2b show schematic illustrations of the human visual recognition system and the curved neuromorphic imaging device inspired from it. The human eye, despite its simple optics, enables the high quality imaging without optical aberrations²² because its hemispherical retina matches with the hemispherical focal plane of the single human-eye lens⁹ (Figure 4.2a). The neural network exhibits the high efficiency for the unstructured data classification by deriving distinctive features of the input data using the synaptic plasticity¹⁴ (*i.e.*, STP and LTP); the intensity of the post-synaptic output signal is weighted by the frequency of pre-synaptic inputs¹⁵ (Figure 4.2a inset).

All such efficient features of the human visual recognition system are incorporated into an integrated neuromorphic imaging device. A single plano-convex lens focuses the incident light (*e.g.*, massive noisy images) on the cNISA that detects massive optical images and derives the preprocessed image through neuromorphic processes (Figure 4.2b). The concave curvature of the cNISA matches with the Petzval surface of the lens, minimizing optical aberrations without the need of the complicated multi-lens optics¹³. The photon-triggered synaptic plasticity, enabled by the MoS₂-pV3D3 heterostructure, derives the electrical output by weighting the optical inputs (Figure 4.2b inset). Such an integrated imaging device enables the image acquisition and data preprocessing through a single readout operation (*i.e.*,

image acquisition and neuromorphic preprocessing simultaneously).

The efficiency of the cNISA in comparison with that of conventional systems is explained in Figure 4.3. In case of the conventional imaging system with a conventional processor (*i.e.*, von-Neumann architecture; Figure 4.3a top), the flat image sensor array responds to the incoming light (optical inputs) focused by the multi-lens optics¹⁰ and generates the photocurrent proportional to the intensity of applied optical inputs²³. All measurements by the image sensors should be converted into digital signals and stored in the memory device for the frame-based image acquisition¹. Then the massive electrical inputs (*i.e.*, raw image data) are sent to the preprocessing module and preprocessed iteratively³. The preprocessed data is sent to the advanced processing units (*e.g.*, GPU) for the additional processing and the image recognition¹². Meanwhile, the neuromorphic chip has been proposed to overcome the computational inefficiency of the conventional von-Neumann architecture⁸ (Figure 4.3a bottom). However, there are still inefficient aspects in terms of the storage, transfer, and preprocessing of the massive electrical outputs (*i.e.*, raw image data) due to the isolated construction of the image sensor array from the neuromorphic chip¹.

On the other hand, the cNISA can simplify the imaging and data preprocessing steps, and thereby maximize the efficiency (Figure 4.3b). The cNISA receives optical inputs through a single lens, which can simplify the system construction (Figure 4.2b). The output photocurrent gradually increases in a pixel with frequently repeated optical inputs (LTP; bottom of Figure 4.2b inset), while it decays in a pixel with infrequent optical inputs (STP; top of Figure 4.2b inset). The

electrical output at each pixel presents the weighted value proportional to the frequency of optical inputs, which includes the history of entire optical inputs. Therefore, by reading the electrical output, the cNISA can derive a preprocessed image data directly from noisy optical inputs. Therefore, the massive data storage, numerous data communications, and iterative data processing in conventional systems are not required^{7,12}.

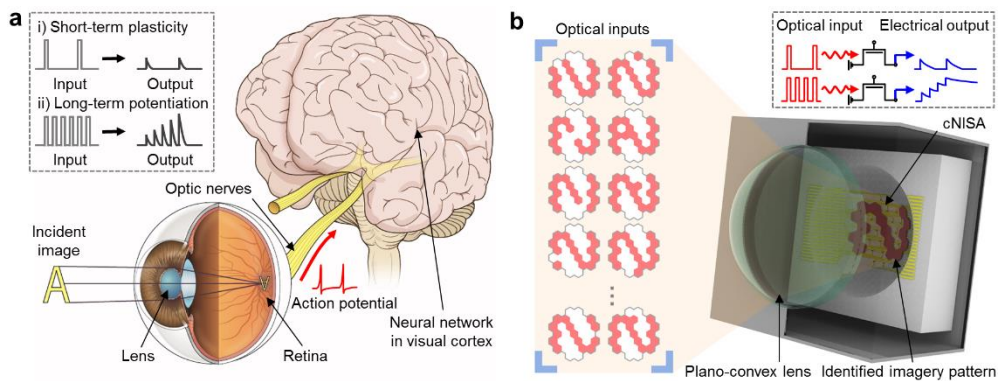


Figure 4.2. Curved neuromorphic imaging device inspired by the human visual recognition system. (a) Schematic illustration of the human visual recognition system comprised of a single human-eye lens, a hemispherical retina, optical nerves, and a visual cortex. The inset shows schematics showing STP and LTP of the neural network. (b) Schematic illustration of the curved neuromorphic imaging device . The inset (dashed box) shows the photon-triggered synaptic plasticity that derives an electrical output by weighting optical inputs.

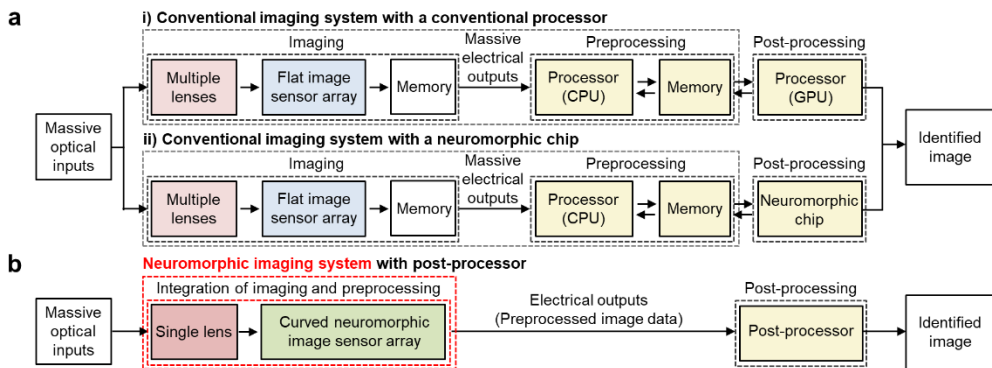


Figure 4.3. Image acquisition and neuromorphic preprocessing based on the imaging and data processing system. (a) Block diagram showing the sequence of the image recognition using the conventional imaging and data processing system (e.g., conventional imaging system with a conventional processor (top) or with a neuromorphic chip (bottom)). **(b)** Block diagram showing the sequence of the image recognition using the cNISA and a post-processor (GPU or neuromorphic chip).

4.3.2 Photon-triggered synaptic plasticity of MoS₂-pV3D3 phototransistor

The key principle of the image acquisition and neuromorphic preprocessing in the cNISA is the photon-triggered synaptic plasticity of the MoS₂-pV3D3 phototransistor (pV3D3-PTr). The pV3D3-PTr consists of a Si₃N₄ substrate, graphene source/drain electrodes, a MoS₂ light-sensitive channel, a pV3D3 dielectric layer, and a Ti/Au gate electrode (Figure 4.4a). An optical microscope image (top view) and cross-sectional transmission electron microscope (TEM) images are presented in Figure 4.4b and 4.4c. The pV3D3-PTr exhibits the light-sensitive field-effect transistor behavior²⁴ and maintains its original performances over three months (Figure 4.5).

The photoresponse of the pV3D3-PTr is comparable to the synaptic plasticity of the neural network. The photocurrent decays rapidly for infrequent optical inputs (*e.g.*, two optical pulses with 10 sec intervals; Figure 4.6a), which corresponds to STP. However, the photocurrent is accumulated for frequent optical inputs (*e.g.*, 20 optical pulses with 0.5 sec intervals; Figure 4.6b), which corresponds to LTP. The photocurrent accumulation is larger, as more frequent optical inputs are applied (Figure 4.7). Such a photon-triggered electrical response similar with the synaptic plasticity is attributed to two characteristics of the pV3D3-PTr, the quasi-linear time-dependent photocurrent increase and the prolonged photocurrent decay.

First, the pV3D3-PTr exhibits the quasi-linear time-dependent photoresponse (Figure 4.6c top). As a comparison, we prepared a control case, the MoS₂-Al₂O₃ phototransistor (Al₂O₃-PTr), which is a representative example of the

MoS₂-based phototransistors^{9,25} and shows the non-linear time-dependent photoresponse (Figure 4.6c bottom). For the quantitative characterization, a linearity factor (α), the degree of linearity of the photocurrent increase with respect to the illumination time ($I_{ph}^\alpha \sim t$), is defined. The linearity factor of the pV3D3-PTr (α_{pV3D3}) and that of the Al₂O₃-PTr ($\alpha_{Al_2O_3}$) are obtained by fitting $\log(I_{ph})$ with respect to $\log(t)$, and α_{pV3D3} (1.52) was closer to unity than $\alpha_{Al_2O_3}$ (2.50). As α approaches 1, the photocurrent can be accumulated linearly by the frequent optical inputs. However, if α is much larger than 1, the photocurrent becomes nonlinear, *i.e.*, saturated by the frequent optical inputs. Therefore, the pV3D3-PTr is more ideal than the control case (Al₂O₃-PTr) for the neuromorphic image data preprocessing due to linear response without saturation.

Second, the pV3D3-PTr shows the prolonged photocurrent decay, whose characteristics are shown in Figure 4.6d-f. The total decay time becomes longer with more frequent optical inputs. The decay time constant (τ_{decay}), the required time for the photocurrent decay to 1/e of the original value of the pV3D3-PTr, is proportional to the number of applied optical pulses (Figure 4.6d). Therefore, the decay time constant for LTP and STP ($\tau_{decay,LTP}$ and $\tau_{decay,STP}$) are 8.61 sec and 1.43 sec, respectively (red and black line in Figure 4.6e), and the retention time for LTP and STP are 3,600 sec and 1,200 sec, respectively (Figure 4.6f and its inset). Such large differences of the decay time and retention time between LTP and STP are critical to enhance the contrast of the neuromorphic preprocessing.

The high contrast between LTP and STP in the pV3D3-PTr is quantitatively

analyzed. The synaptic weight (A_n/A_1), a ratio of the photocurrent generated by n optical pulses (A_n) to the photocurrent generated by a single optical pulse (A_1), is defined (Figure 4.6g). The synaptic weight of the pV3D3-PTr continuously increases as the number of applied optical pulses increases (red line in Figure 4.6h), whereas the synaptic weight of the control (*i.e.*, Al₂O₃-PTr) becomes almost saturated after five optical pulses (black line in Figure 4.6h). Therefore, the pV3D3-PTr exhibits a larger synaptic weight (A_{25}/A_1) of 5.93 than the Al₂O₃-PTr with A_n/A_1 of 2.89 (Figure 4.8). Therefore, the pV3D3-PTr can exhibit the better contrast than the Al₂O₃-PTr.

The quasi-linear time-dependent photocurrent increase and the prolonged photocurrent decay are originated from the charge trapping in the MoS₂-pV3D3 heterostructure. The photo-generated holes are trapped in the MoS₂-pV3D3 heterostructure and increase the current flowing in the channel of the pV3D3-PTr by increasing the electric field^{26,27} (Figure 4.9). The hole trapping at the MoS₂-pV3D3 heterostructure, which induces excessive electrons in the MoS₂ layer, is corroborated by the negative shift of surface potential by the optical irradiation ($\Delta V = -98.6$ mV; Figure 4.10).

An analytical model of the MoS₂-based phototransistors²⁸ ($I_{ph}(t) = I_1(1 - \exp(-t/\tau_1)) + I_2(1 - \exp(-t/\tau_2))$) suggests two kinds of charge traps with the different trapping time constant²¹ (τ_1 and τ_2 ; $\tau_1 < \tau_2$) (Figure 4.11). One is the charge traps with small trapping time constant of $\tau_{1,pV3D3}$ (CT₁), and the other is the charge traps with large trapping time constant of $\tau_{2,pV3D3}$ (CT₂). It is believed that CT₁ is the shallow trap sites in the MoS₂ layer and CT₂ is the deep trap at the MoS₂-pV3D3

heterostructure²⁸. The trapping time constants (τ_1 , τ_2) and ratio of photocurrent coefficients (I_2/I_1) of the pV3D3-PTr and Al₂O₃-PTr are estimated in Figure 4.12. In the pV3D3-PTr, the photocurrent caused by CT₂ is much more dominant than that caused by CT₁, as validated via the large $I_{2,pV3D3}/I_{1,pV3D3}$ of 11.03. Meanwhile, $\tau_{2,pV3D3}$ is as large as 12.85 sec, which is 18.9 times larger than $\tau_{1,pV3D3}$ and even 2.93 times larger than $\tau_{2,Al2O3}$. Therefore, charge trapping in the pV3D3-PTr is very slow, which is compatible with the quasi-linear time-dependent photoresponse ($I_{ph} \sim I_{2,pV3D3}(t/\tau_{2,pV3D3})$). In addition, as more optical inputs are applied, more holes are trapped in CT₂, in which the trapped holes are more difficult to be detrapped than those in CT₁²¹, thus the photocurrent decay is prolonged in LTP.

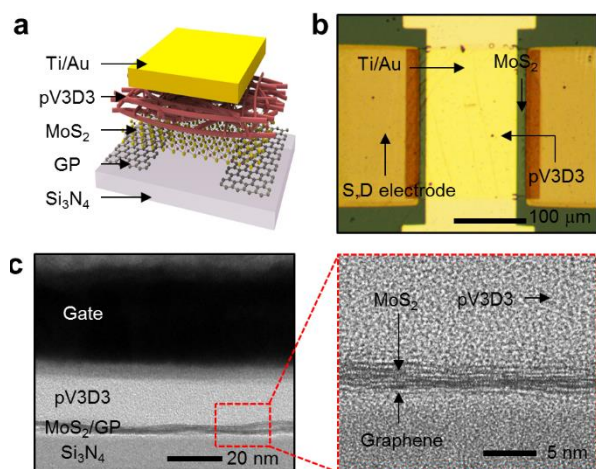


Figure 4.4. MoS₂-pV3D3 phototransistor. (a) Schematic illustration of the device structure of pV3D3-PTr. (b) Optical microscopic image of pV3D3-PTr. (c) Cross-sectional TEM image of pV3D3-PTr (left) and a magnified view (right).

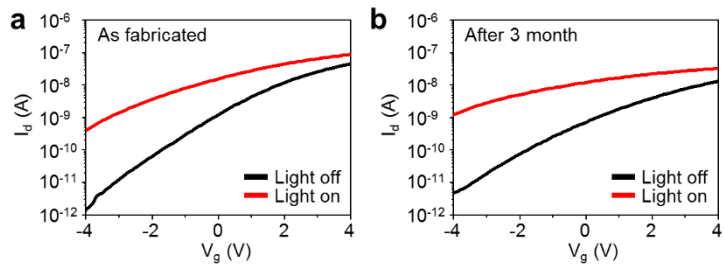


Figure 4.5. Electrical characterization of the MoS₂-pV3D3 phototransistor. (a) Transfer curves of the as-fabricated pV3D3-PTTr under light off/on condition. **(b)** Transfer curves of the pV3D3-PTTr kept in ambient condition for three month.

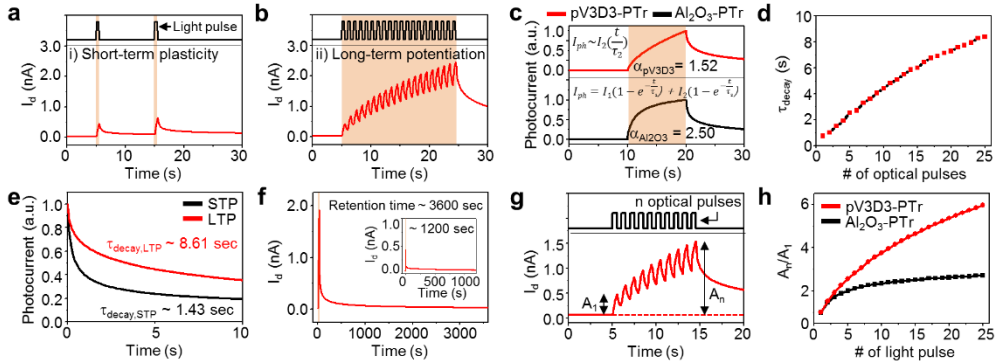


Figure 4.6. Photon-triggered neuromorphic behavior of the MoS₂-pV3D3 phototransistor. (a,b) Photon-triggered STP **a** and LTP **b** of pV3D3-PTr. (c) Photocurrent generation and decay characteristics of pV3D3-PTr and Al₂O₃-PTr. (d) Decay time constant of pV3D3-PTr depending on the number of applied optical pulses. (e) Photocurrent decay characteristics of pV3D3-PTr. STP indicates a single optical pulses, and LTP indicates 20 optical pulses with 0.5 sec interval. (f) Long-term photocurrent decay characteristic of pV3D3-PTr in respond to 20 optical pulses with 0.5 sec interval. Inset shows the photocurrent decay characteristic of pV3D3-PTr in respond to a single optical pulse. (g) Photocurrent generation and decay characteristic of pV3D3-PTr upon irradiation of 10 optical pulses. (h) A_n/A_1 of pV3D3-PTr and Al₂O₃-PTr as a function of the number of applied optical pulses.

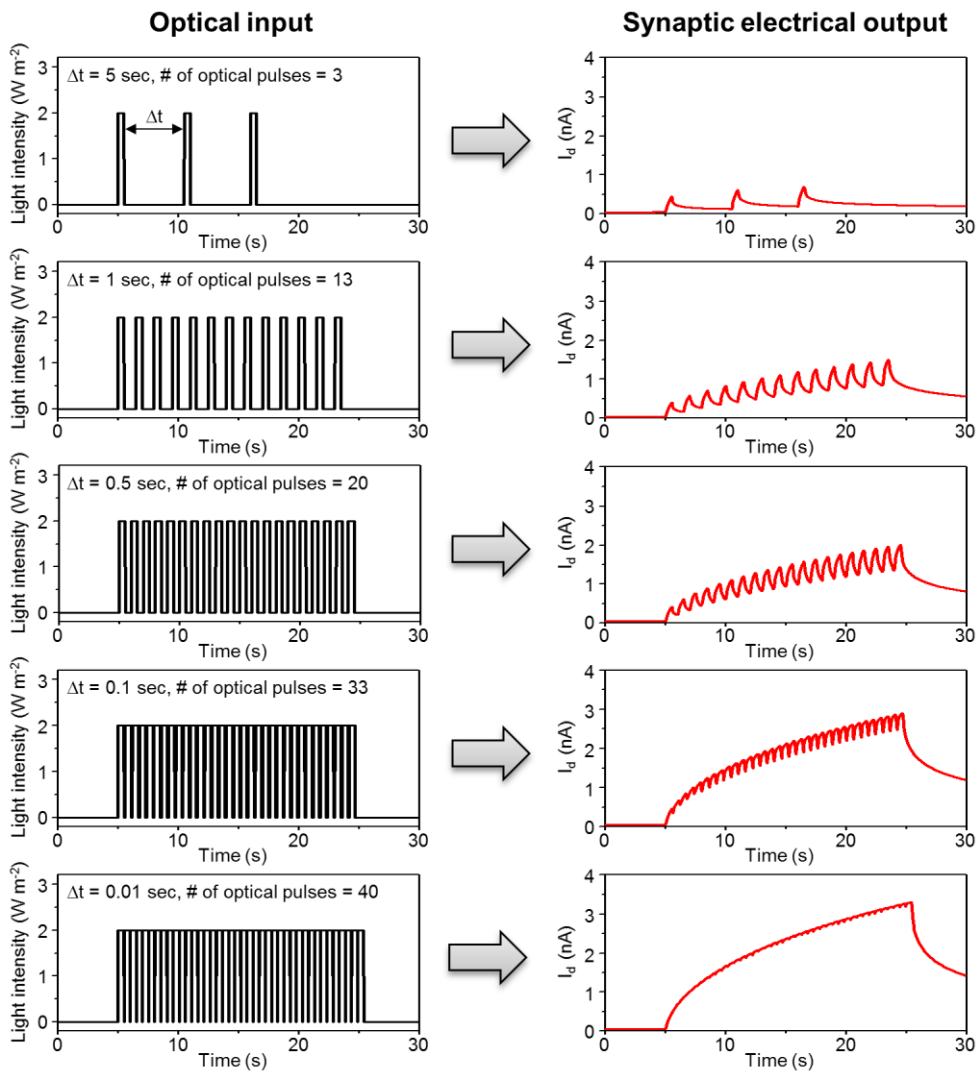


Figure 4.7. Photocurrent and decaying characteristics. Photocurrent generation and decaying characteristics of the pV3D3-PTi in respond to a series of optical pulses with different time intervals.

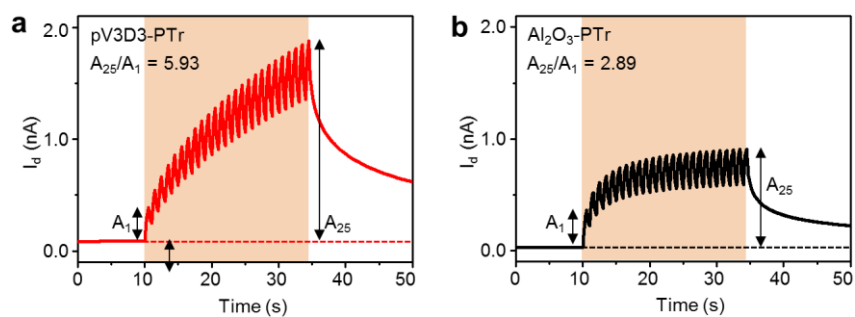


Figure 4.8. Synaptic weight. (a,b) Photocurrent generation and decaying characteristics of the pV3D3-PTr **a** and the control Al_2O_3 -PTr **b** upon irradiation of 25 optical pulses.

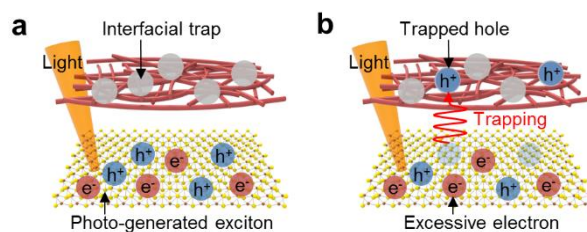


Figure 4.9. Photocurrent generation in the pV3D3-PTr. (a,b) Schematic illustration that explains the mechanism of photocurrent generation in the pV3D3-PTr. The incident light generates the excitons **a**, and the photo-generated holes are trapped at the interfacial traps **b**.



Figure 4.10. Kelvin probe force microscopy. **a**, Surface potential of MoS₂-pV3D3 heterostructure under light off (left) and on (right) condition. **b**, Surface potential of the MoS₂-pV3D3 heterostructure. The incident light changes from off-condition (region 1) to on-condition (region 2) during the scanning. The black arrow indicates the scanning direction.

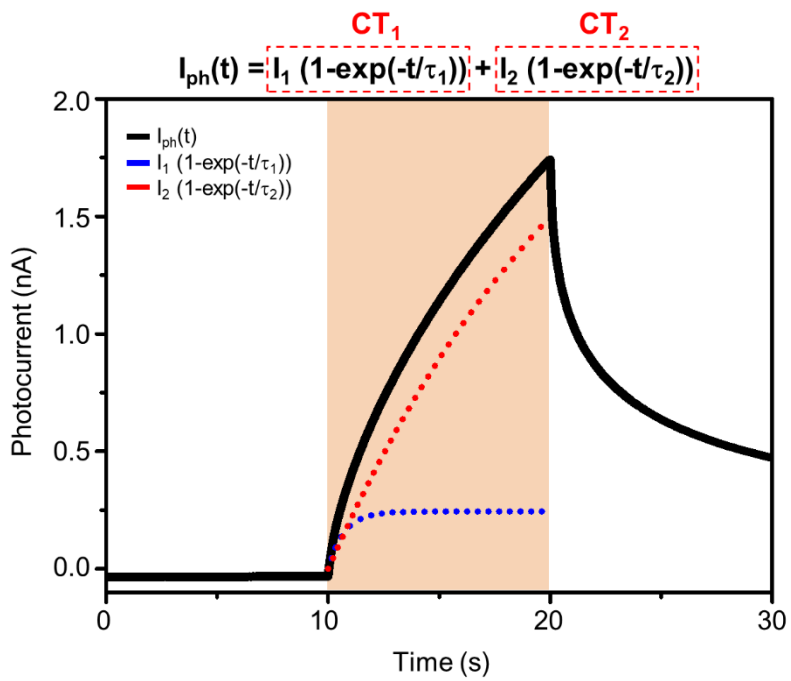


Figure 4.11. Analytical modeling of photoresponse. Analytical modeling of the photocurrent generation in the MoS₂-pV3D3 phototransistor.

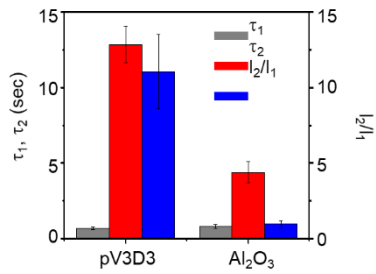


Figure 4.12. Analytical parameters of the MoS₂-pVD3 phototransistor. (a) The trapping time constants (τ_1 , τ_2) and the ratio of the coefficients of photocurrent (I_2/I_1) of pV3D3-PTr and Al₂O₃-PTr.

4.3.4 Image acquisition and neuromorphic preprocessing

We applied the cNISA to the image acquisition and neuromorphic preprocessing for deriving the preprocessed image from a set of noisy optical inputs. First, a simplified version of the array (3×3 pV3D3-PTrs) was used to explain the operation principle. The successively incident optical inputs (I_m) induce photocurrent ($I_{ph,n}$) in the individual pixels (P_n) (Figure 4.13a). $I_{ph,n}$ gradually changes by the illumination of noisy images (Left images in Figure 4.13a). Pixels #1, #2, #3, #5, and #8 receive eight optical pulses and thus show large accumulated photocurrent, while pixels #4, #6, #7, and #9 receive only one optical pulse and thereby show negligible photocurrent level (Figure 4.13b). Since the final photocurrents of individual pixels present the weighted value by the incident optical irradiation, the preprocessed image can be derived by mapping the photocurrents obtained through the single readout operation.

The mapped images at different time points are shown in Figure 4.13c. The enhanced image contrast with the reduced noise was obtained with more optical inputs. Eventually, the preprocessed image 'T' was obtained from the noisy input images (Figure 4.13d). In addition, the preprocessed image is memorized and slowly dissipated over a longer period of time (~ 60 sec; Figure 4.13e). This resembles the biological synaptic behavior of memorizing and forgetting. Therefore, the event detection process, which requires the storage, processing, and communications of massive raw imagery data over entire time domain, is not needed because the imagery information of the preceding event remains stored in the acquired data. In addition,

the memorized preprocessed image can be immediately erased, if needed, by applying positive gate bias ($V_g = 1$ V) (Figure 4.13f). The positive gate bias induces the detrapping of holes that have been trapped at the charge traps²⁶, returning the MoS₂-pV3D3 heterostructure to the initial state prior to the irradiation of optical inputs. Therefore, the subsequent image acquisition and neuromorphic preprocessing without the afterimage of previous imaging is enabled.

Then we built a curved neuromorphic imaging device based on the cNISA for efficient image acquisition and data preprocessing (Figure 4.14a). The curved neuromorphic imaging device is comprised of the single plano-convex lens that focuses the incident images, the cNISA that derives the preprocessed images from the noisy optical inputs, and the housing that supports the aforementioned components (Figure 4.14b). The image of its components is shown in Figure 4.14a inset. Among them, the cNISA is composed of the 31 pV3D3-PTrs, which are distributed in a nearly circular shape (Figure 4.15). By employing the ultrathin device structure^{29,30} (~75 nm thick; Figure 4.4c), using the intrinsically flexible materials (*i.e.*, graphene³¹, MoS₂³²⁻³⁴, and pV3D3³⁵), and applying the strain-releasing array design^{36,37} (*i.e.*, mesh structure), the cNISA can be fabricated on the concavely curved surface without the mechanical failure (Figure 4.14c). The measurement setup including current amplifiers and a multi-channel analog-to-digital converter (ADC) enables the photocurrent measurement of individual pixels in cNISA (Figure 4.14d and 4.16). Each pixel of cNISA is serially connected to the corresponding current amplifier via the anisotropic conductive film (ACF).

The cNISA successfully derived the preprocessed images from massive noisy optical inputs (Figure 4.17). First, a set of noisy C-shaped images (*e.g.*, 20 images with 0.5 sec intervals; Figure 4.18a) is frequently irradiated (reddish region in Fig. 4e top graph). Then, large photocurrent is accumulated at the pixels where the frequent optical inputs are irradiated (reddish region in Figure 4.17 middle graph), while negligible photocurrent is accumulated at the pixels where the infrequent optical inputs are irradiated (reddish region in Figure 4.17 bottom graph), thereby the preprocessed image ‘C’ is acquired (visualized images in Figure 4.17). The preprocessed image maintains stored for 30 sec as the accumulated photocurrent decays slowly. However, it can be immediately erased by applying the positive gate bias ($V_g = 1$ V) (bluish region in Figure 4.17). Then, the photocurrents of individual pixels return to the original values prior to the first irradiation of noisy C-shaped images. The similar image acquisition and neuromorphic preprocessing process for acquiring another preprocessed image ‘N’ from a set of frequently irradiated noisy N-shaped images (*e.g.*, 20 images with 0.5 sec intervals; Figure 4.18b) was also successfully demonstrated (greenish region in Figure 4.17). Therefore, by mapping the photocurrents obtained through the single readout operation at arbitrary time point, the preprocessed images with the enhanced contrast and the reduced noise as well as with the information of preceding events can be derived. In other words, such a curved neuromorphic imaging device enables highly efficient image acquisition and data preprocessing for the image recognition, for which conventional systems have dealt with massive raw imagery data.

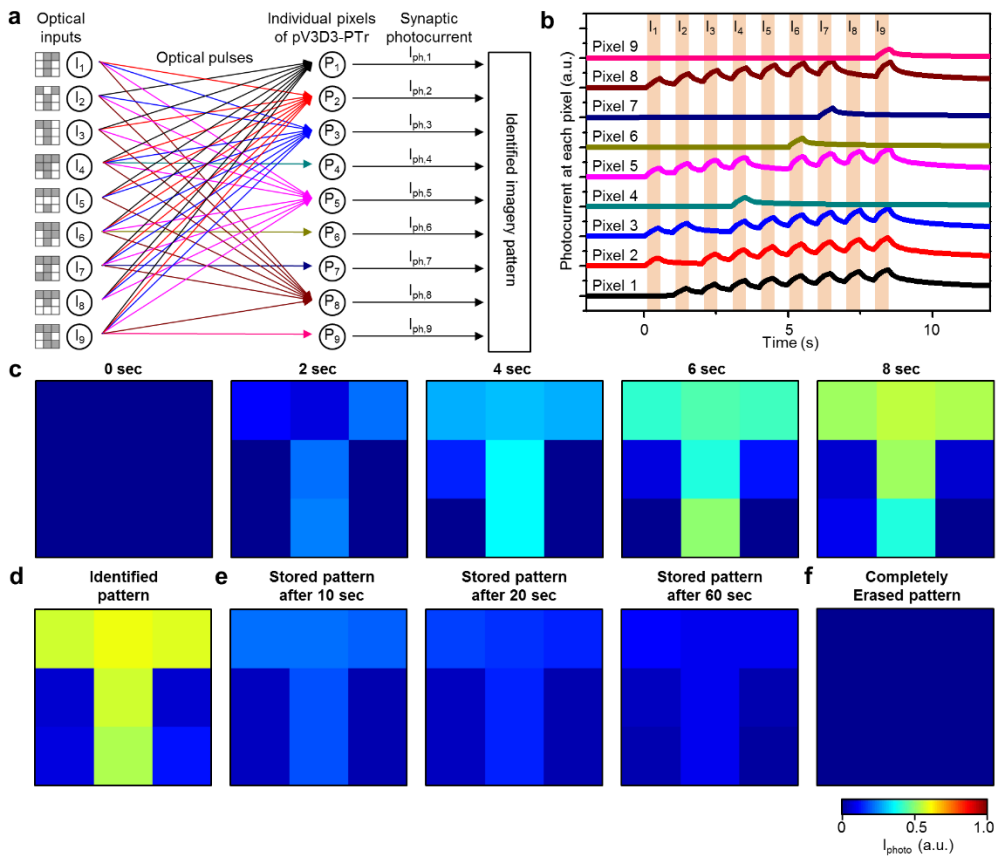


Figure 4.13. Image acquisition and neuromorphic preprocessing from noisy optical inputs. (a) Schematic diagram showing the image acquisition and neuromorphic preprocessing by using a 3×3 pV3D3-Ptr array. (b) Normalized photocurrent measured at each pixel of the 3×3 pV3D3-Ptr array. (c) Acquired imagery information at each time point. (d) The preprocessed image obtained through image acquisition and neuromorphic preprocessing. (e) The stored preprocessed images while photocurrents of individual pixels slowly decay. (f) The erased image by applied positive gate bias.

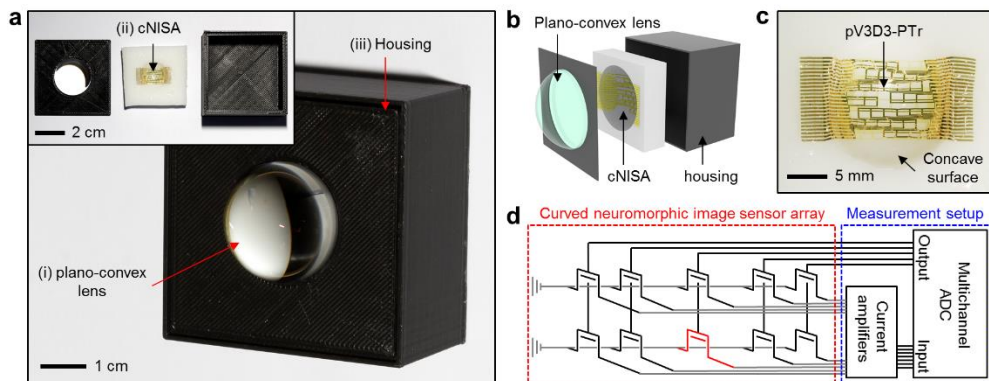


Figure 4.14. Curved neuromorphic imaging device. (a) Photograph of the integrated curved neuromorphic imaging device comprised of the plano-convex lens, the cNISA, and the housing. Inset shows the disassembled form of the neuromorphic imaging system. (b) Exploded illustration of the curved neuromorphic imaging device. (c) Photograph of the cNISA. (d) Schematic diagram of the measurement setup for measuring the photocurrents of individual pixels in cNISA.

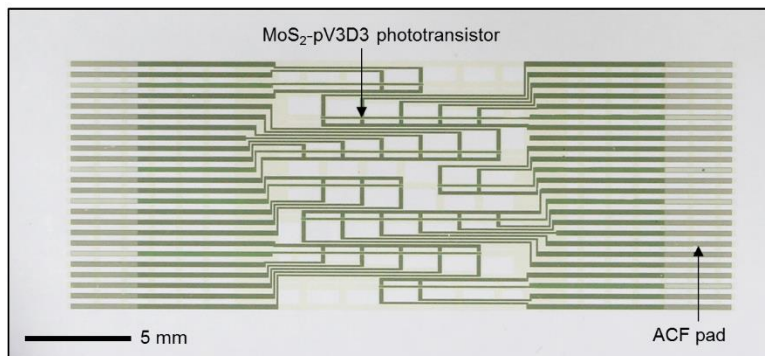


Figure 4.15. Neuromorphic image sensor array on planar substrate. Photograph of the array form of 31 pV3D3-PTs on planar substrate.

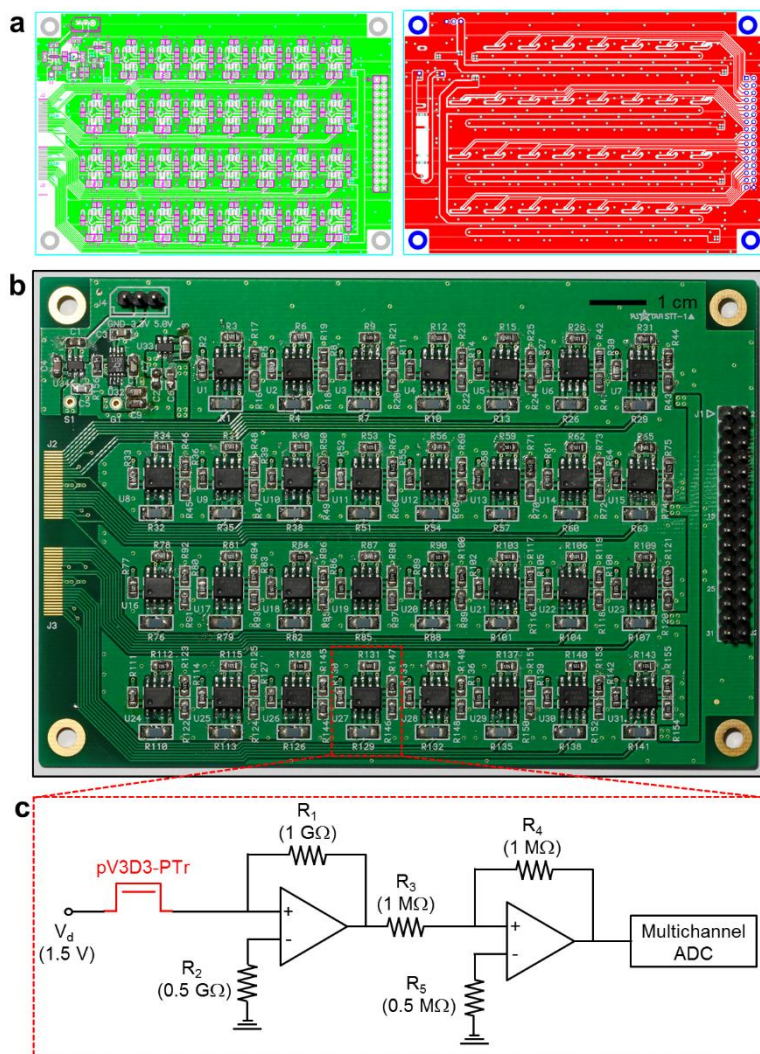


Figure 4.16. Measurement setup. (a) Layout of PCB showing the comprising components. (b) Optical camera image of PCB. (c) Schematic diagram of the current amplifier used in the measurement setup for translating the photocurrent into the amplified voltage signals.

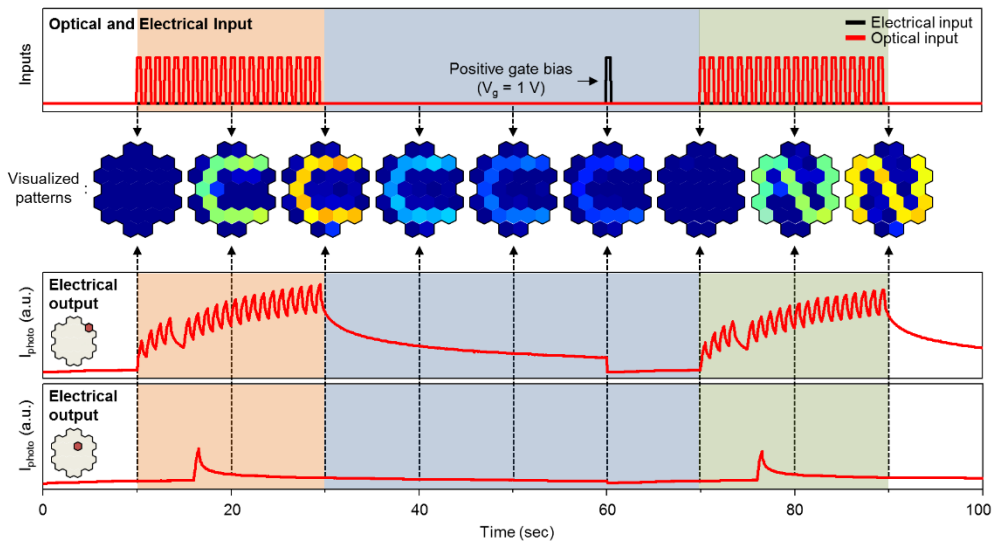


Figure 4.17. Image acquisition and neuromorphic preprocessing . image acquisition and neuromorphic preprocessing process for recognizing each set of noisy input images (C-shape images (red) and N-shape image (green)). Top graph shows optical and electrical inputs, and middle and bottom graphs show photocurrent accumulation and decay at the reddish pixels.

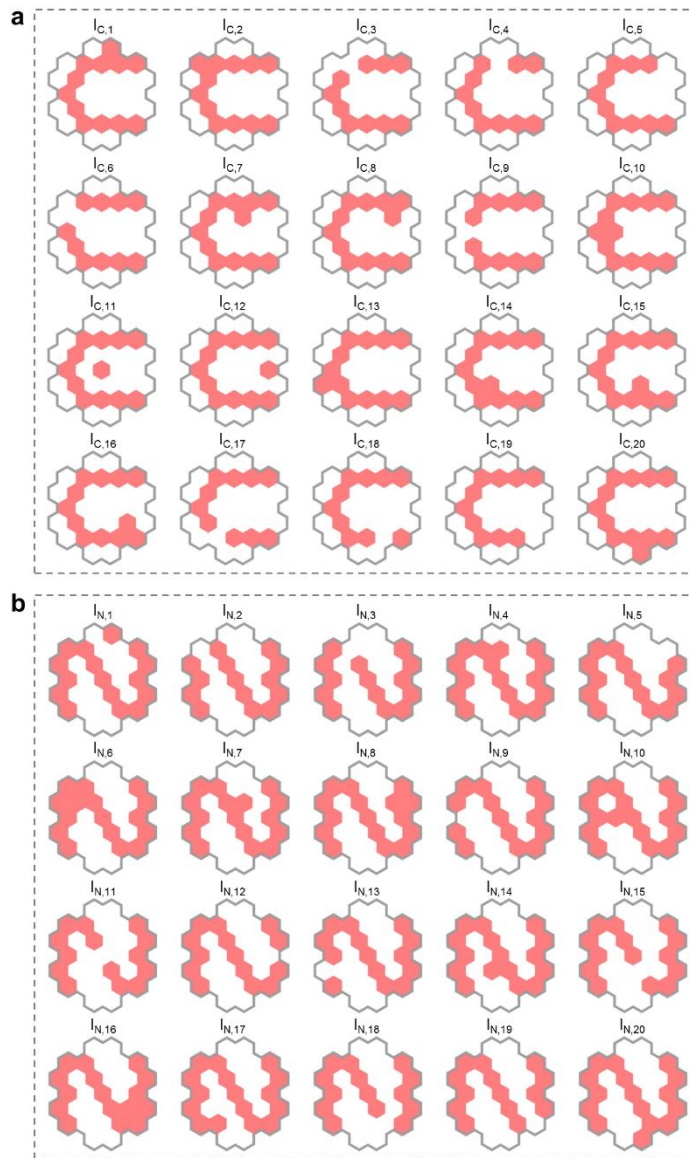


Figure 4.18. Set of noisy images. (a,b) Schematic illustration of the set of flipped images (e.g., C-shape noisy images **a** and N-shape noisy images **b**)

4.4 Conclusions

In this study, the cNISA inspired by the human visual recognition system is developed by using a MoS₂-organic heterostructure for efficient image acquisition and data preprocessing. Unique features of the human visual recognition system, such as the curved retina with simple optics and the synaptic plasticity-based neuromorphic processing, are realized in one integrated device. The photon-triggered synaptic plasticity is the unique feature of MoS₂-pV3D3 heterostructure that exhibits the quasi-linear time-dependent photoresponse and prolonged photocurrent decay. Experimental and theoretical analyses validate the photon-triggered synaptic plasticity in the MoS₂-pV3D3 heterostructure. The cNISA successfully derives the preprocessed images from a set of noisy optical inputs through the single readout operation (*i.e.*, image acquisition and neuromorphic preprocessing). The proposed cNISA is a step forward to the next-generation highly efficient image sensing and recognition system, and is expected to inspire many image-data-based applications in the future.

4.5 References

1. Zhou, F. *et al.* Optoelectronic resistive random access memory for neuromorphic vision sensors. *Nat. Nanotechnol.* **14**, 776-782 (2019).
2. Roy, K., Jaiswal, A. & Panda, P. Towards spike-based machine intelligence with neuromorphic computing. *Nature* **575**, 607-617 (2019).
3. Yao, P. *et al.* Face classification using electronic synapses. *Nat. Commun.* **8**, 15199 (2017).
4. Zidan, M. A., Strachan, J. P. & Lu, W. D. The future of electronics based on memristive systems. *Nat. Electron.* **1**, 22-29 (2018).
5. Burgt, Y., Melianas, A., Keene, S. T., Malliaras, G. & Salleo, A. Organic electronics for neuromorphic computing. *Nat. Electron.* **1**, 386-397 (2018).
6. Floreano, D. & Wood, R. J. Science, technology and the future of small autonomous drones. *Nature* **521**, 460-466 (2015).
7. Jeong, D. S. & Hwang, C. S. Nonvolatile memory materials for neuromorphic intelligent machines. *Adv. Mater.* **30**, 1704729 (2018).
8. Gkoupidenis, P., Koutsouras, D. A. & Malliaras, G. G. Neuromorphic device architectures with global connectivity through electrolyte gating. *Nat. Commun.* **8**, 15448 (2017).
9. Choi, C. *et al.* Human eye-inspired soft optoelectronic device using high-density MoS₂-graphene curved image sensor array. *Nat. Commun.* **8**, 1664 (2017).
10. Ko, H. C. *et al.* A hemispherical electronic eye camera based on compressible

- silicon optoelectronics. *Nature* **454**, 748-753 (2008).
11. Sheridan, P. M. *et al.* Sparse coding with memristor networks. *Nat. Nanotechnol.* **12**, 784-789 (2017).
 12. Xia, Q. & Yang, J. J. Memristive crossbar arrays for brain-inspired computing. *Nat. Mater.* **18**, 309-323 (2019).
 13. Lee, G. J., Choi, C., Kim, D.-H. & Song, Y. M. Bioinspired artificial eyes: optic components, digital cameras, and visual prostheses. *Adv. Funct. Mater.* **28**, 1705202 (2018).
 14. Lee, M. *et al.* Brain-inspired photonic neuromorphic devices using photodynamic amorphous oxide semiconductors and their persistent photoconductivity. *Adv. Mater.* **29**, 1700951 (2017).
 15. Ohno, T. *et al.* Short-term plasticity and long-term potentiation mimicked in single inorganic synapses. *Nat. Mater.* **10**, 591-595 (2011).
 16. Wang, H. *et al.* A ferroelectric/electrochemical modulated organic synapse for ultraflexible, artificial visual-perception system. *Adv. Mater.* **30**, 1803961 (2018).
 17. Brady, T. F., Konkle, T., Alvarez, G. A. & Oliva, A. Visual long-term memory has a massive storage capacity for object details. *Proc. Natl. Acad. Sci. USA* **105**, 14325-14329 (2008).
 18. Prezioso, M. *et al.* Training and operation of an integrated neuromorphic network based on metal-oxide memristors. *Nature* **521**, 61-64 (2015).
 19. Zhang, K. *et al.* Origami silicon optoelectronics for hemispherical electronic eye systems. *Nat. Commun.* **8**, 1782 (2017).

20. Lee, W. *et al.* Two-dimensional materials in functional three-dimensional architectures with applications in photodetection and imaging. *Nat. Commun.* **9**, 1417 (2018).
21. Seo, S. *et al.* Artificial optic-neural synapse for colored and color-mixed pattern recognition. *Nat. Commun.* **9**, 5106 (2018).
22. Jung, I. *et al.* Dynamically tunable hemispherical electronic eye camera system with adjustable zoom capability. *Proc. Natl. Acad. Sci. USA* **108**, 1788-1793 (2011).
23. Kim, J. *et al.* Photon-triggered nanowire transistors. *Nat. Nanotechnol.* **12**, 963-968 (2017).
24. Kang, K. *et al.* High-mobility three-atom-thick semiconducting films with wafer-scale homogeneity. *Nature* **520**, 656-660 (2015).
25. Cheng, R. *et al.* Few-layer molybdenum disulfide transistors and circuits for high-speed flexible electronics. *Nat. Commun.* **5**, 5143 (2014).
26. Lee, J. *et al.* Monolayer optical memory cells based on artificial trap-mediated charge storage and release. *Nat. Commun.* **8**, 14734 (2017).
27. Pak, J. *et al.* Intrinsic optoelectronic characteristics of MoS₂ phototransistors via a fully transparent van der Waals heterostructure. *ACS Nano* **13**, 9638-9646 (2019).
28. Amit, I. *et al.* Role of charge traps in the performance of atomically thin transistors. *Adv. Mater.* **29**, 1605598 (2017).
29. Kaltenbrunner, M. *et al.* An ultra-lightweight design for imperceptible plastic

- electronics. *Nature* **499**, 458-463 (2013).
30. Choi, M. K. *et al.* Wearable red-green-blue quantum dot light-emitting diode array using high-resolution intaglio transfer printing. *Nat. Commun.* **6**, 7149 (2015).
 31. Kang, P., Wang, M. C., Knapp, P. M. & Nam, S. Crumpled graphene photodetector with enhanced, strain-tunable, and wavelength-selective photoresponsivity. *Adv. Mater.* **28**, 4639-4645 (2016).
 32. Yin, Z.Y. *et al.* Single-layer MoS₂ phototransistors. *ACS Nano* **6**, 74-80 (2012).
 33. Akinwande, D., Petrone, N. & Hone, J. Two-dimensional flexible nanoelectronics. *Nat. Commun.* **5**, 5678 (2014).
 34. Lee, C.-H. *et al.* Atomically thin p-n junctions with van der Waals heterointerfaces. *Nat. Nanotechnol.* **9**, 676-681 (2014).
 35. Moon, H. *et al.* Synthesis of ultrathin polymer insulating layers by initiated chemical vapour deposition for low-power soft electronics. *Nat. Mater.* **14**, 628-635 (2015).
 36. Son, D. *et al.* Multifunctional wearable devices for diagnosis and therapy of movement disorders. *Nat. Nanotechnol.* **9**, 397-404 (2014).
 37. Kim, J. *et al.* Stretchable silicon nanoribbon electronics for skin prosthesis. *Nat. Commun.* **5**, 5747 (2014).

요약 (국문초록)

사람 및 수중 생물에서 영감을 받은 나노물질 기반

비정형 이미지 센서 어레이

학번: 2014-31082

이름: 최창순

종래의 카메라 기술은 사물 감지 및 장애물 회피 등과 같은 이미지 기반 어플리케이션에서 많은 관심을 받아왔다. 하지만 기존의 카메라는 평면형의 이미지 센서에 초점을 맞추기 위하여 여러 개의 렌즈로 구성된 복잡한 광학계를 필요로 하기 때문에, 무겁고 부피가 커서 최근 중요성이 부각되고 있는 모바일 전자제품에 사용되기 힘들다. 이러한 점에서 진화를 통해 최적화된 자연계의 눈들은 다양한 장점들 덕분에 새로운 카메라를 개발하는데 영감을 준다. 다양한 장점은 간소하고 작아진 광학계, 넓은 시야각, 민감하고 효율적인 광측정, 깊은 초점심도, 쉬운 초점조절 방법이 있다.

따라서 이 논문을 통해 자연을 모사한 새로운 이미징 시스템 3개를 소개하고자 한다. 첫번째로 MoS_2 -graphene 헤테로구조를 이용하여 유연한 광전자 소자를 제작하였고, 이를 이용하여 사람 눈을 모사한 커브드 이미지센서를 개발하였다. 개발된 커브드 이미지 센서는 하나의 렌즈 만

으로도 수차 없는 이미징을 할 수 있었다. 또한 망막 보조 장치로도 적용되어, 망막에 기계적 부작용을 주지 않으면서도 망막을 전기적으로 자극할 수 있었다.

두번째로 구형 렌즈와 반구형 이미지센서를 통합하여 수중 생물의 눈을 모사한 이미징 시스템을 개발했다. 개발된 수중 생물 모사 이미징 시스템은 소형화된 단일 렌즈 광학계로 광시야각 이미징을 수차 없이 수행할 수 있었으며, 깊은 초점 심도와 간편한 초점 조절방식을 보였다. 이러한 특징들을 이용하여 넓은 각도에서 입사되는 이미지들을 성공적으로 감지할 수 있었다.

세번째로 이미지 센서에 뉴로몰픽 기능을 부여함으로써 사람의 시각 인식 시스템 전체를 모사한 커브드 뉴로몰픽 이미지 센서를 제작하였다. MoS_2 -유기물질 헤테로구조에 기반한 뉴로몰픽 이미지 센서는 빛에 반응하는 시냅스 가소성을 보였다. 따라서 불필요한 데이터 저장, 처리, 및 통신 없이도 무수히 많은 광학 입력들로부터 고유한 패턴을 식별해낼 수 있었다.

주요어: 자연 모사 카메라, 플렉서블, 사람 눈 모사, 수중 생물 시각 모사, 뉴로몰픽 이미지 센서